AECL
EACL

AECL NUCLEAR REVIEW

VOLUME 1, NUMBER 1
JUNE 2012

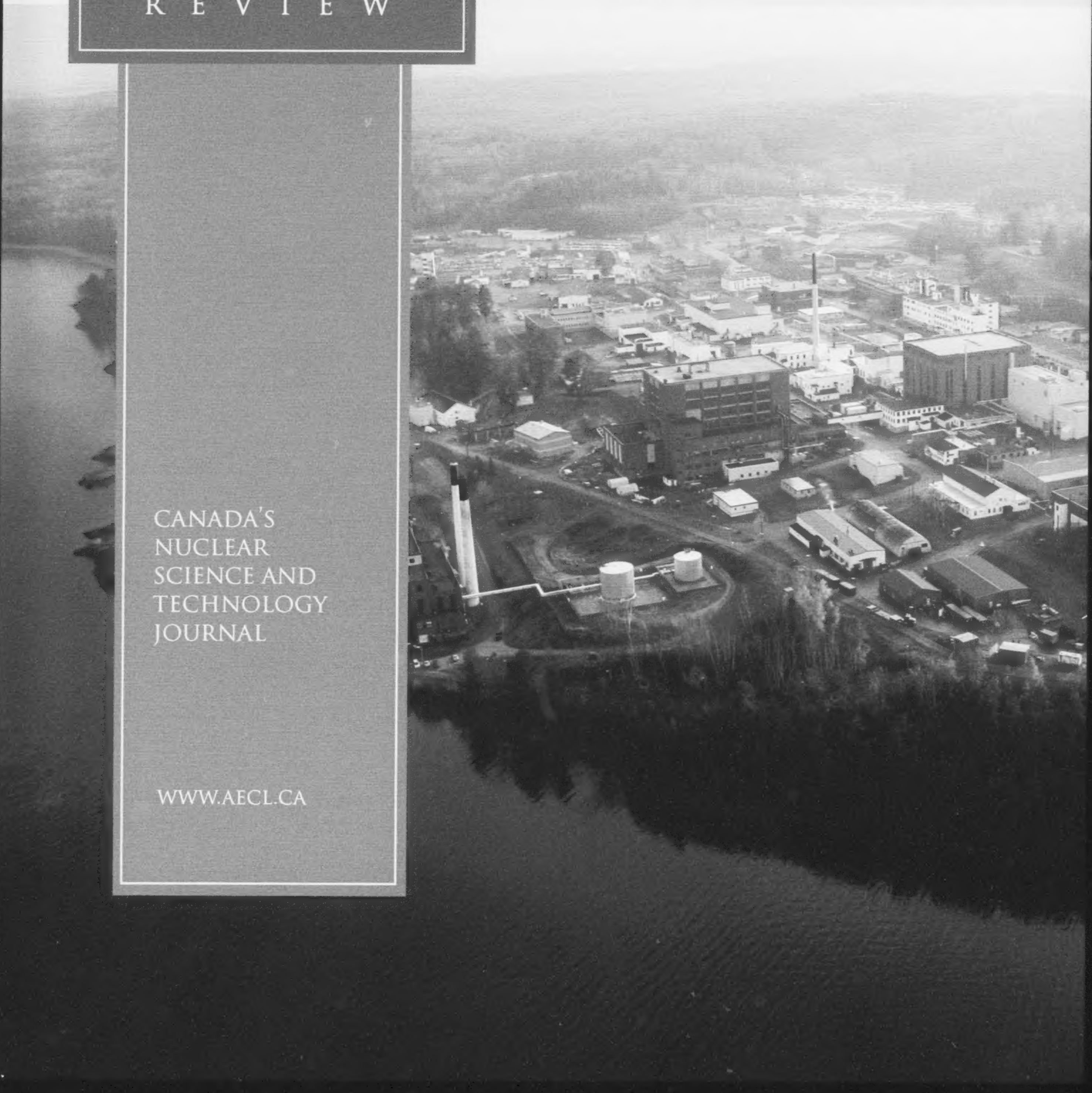

CANADA'S
NUCLEAR
SCIENCE AND
TECHNOLOGY
JOURNAL

WWW.AECL.CA

AECL NUCLEAR REVIEW

AECL Nuclear Review showcases innovative and important nuclear science and technology that is aligned with AECL's core programs. The Journal welcomes original articles and technical notes in a variety of subject areas: CANDU Nuclear Industry; Nuclear Safeguards and Security; Clean Safe Energy including Gen IV, Hydrogen Technology, Small Reactors, Fusion, Sustainable Energy and Advanced Materials; Health, Isotopes and Radiation; and Environmental Sciences. The accepted peer-reviewed articles are expected to span different disciplines such as engineering, chemistry, physics, and biology.

AECL Nuclear Review welcomes Canadian and international research scholars and scientists from different disciplines to its new publication, which reflects the integration of scientific researchers and industrial practitioners.

ABOUT AECL

Atomic Energy of Canada Limited (AECL) is Canada's leading nuclear science and technology laboratory. For over 60 years, AECL has been a world leader in developing peaceful and innovative applications of nuclear technology through its expertise in physics, metallurgy, chemistry, biology and engineering.

Today, AECL continues its commitment to ensure that Canadians and the world receive energy, health, environmental and economic benefits from nuclear science and technology with confidence that nuclear safety and security are assured.

ACTING EDITOR
G.L. Strati, Manager, Mechanical Equipment Development, AECL

ASSOCIATE EDITORS
F.M. Courtel, Chemistry, AECL
A. Khalifa, Mechanical Engineering, AECL

EDITORIAL BOARD
C. Butler, Manager, R&D Operations, AECL
R. Didsbury, General Manager, R&D Operations, AECL
G.L. Strati, Manager, Mechanical Equpment Development, AECL
B. Sur, Director, Nuclear Science, AECL

Copyright © 2012 Atomic Energy of Canada Ltd. All rights reserved.

AECL NUCLEAR REVIEW

Volume 1, Number 1
June 2012

INVITED ARTICLES

Science and Technology Enabling Canada's Tier 1 Nuclear Sector
R. Walker
- 1 -

Assessing Long-Term Performance of CANDU® Out-of-Core Materials
R.L. Tapping, Y.C. Lu, D. Mancey and Z.H. Walker
- 5 -

FULL ARTICLES

Localized Corrosion of Nuclear Grade Alloy 800 Under Steam Generator Layup, Startup and Operating Conditions
Y. Lu
- 13 -

Nuclear Data and the Effect of Gadolinium in the Moderator
J.C. Chow, F.P. Adams, D. Roubstov, R.D. Singh, and M.B. Zeller
- 21 -

Measurements of the High Dose Rate Profiles Inside a Shutdown CANDU® Reactor
C. Jewett, J. Chow, D. Comeau, G. Jonkmans, B. Smith, B. Sur, D. Taylor, S. Yue
- 27 -

Optimization of the Spatial Mesh for Numerical Solution of the Neutron Transport Equation in a Cluster-Type Lattice Cell
R.S. Davis
- 35 -

Self-Excited Acoustic Resonance of Isolated Cylinders in Cross-Flow
A. Mohany
- 45 -

TECHNICAL NOTES

A Novel Boron-Loaded Liquid Scintillator for Neutron Detection
G. Bentoumi, X. Dai, E. Pruszkowski, L. Li, B. Sur
- 57 -

Inverse Collimator-Based Radiation Imaging Detector System
A. Das, B. Sur, S. Yue, G. Jonkmans
- 61 -

Anthropogenic Radionuclides in Ottawa River Sediment near Chalk River Laboratories
D.J. Rowan
- 67 -

SCIENCE AND TECHNOLOGY ENABLING CANADA'S TIER 1 NUCLEAR SECTOR

Dr. Robert Walker, President & CEO, AECL

Atomic Energy of Canada Limited, Chalk River Laboratories, Chalk River, Ontario, Canada, K0J 1J0

Welcome to the inaugural issue of Atomic Energy of Canada Limited's AECL Nuclear Review. We at AECL are dedicating this journal to the dissemination of the latest science and technology (S&T) information through the work of AECL and its partners, and by so doing, we will contribute to the advancement of the peaceful, safe and trusted use of nuclear technology for the betterment of Canada and the world.

AECL is Canada's premier nuclear science and technology organization. 2012 is a milestone year for AECL as it celebrates 60 years as a world leader in the development and deployment of peaceful and innovative applications of nuclear technology, enabled by its deep expertise in physics, metallurgy, chemistry, biology, ecology and engineering. Through its journey, AECL has contributed to the creation and sustainment of a strong domestic nuclear sector. Our nuclear sector today, without a doubt, has a strong foundation on which to build.

However, as we in the sector reflect on its future, we see immediately that today's world, which sets today's context for civil nuclear technology and nuclear energy, is far different than it was for much of the sector's previous history. Globalization, interconnected societies, climate change – these are each terms used to characterize today's reality. Our world has become smaller, interdependent, and more complex, with an accelerating pace of change. Science and technology, or more explicitly the globalization of science and technology, has contributed directly to this new reality.

The resultant dynamics in societies and nations are challenging leaders to adapt public policy to address simultaneously the competing priorities of public-sector debt and deficits, sustainable economic growth and the evolving needs of public health, safety and security. But with these challenges also comes opportunity – opportunity for those sectors that recognize and leverage their strategic advantage in a manner appropriately adapted to today's realities.

Canada is a Tier 1 Nuclear Nation

To chart a path to the future, one must first understand where one is today.

Canada is a Tier 1 Nuclear Nation - one of a small number of countries with a comprehensive nuclear sector. Canada is committed to nuclear energy, with nuclear utilities operating in three provinces. Our utilities have been consistently ranked as among the best in the world for safe, reliable performance. The standards are rightly very high. Our nuclear utilities reside in host communities where mutual respect and trust have been established and sustained. Canada has an internationally respected, independent regulator operating in a coherent legislative and legal framework that meets and exceeds international expectations. Canada is a sought-out and active contributor to the advancement and implementation of international nuclear safety and security policies and standards. Canada has a robust domestic supply chain from mining through manufacturing and services, anchored by a domestic nuclear reactor original equipment manufacturer (OEM). Canada has a vibrant network of colleges and universities that are educating our next generation of nuclear workers while providing the appropriate research to augment their training. And Canada has the AECL Nuclear Laboratories, the home of critical nuclear science and technology expertise and licensed infrastructure that contributes to Canada's nuclear policy, regulatory framework, operational effectiveness, education and technological capabilities.

Attributes of a Tier 1 Nuclear Nation that Build Strategic Advantage

A Tier 1 Nuclear Nation today; but what of tomorrow?

An answer to this question emerges through an assessment of the attributes – what "good" looks like - that would provide or sustain strategic advantage for our nuclear sector into the future. Following are a possible set of such attributes around which the nuclear sector could rally its collective efforts.

A Tier 1 Nuclear Nation has a supply chain that is internationally competitive, with a demanding domestic market to help establish its credentials. Being internationally competitive requires that we understand what provides this competitive advantage. It also requires an understanding of the unique social, economic and public policy needs of the market. Our domestic nuclear platform, the CANDU®, is particularly noteworthy; CANDU has a strategic advantage. It is important that we understand and leverage that strategic advantage in domestic and international markets, recognize how it is complementary to other nuclear platforms, and appreciate how it plays into the public-policy priorities of customer nations.

A Tier 1 Nuclear Nation has a credible regulator who attests to the world that the country's nuclear solutions are safe. A necessary ingredient to sustained public trust is a credible regulatory system founded in fact; good science is a core ingredient to good regulation. There are many issues where the voice of science is needed to both inform regulatory decisions and to underpin the technological solutions that must respond to regulatory direction.

A Tier 1 Nuclear Nation has a sustained supply of highly qualified people. This supply must be enabled by appropriate education, economic development and immigration policies and systems. We aspire to attract Canada's best and brightest into careers that span public policy and regulation, operations, education, engineering and manufacturing and research, science and technology. Sustaining highly qualified people is a matter of both quantity and quality; they must be supported by a system of enablers that promote the movement of people across government, academic and industry sectors.

A Tier 1 Nuclear Nation values innovation. Focussing our sector on technological innovation is enormously important, particularly in such a capital-intensive industry as ours, but indeed innovation has many aspects to it. Business innovation is about how we work and how we translate good ideas into operational or commercial success. For example, the concept of a performance-driven supply chain is a business innovation. As opposed to a customer saying to its suppliers "Here is a technical specification, please build to this specification", our industry could do as the aerospace and automotive sectors did decades ago, that is, say "Here is the performance objective, please provide the best solution to meet this performance within our stringent safety and security requirements". This approach rewards innovation by setting conditions that stimulate increased productivity and profitability. It also affords the opportunity to leverage our sector's unique technological advances for competitive advantage in other nuclear platform supply chains or in other markets.

A Tier 1 Nuclear Nation is resilient in the face of volatility in the market. The reality is that the nuclear-energy business tends to fluctuate episodically with new build and refurbishments as intensive a periodic opportunities interspersed with services. The challenge is how to sustain sector capabilities and capacity to be responsive and resilient to that reality. For example, a supply chain that is able to lever its technology, production and service offerings into non-nuclear sectors will expand its market space and sustain growth while building competitive advantage.

A Tier 1 Nuclear Nation exploits public-private partnerships. The nuclear business is capital intensive, with long lead times for project design through implementation. Access to long-term "patient" capital is a necessary ingredient to success. Innovative business models that bring together the strengths of the public and private sectors in managing program risk can provide competitive advantage.

A Tier 1 Nuclear Nation builds and sustains public trust. Public trust takes time to build, and can be all too easily lost. A simple reality must be acknowledged - humans have a natural inclination to fear radiation. Trust must be built on the principles of transparency, accountability, effective regulation, objective discourse – and on accessible science.

A Tier 1 Nuclear Nation has reliable domestic access to nuclear science and technology expertise and infrastructure. The advancement of nuclear technology, the sustainment of nuclear operations and the regulation of both the technology and operations require large-scale licensed science and technology facilities. These facilities must be capitalized and sustained through an appropriate sharing of public- and private-sector investments.

An assessment of Canada's status today relative to these attributes identifies both strengths and opportunities for improvement. How do we nourish our strengths and address the areas for improvement? One approach is through the effective use of science and technology.

Science and Technology Enables Strategic Advantage

Science and technology, appropriately harnessed, can be a key contributor to the realization of the above attributes, thereby enabling the strategic advantage of our nuclear sector. But where and how do we align effort across the science and technology community - and the investments being made in the efforts of this community - to help ensure we are sustaining our Tier 1 status?

Here are some thoughts regarding a framework for helping build this alignment, with reference to specific examples of how AECL's science and technology efforts are contributing.

S&T enables sector competitivity through CANDU's strategic advantage. CANDU's strategic advantage is rooted in the flexibility of its fuel cycles, which in turn provides the opportunity for CANDU to complement, not compete with, alternative nuclear reactor designs in markets where this fuel cycle flexibility is of strategic value. For example, AECL has continually strived to evolve the current CANDU reactor design, particularly through a program called CANDU-X, which evolved the CANDU design over the years into a supercritical water-cooled reactor concept, which meets the objectives of the Generation IV International Forum; a safer, sustainable, economical and more proliferation resistant and physically secure design that retains CANDU's original fuel cycle advantage.

S&T enables public trust through science-informed regulation. In light of the March 2011 Fukushima Diachi reactor accident, there is renewed regulatory focus on nuclear emergency response and on the long-term effects of low level radiation on humans and non-human biota. For example, AECL is working with a broad set of partners to advance the scientific community's understanding of the biological mechanisms associated with the long-term exposure of biota to low-level radiation in the environment. This scientific knowledge is critical to establishing the factual basis for regulation and for managing the response to nuclear incidents in the future.

S&T enables sector capability through its experiential learning for its highly qualified workforce. Engagement in nuclear science and technology activities is a powerful mechanism of experiential learning for students, policy makers, regulatory staff, operators, industrialists, scientists, engineers and technologists. For example, AECL's approach to the execution of its comprehensive suite of S&T activities is to value collaboration across a broad set of nuclear sector partners, as well as to make AECL's unique nuclear S&T facilities accessible to others for their needs.

S&T enables business innovation through a performance-driven supply chain. Science and technology helps translate nuclear utilities' and OEM performance specifications into cost-effective technological solutions, demonstrating that these solutions meet demanding safety requirements while at the same time driving commercial competitive advantage. For example, AECL is expanding its efforts to help Canadian Small- and Medium-Sized Enterprises (SMEs) in the nuclear supply chain not only advance their technological solutions but also validate that these solutions meet and exceed regulatory requirements.

S&T enables sector resilience through the development of dual-use technologies. Technological solutions developed to meet the very demanding requirements of the nuclear environment can also provide competitive advantage in other industry sectors. For example, AECL has a rich history of working with suppliers in the development of robotic tooling for nuclear reactor maintenance and repair. These robotic solutions have potential application in the harsh environments found in other industries, such as petro-chemical and mining.

S&T enables a holistic perspective through an integrated lifecycle outlook. The cost effectiveness of nuclear technology in general, and of nuclear energy in particular, requires a holistic view of the entire lifecycle including mining and fuel production, plant licensing, new build, operation, refurbishment, decommissioning and waste management. Science and technology can help inform the entire lifecycle design to improve overall system economics and to help identify the substantial cost and effectiveness drivers. AECL has the integrated S&T expertise and capabilities to nurture this holistic view within Canada's nuclear sector.

Conclusion

Canada has a rich history of success in nuclear technology, built over many decades. It is a solid foundation on which we can build. Sustaining Canada's Tier 1 nuclear status will require a shared vision of where we want to take our nuclear sector into the future. Science and technology has a critical role to play in this journey and AECL, through this new journal, intends to share information on the latest S&T advances that are helping our sector along this journey.

INVITED ARTICLE

ASSESSING LONG-TERM PERFORMANCE OF CANDU® OUT-OF-CORE MATERIALS

R.L. Tapping[A*], Y.C. Lu[A], D.S. Mancey[A] and Z.H. Walker[B]

[A] Atomic Energy of Canada Limited, Chalk River Laboratories, Chalk River, Ontario, Canada, K0J 1J0
[B] Candu Energy Inc., 2280 Speakman Drive, Mississauga, Ontario, Canada, L5K 1B1

Article Info
Keywords: steam generator corrosion, flow accelerated corrosion, carbon steel corrosion, CANDU® materials
Article history: Received 13 April 2012, Accepted 7 May 2012, Available online 30 June 2012.

* Corresponding Author: (613) 584-3311 ext. 43219, TappingR@aecl.ca

ABSTRACT

As so-called second-generation power reactors are approaching the end of their original design lives, assessments are being made to determine the feasibility and economics of extending plant life. Although components exposed to neutron and gamma irradiation are often those of most concern in terms of in-service ageing and continued fitness for service, ageing of out-of-core components can also limit the possibility of extended service life beyond design life. In CANDU® reactors, life extension decisions occur when the Zr-2.5Nb pressure tubes reach end of life, typically after about 25 years of service for the first CANDU-6 units. At the time of pressure tube replacements, the remaining life predictions for several other major components or systems provide the information required to determine life extension feasibility. Several CANDU reactors are currently being refurbished, with others planned, and experience to date shows that the steam generators, heat transport system piping and various balance of plant piping systems are typically those requiring careful assessment to ensure successful refurbishment. In this paper, we discuss AECL R&D that is oriented towards providing the chemistry and materials inputs required to assess current condition and predict future ageing of CANDU reactor out-of-core components and systems, and in particular steam generators (Alloy 800 tubing and carbon steel internals), feeder pipes and related heat transport system piping (carbon steel flow accelerated corrosion, feeder cracking). Systems and components that may impact future life will also be discussed, along with the related R&D, and this includes balance of plant system piping (feedwater piping and buried piping), cables and concrete structures.

1. Introduction

A significant challenge in determining the feasibility of extending the life of nuclear power plants is to quantitatively predict remaining life, up to 60 to 80 years of service, of existing components after 20 to 30 years of service to date. In some cases, there is no in-service record of degradation, which introduces uncertainty in predictive approaches that can be used to assess future component and system performance. Laboratory data are often conservative in predicting materials performance, although there are striking examples where laboratory data predicted in-service corrosion, for instance, the work of Coriou, which highlighted the susceptibility of Alloy 600 to stress corrosion cracking (SCC) in hot pure water [1]. In other cases, in-service degradation has occurred, which was not predicted by mechanistic studies. An example of this is the carbon steel cracking in primary heat transport system (PHTS) water at one CANDU plant, which remains unexplained mechanistically. Further, much of the laboratory data have been obtained using essentially static conditions in the sense that the test environment did not change significantly with time. It is well established that actual plant operation is such that key components such as SGs and PHTS components are subjected to fluctuating conditions; thus, over long operating lives, these components experience many changes in pH, chemistry, electrochemical corrosion potential (ECP), mechanical loading and temperature. The accumulation of these stresses and especially synergistic effects between them, on component condition has not been evaluated with laboratory testing but remains an issue for long term performance. Some approaches to this for SG tubing will be discussed.

In this paper, the focus will be on two key materials and issues; one is Alloy 800 steam generator (SG) tubing performance in CANDU service, and recent results from PWR reactor SG experience, which have resulted in a need to re-evaluate the R&D required to address this operating experience. The other is flow accelerated corrosion (FAC) and intergranular stress corrosion cracking (IGSCC) of carbon steel in various CANDU systems and components. These topics will be addressed in some detail, but other materials' aging and degradation issues of interest for the longer term will be mentioned, including those related to electrical cables, concrete structures and balance of plant piping, and the associated R&D in place to assess these components.

2. Alloy 800 Steam Generator Tubing

After more than 30 years of corrosion-free in-service experience with Alloy 800, there have been recent reports of secondary side IGSCC detected in this material [2], which requires understanding in order to determine whether this degradation is of wider concern, or even the start of a much more serious future concern [3]. To date, there has been no IGSCC of Alloy 800 in CANDU SG service, although there has been some secondary side pitting detected. Alloy 800 was originally selected for CANDU SGs because of its predicted excellent resistance to primary side SCC (PWSCC; primary water SCC), and no susceptibility to PWSCC has been found in laboratory testing or in service. Figure 1 schematically illustrates the relative behaviour of Alloy 800 and other Ni-base alloys to a range of environments, indicating its suitability for SG applications.

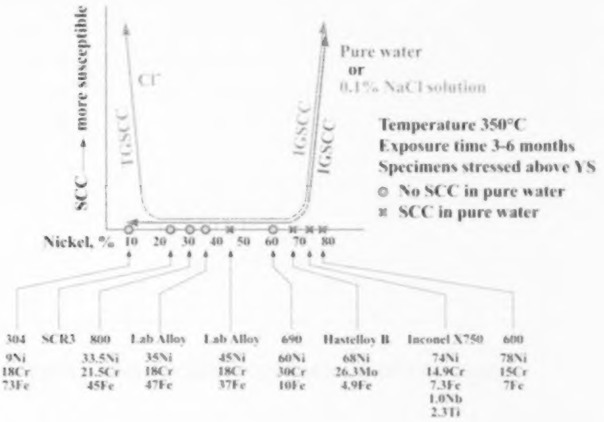

FIGURE 1

Schematical illustration of the SCC susceptibility of Alloy 800 and other Ni-base alloys in pure water or 0.1% chloride solution at 350°C. (Courtesy R.W. Staehle; based on Coriou data).

Table 1 summarizes the available in-service Alloy 800 SG tubing corrosion degradation data. Note that only in-service corrosion-related or corrosion-suspected data are included; there are many more incidents of tube damage and/or plugging as a consequence of mechanical issues, such as fretting against supports and loose parts damage. These data, along with the R&D data to be discussed shortly, indicate that a deterministic assessment of long-term future performance of Alloy 800 in CANDU service is impractical; rather a probabilistic approach is required that can be adapted to data as they become available.

2.1 Recent CANDU-Related R&D on Alloy 800

CANDU reactors have a variety of SG tubing materials, de-pending on their design and age. Table 2 summarizes these materials, along with a summary of any corrosion-related degradation experienced in CANDU service. Note that Indian Pressurized Heavy Water Reactors (PHWRs) have SGs tubed with both Alloy 400 (earlier PHWRs) and Alloy 800 (recent 220 MWe PHWRs, 540 MWe PHWRs and planned 700 MWe PHWRs), and there have been no reported corrosion-related issues with the Alloy 800 tubing. For some time, the R&D carried out on CANDU SG tube corrosion has addressed all three materials listed in Table 2, and in some cases Alloy 690TT has also been evaluated for benchmarking purposes. In the mid-1990's, it was also decided to use a consistent set of crevice chemistries as the basis for corrosion testing. These chemistries, outlined in Table 3, were determined based on hideout return and MULTEQ calculations from Bruce A SGs, where the crevice chemistry of the Alloy 600-tubed Bruce A SGs was taken as the basis because of significant corrosion experienced there starting in the late 1980's [4]. Addition of Pb compounds to these solutions increases the pH slightly. Two significant aspects dominated the Bruce A SG tubing degradation; one was the presence of sulphates (with several sulphuric acid excursions) and consequent acidic crevice chemistries, and the other was the inadvertent introduction of a lead blanket into one of the Bruce A SGs, resulting in a significant onset of IGSCC [5]. Hence there has been focus on the role of both impurities, and combinations of these with other potentially corrosive impurities, in evaluating the response of all four materials under plausible CANDU off-specification SG operating conditions. Much of this work has been carried out using electrochemical techniques, and results using this approach will be the emphasis in what follows.

TABLE 1

Summary of Alloy 800 SG Tubing Service and Associated Degradation Reports

Unit (in-service date)	Country	Degradation (first detected)	Location	SG Inlet T (°C)	Cause
Point Lepreau (1983)	Canada	Wastage/pitting (1987)	TTS^1 sludge pile	310	Incorrect Na/PO$_4$ ratio (wastage); condenser leaks (seawater; pitting)
Darlington (2003,2005 and 2006)	Canada	Shallow pitting (Reported in 2004)	TSP^2 (grids)	309	
Biblis A (1974)	Germany	Axial OD IGA/IGSCC^3 (1999; reported 2005)	Intra tubesheet (peripheral tubes)	313	Impurities; crevices (condenser leaks)
Unterweser (1979)	Germany	Axial OD IGA/IGSCC (2005)	TTS and TSP (grids)	318	Impurities; crevices (condenser leaks)
Almaraz (1981/83 in service; SG replacements 1996, 1997)	Spain	Circumferential IGSCC (?); denting	TTS	327	Not confirmed; based on inspection data (X probe); denting

2.2 Lead in combination with impurities

For some time, it has been recognized that lead (Pb) and sulphur/sulphates are implicated in the corrosion, and in particular intergranular (IGSCC), of SG tube alloys (for instance, see reference [6]). Lead is a potential life-limiting impurity for SGs, and is a secondary side impurity that is present in most, if not all, SGs. As has been discussed previously [6], there may be a relatively low threshold concentration for Pb-SCC of Alloy 600. Both Alloy 800 and Alloy 690 have generally better resistance to such IGSCC than Alloy 600, as typified by the excellent in-service performance, and also by laboratory investigations, especially when the evaluations are carried out in realistic off-specification chemistries. Given the need to assure reactor lives of 60 years or more, and consequently for major components such as SGs, it is necessary to determine that more resistant materials such as Alloy 690 and Alloy 800 have adequate resistance to PbSCC and other corrosive secondary side impurities for long service lives.

TABLE 2

Summary of SG Tube Materials in various CANDU Designs

Unit	Country	Tube Material	Supports	Experience
Pickering A	Canada	Monel 400 (Alloy 400)	Carbon steel lattice bars	Limited shallow pitting (significant sludge piles)
Pickering B	Canada	Monel 400 (Alloy 400)	Carbon steel trefoil broach plates	Significant pitting under deposits
Bruce A	Canada	Alloy 600 (slightly sensitized)	Carbon steel trefoil broach plates	IGA, IGSCC, fatigue (early failures of a few outer row tubes)
Bruce B	Canada	Alloy 600 (slightly sensitized)	Carbon steel trefoil broach plates	Minor IGA in one unit; FAC of support plates
Darlington	Canada	Alloy 800	Stainless steel lattice bars	Shallow pitting in a few tubes near 5th hot leg supports
Point Lepreau	Canada	Alloy 800	Stainless steel trefoil broach plates	Pitting and wastage (phosphate chemistry until 2000) of some tubes in sludge pile areas
Gentilly 2	Canada	Alloy 800	Stainless steel trefoil broach plates	No corrosion
Embalse	Argentina	Alloy 800	Carbon steel trefoil broach plates	Pitting of a few tubes; FAC of support plates
Cernavoda 1,2	Romania	Alloy 800	Stainless steel lattice bars	No corrosion
Wolsong 1	South Korea	Alloy 800	Alloy 600 formed lattice bars	No corrosion
Wolsong 2,3,4	South Korea	Alloy 800	Stainless steel lattice bars	No corrosion
Qinshan 3 1,2	China	Alloy 800	Stainless steel lattice bars	No corrosion

The use of highly concentrated alkaline or acidic solutions to simulate potentially corrosive crevice chemistries can produce overly conservative and possibly misleading results [7]. Preferable is the use of crevice chemistries that simulate the range that can be achieved within the experience base of chemistry upsets while operating on all volatile treatment (AVT) secondary side chemistry, as summarized in Table 3. Thus Alloy 800 SG tube samples, along with other SG tubing materials, were exposed to the chemistries outlined in Table 3 with the addition of various secondary side impurities, with a focus on Pb but looking for synergistic corrosive effects. Figure 2 illustrates some of the electrochemical data, which are assessed on the basis of passivity breakdown of the alloy, which is a measure of the susceptibility to corrosion under the test conditions. Parallel autoclave tests were used to assess the SCC susceptibility under the same conditions. The results have been summarized in Table 4, and are also compiled into "recommended" pH vs. potential zones as illustrated in Figure 3 [1].

As part of this study the role of sulphates and reduced sulphates (thiosulphates, for example) was examined, along with examination of the interaction of Pb with sulphates, and whether sulphate could act to reduce the corrosivity of Pb, for example by complexing the Pb as an insoluble and non-corrosive complex. As shown in Table 5, sulphate does not reduce the corrosivity of Pb to SG tubing. In fact, reduced sulphates, thiosulphates and tetrathionates, for example, may be the most aggressive form of sulphur found on the secondary side of SGs. The reduction of sulphate to sulphide during operation is well-known [6], as is the formation of intermediate oxidation state sulphur (IOSS) such as thiosulphate and tetrathionate following re-exposure to aerated or oxidizing conditions during SG layup, but only recently has it been shown clearly that these chemistries can cause severe corrosion in service as a consequence of typical, although not optimal, operating conditions [5]. Given the widespread presence of sulphates in SGs, it seems likely that "reduced sulphate" or more precisely IOSS degradation is more widespread than has been reported.

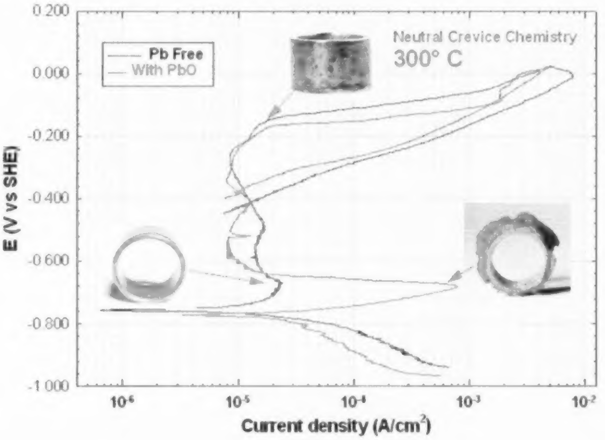

FIGURE 2

Potentiodynamic polarization curves of Alloy 800 SG tubing obtained under simulated neutral SG secondary side crevice chemistry conditions in the presence and absence of 500 ppm PbO contamination.

TABLE 3

Compositions of Simulated Crevice Solutions used for CANDU SG Tube Corrosion Evaluations

Simulated Crevice Environment	pH at temperature (°C)	Solution Composition*	Neutral pH at T for this composition
"Neutral" crevice ("reference solution")	pH_{300} 6.10 pH_{150} 6.03	0.15M Na_2SO_4 0.3M NaCl 0.05M KCl 0.15M $CaCl_2$	pH_{300} 5.16 pH_{150} 5.56
Alkaline crevice	pH_{300} 9.26 pH_{150} 10.10	Add 0.4M NaOH to "reference solution"	pH_{300} 5.14 pH_{150} 5.56
Acidic crevice	pH_{300} 3.22 pH_{150} 2.32	Add 0.05M $NaHSO_4$ to "reference solution"	pH_{300} 5.16 pH_{150} 5.56

Figure 3 shows that Alloy 800 is stable in a range of secondary side chemistries, and should be corrosion resistant to chemistry transients that result in crevice chemistries within this range. What remains to be determined is the allowable time to remain outside the range, and the effect of multiple transients in and out of the range. These are conditions that can occur during operation, and extended service lives imply that these conditions might occur more often. Both Alloy 800 and Alloy 690 have much larger safe ECP and crevice chemistry ranges than Alloy 600 or Alloy 400, and thus provide more protection against transients. It remains to be determined if there is a cumulative effect of transients that can affect SG tubing behaviour beyond that known from service experience to date, or from laboratory testing [6]. What also remains to be determined is the effect of cold work or surface damage on long term behaviour. Recent examinations of Alloy 800 tubing removed from a CANDU SG showed shallow pitting in an area with possible cold work [9]. Cold work can occur, for example, where tubes intersect support structures, as well as from fabrication defects, so cold work impacts on tube life could be significant over long service lives.

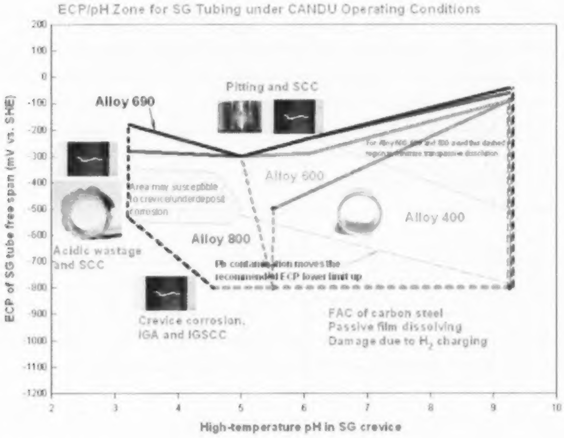

FIGURE 3
Recommended ECP/pH zone with minimized corrosion for SG alloys at CANDU SG operating temperature.

Recent examinations of tubing removed from one Canadian CANDU SG suggested that an ageing effect might be increasing the corrosion susceptibility of the "aged" (ex-service) tubing, based on results from electrochemical tests, such as those used to develop the data shown in Figure 3. The major difference between the aged material and other materials was that the Ti/C ratio of the ex-service material was very high, approximately 28 compared to the specification of >12, although this would normally be predicted to have a positive effect. As a consequence of this finding, a series of tests was carried out on archived and ex-service tubing to determine if there was any evidence for an aging effect. Steam generator (SG) tubing removed from three CANDU stations with service life spanning from two to 27 years was examined as part of a material aging assessment. It was not possible to find archived materials that matched the heats of materials removed from service. Table 5 summarizes the ex-service tubing assessed and results of the tests. No evidence of an aging effect was found, although it was noted that the aged materials appeared to have more boron on the grain boundaries than the archived materials. It is not clear that this latter result has any significance [10].

In order to better predict future behaviour of SG component life, and in particular tube life, R&D is also underway on probabilistic methodologies to make these predictions. Until recently, as noted earlier, Alloy 800 SG tubing had not been reported to have experienced any significant corrosion in service times up to 30 years or more. Although this is still the case for CANDU SGs, recent European experience shows that Alloy 800 can experience significant in-service degradation under certain conditions. This in-service database, along with laboratory data, can be used to develop a Bayesian model for Alloy 800 tube performance over long times, the "degradation free lifetime". The details will not be reproduced here [11], but the conclusion is that Alloy 800 should perform reliably for at least 60 years based on the current data. It should be remembered that most of the laboratory data, as noted above, were generated using static (in time and concentration) tests under various chemistries, but not under transient or oscillating conditions. Thus, work is continuing to address the possible consequences of the accumulation of minor chemistry transients on the long term stability of Alloy 800.

TABLE 4
Impurity Mixes Used to Evaluate Susceptibility of SG Tubing to Secondary Side Corrosion

Impurity Mix	Effect on Alloy 800
$PbSO_4$	No evidence SO_4 could immobilize Pb and reduces effect of Pb on SG tube degradation.
PbCl and PbS	More aggressive than PbO to all SG tube alloys
$PbO + SiO_2$	Silica appears to inhibit Pb-induced degradation of SG tube alloys
Al, PbO + Al	Al impurities apparently have no effect on corrosion
Cu, PbO + Cu	Cu contamination increases ECP and pitting susceptibility (oxidant effect)
Mg, PbO+Mg	Mg increases ECP and decreases pitting potential. The effect of Mg on PbSCC requires further investigation.

3. Carbon steel corrosion

CANDU reactors have used carbon steel (A106 Grade B) for PHTS piping that connects the fuel channels to the rest of the PHTS circuits. Some time ago it was recognized that magnetite fouling of the primary side of CANDU SG tubing was a consequence of the corrosion of, and deposition of corrosion products from, carbon steels. Subsequently it was recognized that this corrosion product deposition was largely a consequence of flow accelerated corrosion (FAC) of corrosion products from, carbon steels. Subsequently, it was recognized that this corrosion product deposition was largely a consequence of flow accelerated corrosion (FAC) of the outlet feeder piping ("feeders"), and was exacerbated by unusually low Cr contents of the steel and local hydraulic behaviour. Similarly, several cases of unexpectedly high FAC rates of carbon steel have occurred in the secondary side of CANDU SGs, where fouling-induced hydraulic disturbances have resulted in unanticipated damage. Again, the role of Cr has been a factor in determining the pattern of damage. In terms of predicting carbon steel component life, these factors need to be included, although they were not at the time of initial design. Finally, the intergranular cracking found in some outlet feeders at one CANDU station (PLGS), although apparently limited to just 13 feeders at the one station [12], and a repaired feeder-to-feeder weld, remains a concern given the several thousand similar feeder pipes in service in other reactors and, to date, no unambiguous mechanistic interpretation of the cracking.

TABLE 5
Ex-Service Alloy 800 Tubing Examined and the Results Summarized

STATION	DNGS	DNGS	CNG2	PLGS
Ex Service Tube ID	D4 SG3 R54C76	D4 SG1 R49C61	G2 SG3 X69Y54	PL SG3 R32C65
Removed	1995	2003	Apr. 2009	Dec. 2009
In-Service Date	Jun. 1993	Jun. 1993	Oct. 1983	Feb. 1983
Calendar Year	2	10	25.5	26.8
EFPY/Hot Years	1.6/1.7	8.4/8.7	20.4/-[3]	20.94/21.99
Surface Chromium	No depletion was detected	No depletion was detected	No depletion was detected	No depletion was detected
Electrochemical corrosion behaviour	Identical to archived new tubing	Identical to archived new tubing	Identical to archived new tubing	Identical to archived new tubing
Chemical compositions	Met with ASME SB 163 Standard	Met with ASME SB 163 standard	Met with ASME SB-163 Standard	Met with ASME SB-163 Standard
Hardness (HV)	160	165	163	173
Grain Size (µm)	13.8/15.0	11.0	8.2/8.8	9.4/8.5
Cr depletion at grain boundaries	Not detected	Not detected	Not detected	Not detected
Boron segregation at grain boundaries		Observed	Observed	Significant

Feeder piping corrosion

General corrosion of carbon steel under the pH ~10 chemistry of a CANDU PHTS is low enough that long-term acceptable performance is expected. However, although FAC rates under CANDU PHTS operating conditions are very low on average, the FAC is localized to specific areas of the outlet piping where rates of wall loss up to 175 µm/year have been measured. Given that the feeder pipes have wall thicknesses of ~8 mm, these wear rates have a significant impact on feeder life, in some cases requiring premature replacement [12]. Figure 3 provides an overview of the feeder pipes that have been replaced in Canadian CANDU reactors as a consequence of wall thinning. As has been discussed previously [14], the FAC mechanism responsible for the wall thinning found in CANDU outlet feeders is primarily a consequence of the flow of Fe-unsaturated water into the outlet feeders. The PHTS coolant becomes significantly unsaturated in Fe as it traverses the non-ferrous zirconium alloy pressure tubes and is heated to ~300°C in the process, thus leaving the water able to dissolve more Fe [15]. This, combined with turbulent flow and high mass transfer as the coolant enters the typically tight radius bends of the outlet feeder piping, results in wall-thinning rates high enough to reduce feeder pipe life significantly (although note that these rates are low compared to those found at lower temperatures in feedwater piping). Based on available solubility data for Fe and Fe_3O_4 some reduction in rate can be achieved by lowering the pH to ~10.2 to 10.4 from the typical range of 10.2 to 10.8, and experiments are underway to determine if the pH can be lowered further and achieve lower FAC rates. Chemistry modifications are of value to mitigate feeder thinning in operating reactors. For new reactors, and for replaced feeders, for instance during refurbishments for extended life, it has been shown that specifying Cr contents of the steel to be ≥0.3 wt % reduces feeder thinning rates by 50%, demonstrated by both in-service performance and in- and out-reactor laboratory testing [16]. Typically the Cr contents of early CANDU reactor feeder pipes are very low, <0.02 wt % for instance, which is a consequence of the low Co specification originally imposed in order to reduce corrosion product activation. More recent reactors, and all new CANDU-6 reactors, specify higher Cr steel, while remaining within the A106 specification. Given that the feeder pipe FAC mechanism is well understood and predictable [16], this degradation mechanism can be readily managed for existing and extended design lives.

Laboratory tests using AECL's FAC loop have demonstrated that the production of hydrogen by the FAC reaction can be completely suppressed by the presence of very low concentrations of dissolved oxygen, and that this suppression occurs without significant changes in the rate of FAC. In these experimental loop tests, abrupt changes in dissolved oxygen concentration were made to stop and start the entry of atomic hydrogen into the test samples and hydrogen effusion probes used to measure the diffusion of hydrogen through carbon steel [17].

Of more concern than FAC, because there is not as good an understanding of the mechanistic details, has been feeder cracking. Although all of the early CANDU-6 reactors have similarly fabricated feeder pipes, only those at Point Lepreau Generating Station (PLGS) have experienced cracking. Figure 4 shows the chronology of the detected cracks. The cracking experienced at PLGS is intergranular stress corrosion cracking, both from the inside and outside surfaces with no obvious grain boundary segregation of impurities. The feeder bends at these early reactors were heavily cold-worked during fabrication [12]. The most plausible explanation for this cracking is that low temperature creep cracking of highly cold-worked material, combined with FAC-induced hydrogen from the inside surface, are contributing to the cracking [18]. To test this hypothesis, a number of experiments have been carried out in the FAC test rig with pre-cracked test spool pieces subjected to an applied load. In these experiments, the FAC process can be turned on and off by modifying the oxygen content, and thus the role of FAC-induced hydrogen can be determined. Results to date suggest that FAC hydrogen is a contributor to the IG-SCC; with FAC-induced hydrogen present, the crack growth rate is significantly faster than when hydrogen generation is suppressed (but FAC continues) [17].

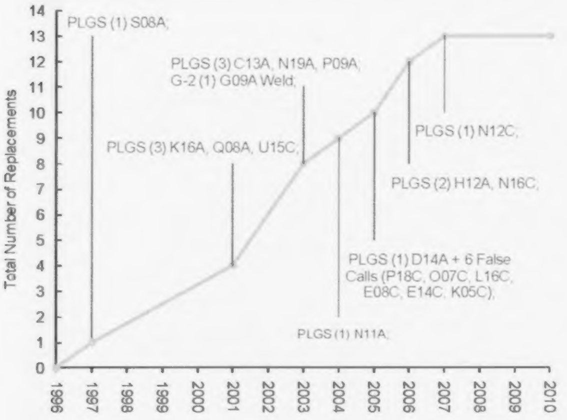

FIGURE 4
Historical Record of Point Lepreau Outlet Feeder Cracking.

Separate tests have demonstrated that low temperature creep of A106B carbon steel is measurable, with crack growth rates comparable at 300°C to those measured for feeder cracks at PLGS, for heavily cold-worked material stressed close to yield [18].

The role of operating transients on feeder cracking has not been investigated. What remains to be understood is why the PLGS IGSCC has not occurred in feeder piping elsewhere (although IGSCC was observed in a repaired feeder weld at Gentilly-2 NGS). For more recent reactors, the feeder bends are stress relieved and thus are not expected to be at significant risk of cracking.

4. Other systems

Most of the secondary side of power plants is constructed with carbon steel piping. Recently, after the discovery of the ubiquitous nature of FAC under feedwater conditions, FAC-resistant materials (Cr-Mo alloys; stainless steels) are used in high susceptibility areas such as susceptible geometries, low pH, two-phase flow, and flows with Fe concentrations less than saturation, such as moisture separator reheater piping [19] are used. FAC of secondary side systems and piping can be engineered out with appropriate materials selection, designed to avoid turbulence and impingement, and appropriate operating chemistry. For older plants, inspection is a key part of the management approach, and at CANDU plants, the CHECWORKS code of the Electric Power research Institute (EPRI) is applied. AECL has also applied this code, along with CFD (computational fluid dynamics) calculations, to assess FAC of carbon steel components on the secondary side of SGs. There have been several instances of secondary side FAC of key secondary side SG components, as noted in Table 2. R&D continues on improving the predictability of CHECWORKS in terms of quantitation of expected wall thinning rates at high risk locations, using accumulated plant data as a baseline for predictions, along with improved understanding of the key factors influencing FAC of carbon steel. For buried piping, the use of non-metallic materials is being considered, and modelling of service water piping systems has shown where conditions particularly susceptible to microbiological corrosion, or microbiological corrosion (MIC) (for instance, vertical deadlegs), can be designed out. In addition, the R&D has provided the data needed for improving operating specifications to minimize the ingress of nutrients that can lead to biological growth and subsequent MIC.

Low temperature piping, typical of that used in service water systems, is also susceptible to localized corrosion, either under deposits (tuberculation) or as a consequence of MIC attack. In collaboration with EPRI, AECL has been developing models of tuberculation and MIC to incorporate into EPRI's BPWORKS code, which is used to identify high risk areas where inspections of piping should be carried out. This is particularly important for buried piping, where the consequences of undetected degradation can be significant, and the cost of carrying out unnecessary inspections is also a major concern. Thus, R&D in this area is focused on inspection technology developments, along with improved risk ranking techniques.

Other systems of concern for long life, and where CANDU-related R&D is being carried out, include concrete structures, cables and the calandria vessel. The main issue with concrete is that many concrete structures must remain intact and act as a barrier to prevent release of nuclear materials for very long times. Concrete degradation mechanisms for unirradiated structures are well known, although work remains to be done on irradiated concrete. The key life management issue for concrete is improving inspection technologies such that non-destructive methods of assessing concrete structure condition can be quantified. Models for the degradation of concrete over long times may need to be developed to relate inspection findings to life prediction. For cables, aging models have been developed, and related to inspection results from various destructive and non-destructive techniques. To date, experience with cables in various CANDU reactors, and in AECL's NRU reactor, all show that the cables are in good condition and can remain in service. Finally, the calandria vessel, which contains the heavy-water moderator, at 60 to 70°C, which surrounds the pressure tubes, requires some assessment of remaining life. This vessel experiences a neutron flux up to 2x1021 n/cm^2, and is fabricated from type 304L stainless steel. There are essentially no data available showing the long-term effects of neutron irradiation of this material at low temperatures, but several analyses using extrapolations from available data indicate that the vessel and vessel welds would not have experienced any significant irradiation-induced effects after 30 years of service, and can remain in service. To quantify this, it is proposed to destructively examine other structures from inside the calandria vessel in order to assess any irradiation effects.

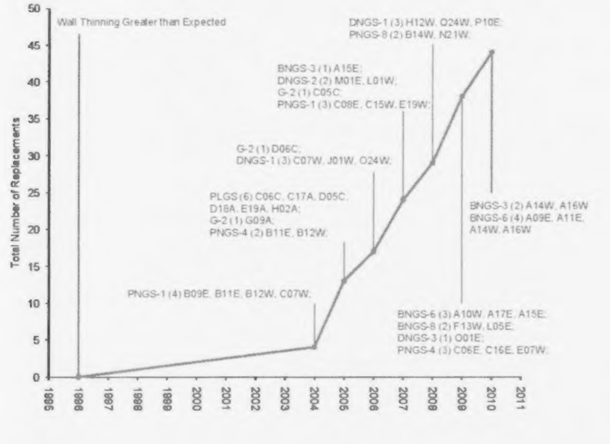

FIGURE 5
Historical record of outlet feeder replacements in CANDU reactors because of feeder thinning.

5. Conclusion

Materials performance remains the primary long-term risk for most industrial systems, and especially for nuclear power plants. Predicting that performance quantitatively has always posed challenges [20], and an even bigger challenge is to predict performance for extended reactor lives of 60 to 80 years. For CANDU reactors, life extension implies replacement of the fuel channel assemblies, and hence the materials issues relate to whether or not out-reactor components and systems need to be replaced. In most cases, in-service experience and laboratory data indicated that passive components such as steam generators, piping, etc. do not need replacement. Significant exceptions are where Alloy 600 and Alloy 400 were used for used for SG tubing, and where carbon steel was used for secondary side SG support structures. The most recent CANDU reactors, built since the 1980's, and those being refurbished now, use designs, components and materials, in addition to appropriate operating and maintenance strategies, based on results from R&D programs carried out at AECL's laboratories. These results indicate that Alloy 800 SG tubing, Cr-enriched carbon steels and appropriately designed service water systems can provide low-risk long term service.

REFERENCES

[1] H. Coriou, L. Grall, P. Olivier and H. Willermoz, 1968, "Influence of Carbon and Nickel Content on Stress Corrosion Cracking of Austenitic Stainless Alloys in Pure or Chlorinated Water at 350 C", in Fundamental Aspects of Stress Corrosion Cracking; NACE-1, NACE, Houston, pp. 352-359

[2] J. Slade, V. Moroney, J. Gorman and T.S. Gendron, 2007, "A CANDU Utility Perspective on Using World Experience to Manage Alloy 800 SG Tube Degradation", Proceedings 13th International Conference on Environmental Degradation of Materials in Nuclear Power Systems, Whistler, B.C., Canada

[3] R. Kilian, J. Beck, H. Lang, T. Schönherr, and Martin Widera, September 2010, "Root Cause Analysis of SG Tube ODSCC Indications within the Tube Sheets of NPP Biblis Unit A", Proceedings of the International Symposium, Fontevraud-7, Avignon, France, Paper A154-T06

[4] Y.C. Lu, 2010, "Effect of Hazardous Impurities on Steam Generator Tube Degradation", Proceedings ICONE-18, Xi'an, China, Paper ICONE18-30120

[5] K. Sedman and D. Durance, November 2009, "Update of the SG Tube Intergranular Attack/Stress Corrosion Cracking in Bruce Unit 4, Proceedings 6th CNS International Steam Generator Conference, Toronto

[6] R.W. Staehle and J.A. Gorman, 2004, "Quantitative Assessment of Sub-modes of Stress Corrosion Cracking on the Secondary Side of Steam Generator Tubing in Pressurized Water Reactors", Corrosion, Part 1: 59 (2003) p.931-994; Part 2: 60 (2004) p.5-63; Part 3: 60, pp.115-180

[7] P.V. Balakrishnan, S.M. Pagan, A.M. McKay and F. Gonzalez, 1995, "Hideout and Hideout Return: Laboratory Studies and Plant Measurements", Control of Corrosion on the Secondary Side of Steam Generators, Airlie, Virginia, NACE, pp. 683-708

[8] Y.C. Lu, 2007, "Define Optimal Conditions for Steam Generator Tube Integrity and an Extended Steam Generator Service Life", Proceedings ICONE-15, Nagoya, Japan, Paper ICONE15-10854

[9] Y.C. Lu, G. Goszczynski and S. Ramamurthy, July 2009, "Degradation of Alloy 800 under Steam Generator Secondary Side Crevice Conditions", Pro-ceedings of the 17th International Conference on Nuclear Engineering, ICONE-17, Brussels, Belgium, Paper ICONE17-75695

[10] Y. Lu, S. Ramamurthy, G. Goszczynski, 2012, "An Aging Assessment on Ex-Service Alloy 800 Steam Generator Tubing", Nuclear Engineering and Design, 242, pp. 91-99

[11] Y.C. Lu, R.L. Tapping and M.D. Pandey, November 2009, "Degradation of Alloy 800 Steam Generator Tubing and its Long-Term Behaviour Predictions for Plant Life management", Proceedings 6th CNS International Steam Generator Conference, Toronto

[12] J.P. Slade and T.S. Gendron, August 2005, "Flow Accelerated Corrosion and Cracking of Carbon Steel Piping in Primary Water – Operating Experience at the Point Lepreau Generating Station", Proceedings 12th International Conference on Environmental Degradation of Materials in Nuclear Power Systems – Water Reactors, Salt Lake City, U.S.A., pp. 773-784

[13] Z.H. Walker, July 2004, "Managing Flow Accelerated Corrosion in Carbon Steel Piping in Nuclear Plants", Proceedings of ASME PVP Conference (PVP2004), San Diego, U.S.A., Paper PVP2004-2251

[14] R.L. Tapping, 2008, "Materials Performance in CANDU Reactors: The First 30 years and the Prognosis for Life Extension and New Designs", Journal of Nuclear Materials, 383, pp. 1-8

[15] D.A. Guzonas and L. Qiu, October 2004, "A Predictive Model for Radio-nuclide Deposition Around the CANDU Heat Transport System", International Conference on Water Chemistry of Nuclear Reactor Systems, San Francisco, U.S.A., pp.2079-2086

[16] Z.H. Walker, A.J. Elliot, D.S. Mancey and B. Rankin, October 2006 , "Resistance of SA-106 Carbon Steel containing >0.30 wt% Cr to Flow Accelerated Corrosion Under CANDU Reactor Outlet Feeder Pipe Conditions", International conference on Water Chemistry of Nuclear Reactor Systems, Jeju Island, Korea

[17] D.S. Mancey, AECL, unpublished results

[18] M.D. Wright, AECL, unpublished results

[19] B. Chexal, et al., 1998, "Flow-Accelerated Corrosion in Power Plants", EPRI Report TR 106611-R1

[20] P.L. Andresen, T. Angeliu and L.M. Young, February 11-15, 2001, "Immunity, Thresholds and Other SCC Fiction", in Chemistry and Electrochemistry of Corrosion and Stress Corrosion Cracking: A Symposium Honouring the Contributions of R.W. Staehle, edited by R.H. Jones, TMS, New Orleans, Louisiana, pp. 65-82.

FULL ARTICLE

LOCALIZED CORROSION OF NUCLEAR GRADE ALLOY 800 UNDER STEAM GENERATOR LAYUP, STARTUP AND OPERATING CONDITIONS

Y. Lu*

Atomic Energy of Canada Limited, Chalk River Laboratories, Chalk River, Ontario, Canada, K0J 1J0

Article Info

Keywords: steam generator, alloy 800, localized corrosion, potentiodynamic polarization, crevice corrosion

Article history: Received 19 March 2012, Accepted 25 June 2012, Available online 30 June 2012.

*Corresponding Author: (613) 584-3311 ext. 43258, Luy@aecl.ca

ABSTRACT

The localized corrosion resistance of nuclear-grade Alloy 800, which is one of the preferred steam generator (SG) heat exchange tube materials of CANDU and PWR reactors, was studied under simulated SG secondary side crevice chemistry conditions at ambient temperature as well as at elevated temperatures. Series of cyclic potentiodynamic polarization tests were performed to study the localized corrosion resistance of Alloy 800 as a function of chloride ion concentration in the SG crevice solution at 40°C, 150°C and 300°C. Based on the experimental results, empirical equations were provided for calculating the pitting potential of nuclear grade Alloy 800 in the SG secondary side crevice chemistries with different levels of chloride concentration at SG layup, startup and operating temperatures.

Introduction

Significant corrosion degradation of steam generator (SG) tubing has been found in the SG secondary side worldwide. Pitting corrosion and crevice/underdeposit corrosion, intergranular attack (IGA) and stress corrosion cracking (SCC) are among the possible major forms of degradation for SG tube materials. The impurities can hide out and concentrate in SG crevices, leading to an aggressive local chemistry. Corrosion-related SG tube degradation may take place in tube/tube-support crevices, tube/tubesheet crevices or under sludge deposits when the secondary side environment contains oxidants and/or is contaminated with chloride. Experimental data suggest that all SG tube materials can be susceptible to corrosion degradation under some particular off specification SG crevice chemistry conditions [1]. The tolerance to the chemistry upset for each SG tube alloy is different. In recent years, AECL has been working proactively to deal with the SG degradation issues. An effective way to minimize the SG material degradation is through effective water chemistry control. To support the proactive materials degradation management (PMDM) of SG materials, high temperature electrochemical tests were performed under plausible SG crevice chemistry conditions for all SG tube alloys. This knowledge has been documented in the form of a recommended ECP/pH zone that can be incorporated into a program for SG system monitoring [1, 2]. Tests, especially simulated accelerated corrosion tests and SCC tests, have been performed to verify the boundary leading to SG tube degradation under transient and off-specification conditions [3]. The recommended ECP/pH zone could be used as a tool for safeguarding the integrity of SG tubing, with the expectation that operation in these "safe" zones will assure at least 60 years of service.

It should be noted that the plausible crevice chemistry conditions, which were used to develop the recommended ECP/pH maps of different SG alloys, were based on formulations suggested by Pagan used in previous work [4] and later verified by Burton and Turner [5]. However, based on an average of all Darlington Nuclear Generating Station hideout return surveys since 2001, McKay and Pagan found that the SG crevice solution may not always be as aggressive as previously suggested [6]. It is therefore necessary to evaluate how the boundaries of the recommended zones change as a function of the concentrations of SG impurities. Chloride is one of the major SG impurities that cause the break down of the passive film and initiate localized corrosion in passive metals, including SG tubing materials [1]. Work has been performed by AECL to study the impact of chloride ion concentration on the upper boundary of the safe ECP/pH zone leading to SG tube alloy degradation. The overall objective of this task is to evaluate the effect of chloride concentration on the SG tube corrosion degradation. The results will provide information to determine how the safe ECP/pH zone boundaries move with variation of SG impurity concentrations at the same high temperature pH. Acidic crevice chemistry is excluded from the recommended ECP/pH zone and according to a study by Balakrishnan CANDU SG crevice chemistry is normally in the neutral pH range even under condenser leakage conditions [7]. Therefore, the effect of chloride ion concentration on the corrosion of SG tubing was focused on neutral crevice chemistry conditions. This paper summarizes the high temperature electrochemical experimental results from these studies.

1. Experimental Conditions

1.1 Test Material

Samples for electrochemical measurements were 10 mm long segments cut from ASTM B 163 standard seamless heat exchanger tubes. In this paper, only data from Alloy 800 SG tubing will be presented. Nuclear grade Alloy 800 SG tubing tested was from Noranda Metal Industries Ltd., where the final heat treatment was a bright annealing at 980 ± 10°C. The outer diameter (OD) surface of the test specimens was finished by grinding with 600 grit silicon carbide paper and ultrasonically cleaning first with acetone, and then with ethanol before the tests. The detailed information on the tube material is listed in Table 1.

TABLE 1
Detailed Information on the SG Tube Materials for Tests (Based on Mill Test Certificates)

Alloy	Heat No.	Size	Composition wt %												
			C	Si	Mn	P	S	Cr	Ni	Co	Ti	Cu	Al	N	Fe
800	HH9943A	0.625 x 0.044" Wall (15.88 x 1.12 mm)	0.015	0.10	0.80	0.009	0.002	21.70	34.11	0.012	0.42	0.03	0.41	0.028	42.41

1.2 Test Environments

The corrosion susceptibility of Alloy 800 SG tubing material was evaluated by performing a series of electrochemical measurements under the SG crevice conditions shown in Table 2 through Table 4. The crevice solutions were determined by referring to simulated representative CANDU SG crevice environments based on the systematic SG hideout return results from CANDU Nuclear Generating stations, and on analysis of the intact tube/bar crevice deposits [4]. To study the effect of the chloride concentration on the corrosion degradation of Alloy 800 SG tubing, different amounts of chloride were added to the neutral crevice chemistry by meeting the following criteria:

1. The total concentration of sulphate in the crevice solution should remain unchanged (or the changes are negligible).
2. The pH of the solution at temperature should be maintained at, or at least close to, a fixed value by using pH adjusters, such as 10^{-4} M NaOH or HCl.

The calculation of the at-temperature pH values for the selected crevice solutions were performed using the OLI software, Version 2.048, from OLI Systems Inc. (NJ, USA). The detailed method and theories used for the calculation in Stream Analyzer can be found in reference [8] and its citations. Stream Analyzer has two embedded activity frameworks. The one selected for this report was the Aqueous H^+ Framework [8].

In this work, only the bulk chloride concentration of the solution is considered. Chloride concentration gradient on the alloy surface is not significant if Alloy 800 is passive. Under such conditions, the passive current density is so low that the potential gradient in the solution near the electrode surface can hardly result in any significant chloride ion gradients near the passive surface.

TABLE 2
Neutral Crevice Solution with Different Chloride Concentrations for Tests at 300°C (pH 300°C = 6.10) Unit: mol/kg

$[Cl^-]$	Na_2SO_4	NaCl	KCl	$CaCl_2$	HCl	NaOH
0.01	0.1500	0.0027	0.0005	0.0014	4.15E-03	
0.1	0.1500	0.0443	0.0074	0.0222	3.98E-03	
0.65	0.1500	0.3000	0.0500	0.1500		
1	0.1500	0.4615	0.0769	0.2308		2.2E-04
4	0.1500	1.8462	0.3077	0.9231		6.2E-04

TABLE 3
Solutions for Tests Performed at 150°C (pH 150°C = 6.03) Unit: mol/kg

[Cl]	Na_2SO_4	NaCl	KCl	$CaCl_2$	HCl	NaOH
0.01	0.15	4.57940×10^{-3}	7.63000×10^{-4}	2.29000×10^{-3}	8.29711×10^{-5}	
0.1	0.15	0.0461173	7.68600×10^{-3}	0.0230590	8.41592×10^{-5}	
1	0.15	0.461538	0.0769230	0.230769		1.10203×10^{-5}
4	0.15	1.846154	0.307692	0.923077		5.82434×10^{-5}

TABLE 4
Solutions for Tests performed at 40°C (pH 40°C = 6.83) Unit: mol/kg

[Cl]	Na_2SO_4	NaCl	KCl	$CaCl_2$	HCl	NaOH
0.01	0.15	4.61568E-03	7.69044E-04	2.30814E-03	5.75180e-7	
0.1	0.15	0.046154	7.69205E-03	0.023077	4.75957e-7	
1	0.15	0.461538	0.0769230	0.230769		1.72694e-7
4	0.15	1.846154	0.307692	0.923077		1.44906e-6

2. Electrochemical Tests

Electrochemical methods are usually used to determine the corrosion susceptibility of SG tube material under different environments. Potentiodynamic polarization is a technique where the potential of an electrode is swept at a selected rate by application of a current through the electrolyte using a potentiostat. Potentiodynamic polarization tests can provide information on corrosion kinetics (rate of corrosion) as a function of ECP in specific environments. In order to determine the effect of chloride ion concentration on the degradation of SG tubing in SG crevices and under deposits, a series of electrochemical tests of Alloy 800 SG tubing were performed in simulated SG crevice chemistries listed in Table 2 through Table 4.

All electrochemical polarization data were performed in static autoclaves using a typical three-electrode system. The schematic of the electrochemical cell and sample mounting for high temperature electrochemical measurements is shown in Figure 1. An EG&G Model 263A/99 Potentiostat/Galvanostat with a floating/auxiliary input option is used for the potentiodynamic polarization tests in autoclave systems. The scan rate is fixed at the ASTM standard recommended rate, 0.167 mV/s [9]. All samples are tested under isothermal conditions. Internal Ag/AgCl/0.65 M KCl high temperature reference electrodes were used to make high temperature electrochemical measurements. Electrochemical measurements at 40°C are performed in a three-electrode system shown in Figure 2. An oil bath is used to maintain the test temperature. A saturated calomel electrode (SCE) is used as the reference electrode. A platinum foil is used as a counter electrode. To minimize the solution IR drop, the Luggin capillary of the reference electrode is placed close to the sample surface (≤ 1 mm). For this work, all potentials were converted to the standard hydrogen electrode scale (SHE) [10], [11].

The samples for electrochemical tests were 10 mm long segments cut from SG tubing. The external surface was finished with 600 grit silicon carbide paper and ultrasonically cleaned first with acetone and then with ethanol before the tests.

3. Experimental Results

The experiments were performed at three temperatures, representing SG layup, startup, and full power operation. Electrochemical polarization tests suggest that Alloy 800 is susceptible to pitting corrosion in the simulated neutral crevice chemistry and the pitting potential is a function of chloride concentration.

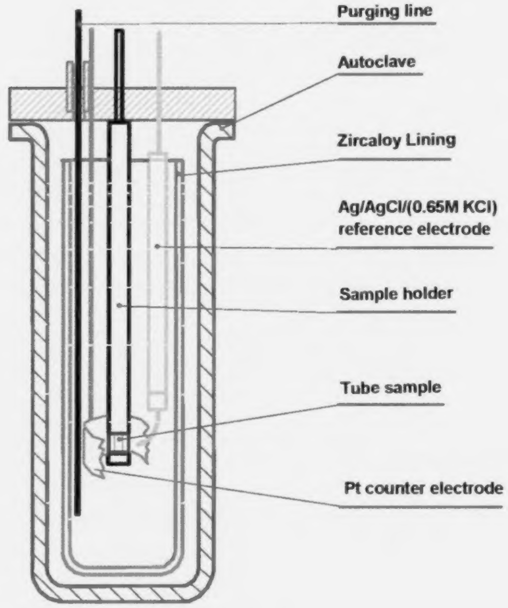

FIGURE 1
A three-electrode system for electrochemical measurements in a static autoclave.

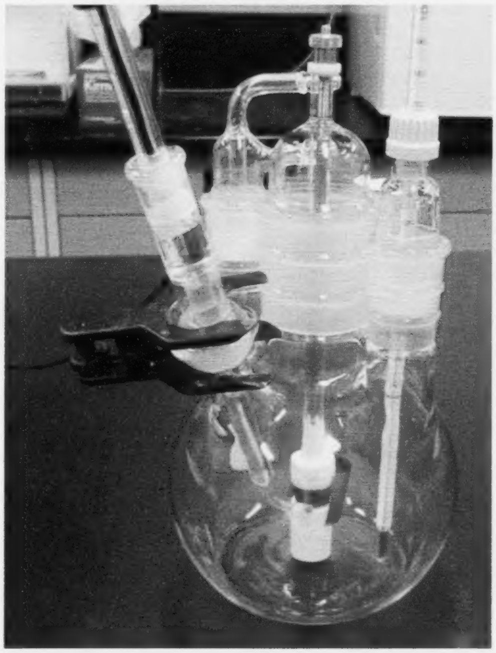

FIGURE 1
A glass cell assembly used for cyclic potentiodynamic polarization measurements at 40°C.

3.1 Effect of Different Chloride Concentrations on Alloy 800 SG Tube Degradation at 300°C

The cyclic polarization curves of Alloy 800 SG tubing obtained under neutral crevice chemistry conditions at 300°C with various chloride concentrations were superimposed in Figure 3. It is clearly shown that the pitting potential of Alloy 800 is significantly affected by the chloride concentration in the crevice chemistry. Alloy 800 is free of pitting in neutral crevice chemistry with a chloride concentration ≤ 0.01 mol/kg. The existence or absence of a pitting potential can be identified from the polarization curves. For the polarization curves in solutions containing chloride at concentrations ≤ 0.01 mol/kg, the current density increased linearly after the potential was raised above 390 mV, and it decreased following the same slope during the back scan. The current density increase for potentials above a potential of 390mV was the result of oxygen evolution. The specimens did not pit and the surface area of the specimens remained the same. Therefore, the forward scan and the back scan almost overlapped. For the rest of the polarization curves shown in Figure 3, for solutions with higher chloride ion concentrations, there was a sudden increase in the anodic current density resulting from pitting corrosion. The pitting degradation was not reversible and the anodic current density remained high during the back scan until the pits stopped growing at a specific lower potential. The cathodic branches of the polarization curves should be the same if the high temperature pH is the same. However, there were some obvious discrepancies in very dilute chloride solutions and very concentrated chloride solutions indicating the pH calculation provided by the stream analyzer requires further correction under extreme diluted and concentrated solutions.

Replicated tests were performed under each test condition. The pitting potential values obtained at 300°C from different tests performed in solutions with various chloride concentrations are listed in Table 5.

TABLE 5
Pitting potential of Alloy 800 SG tubing in neutral SG crevice at 300°C.

Cl⁻ (m)	Data 1	Data 2	Data 3	Data 4	Data 5	Average	STDEV
0.01	450 mV*	390 mV*	455 mV*	-	-	231.7 mV*	36.2 mV*
0.1	168 mV	233 mV	264 mV	-	-	221.7 mV	49.0 mV
0.65	-162 mV	-155 mV	-178 mV	-181 mV	-167 mV	-168.6 mV	10.9 Mv
1.0	-233 mV	-244 mV	-258 mV	-	-	-245.0 mV	12.5 Mv
4.0	-270 mV	-283 mV	-357 mV	-260 mV	-	-292.5 mV	44.0 mV

* Free of pitting corrosion

The pitting potential of Alloy 800 under secondary side crevice chemistry conditions at 300°C as a function of chloride solution is shown in Figure 4.

The pitting potential of Alloy 800 SG tubing under secondary SG crevice conditions at 300°C can be approximately fitted by the following empirical equations:

$$\text{Epit} = (451 - 1966\,[\text{Cl}^-])\ \text{mV} \qquad 0.01\ \text{mol/kg} > [\text{Cl}^-] \leq 0.20\ \text{mol/kg} \qquad (1)$$

$$\text{Epit} = (-288 + 56.3/[\text{Cl}^-] - 0.49/[\text{Cl}^-]^2)\text{mV}\ [\text{Cl}^-] > 0.20\ \text{mol/kg} \qquad (2)$$

3.2 Effect of Different Chloride Concentrations on Alloy 800 SG Tube Degradation at 150°C

The cyclic polarization curve of Alloy 800 SG tubing obtained

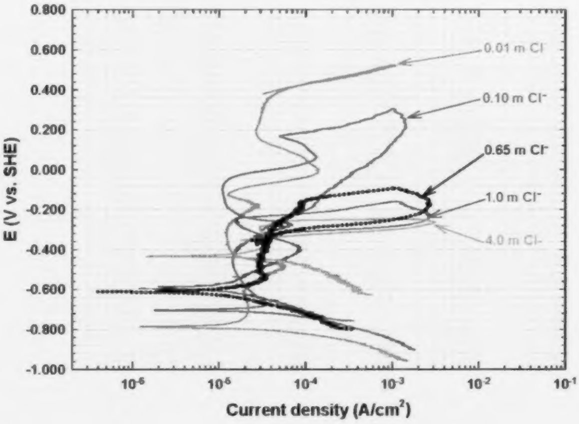

FIGURE 3
Cyclic polarization curves of Alloy 800 obtained at 300°C under neutral SG crevice chemistry conditions with different chloride concentrations.

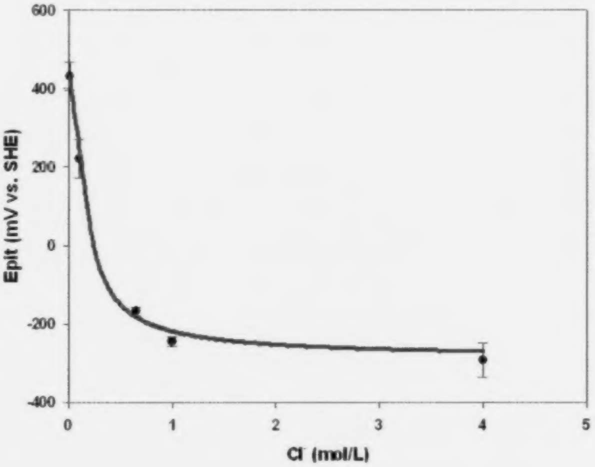

FIGURE 4
Pitting potential of Alloy 800 SG tubing material at 300°C under neutral SG crevice chemistry conditions as a function of chloride concentration.

under neutral crevice chemistry conditions at 150°C for various chloride concentrations were superimposed and shown in Figure 5. As observed at 300°C, the pitting potential of Alloy 800 is also significantly affected by the chloride concentration in the crevice chemistry at 150°C. It is seen that Alloy 800 is susceptible to pitting corrosion at 150°C even if the chloride ion concentration is as low as 0.01 mol/kg.

Replicated tests were performed under each test condition. The pitting potential values obtained at 150°C from different tests performed in solutions with various chloride concentrations are listed in Table 6.

The pitting potential of Alloy 800 under secondary side crevice chemistry conditions at 150°C as a function of chloride solution is shown in Figure 6. The pitting potential of Alloy 800 SG tubing under secondary side SG crevice conditions at 150°C can be approximately fitted by the following empirical equations:

$$E_{pit} = (1244 - 7544\,[Cl^-])\ \mathrm{mV} \qquad 0.01\ \mathrm{mol/kg} \geq [Cl^-] \leq 0.10\ \mathrm{mol/kg} \tag{3}$$

$$E_{pit} = (-193.6 + 166.1/[Cl^-] - 9.68/[Cl^-]^2)\mathrm{mV}\ [Cl^-] > 0.10\ \mathrm{mol/kg} \tag{4}$$

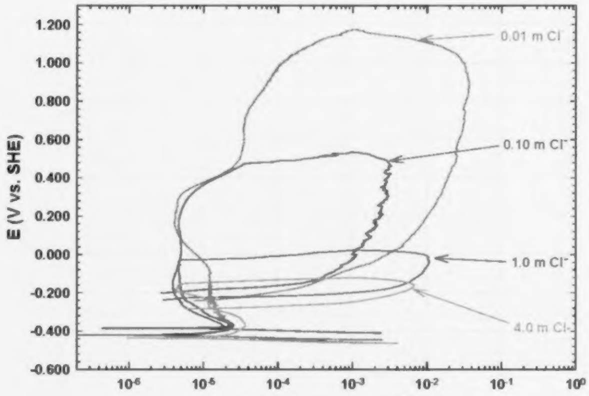

FIGURE 5

Cyclic polarization curves of Alloy 800 obtained at 150°C under neutral SG crevice chemistry conditions with different chloride concentrations.

TABLE 6

Pitting potential of Alloy 800 SG tubing in neutral SG crevice at 150°C.

Cl (m)	Data 1	Data 2	Data 3	Data 4	Data 5	Average	STDEV
0.01	1171 mV	1172 mV	1163 mV	-	-	1168.7 mV	4.9 mV
0.1	472 mV	534 mV	493 mV	-	-	499.7 mV	31.5 mV
0.65	54 mV	72 mV	8 mV	38 mV	58 mV	46.0 mV	24.5 Mv
1.0	-72 mV	-43 mV	-30 mV	-	-	-48.3 mV	21.5 Mv
4.0	-162 mV	-132 mV	-151 mV	-	-	-148.3 mV	45.2 mV

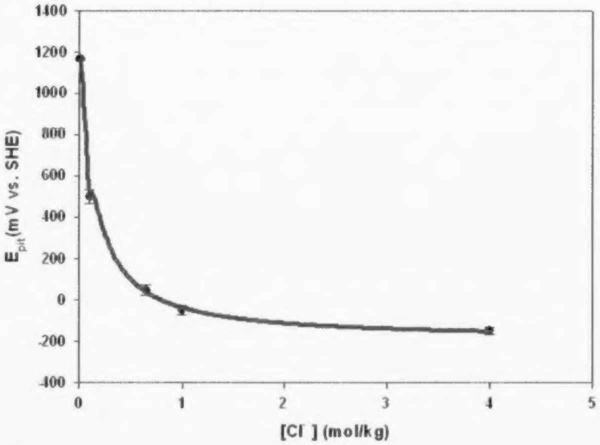

FIGURE 6

Pitting potential of Alloy 800 SG tubing material at 150°C under neutral SG crevice chemistry conditions as a function of chloride concentration.

3.3. Effect of Different Chloride Concentrations on Alloy 800 SG Tube Degradation at 40°C

The cyclic polarization curves of Alloy 800 SG tubing obtained under neutral crevice chemistry conditions at 40°C for various chloride concentrations were superimposed in Figure 7. The pitting potential of Alloy 800 is decreasing as the chloride concentration in the crevice chemistry increases. Alloy 800 is immune to pitting potential when chloride concentrations are equal to or lower than 0.01 mol/kg. A cathodic loop or shoulders could be seen in the polarization curves shown in Figure 7 indicating the existence of some residual dissolved oxygen. This would not affect the pitting potential measurements.

The pitting potential values obtained at 40°C from replicated tests performed in solutions with various chloride concentrations are listed in Table 7.

The pitting potential of Alloy 800 under secondary side

TABLE 7

Pitting Potential of Alloy 800 SG Tubing in Neutral SG Crevice at 40°C

Cl (m)	Data 1	Data 2	Data 3	Data 4	Data 5	Average	STDEV
0.01	*	*	*	-	-	*	*
0.1	1129 mV	1058 mV	1131 mV	-	-	1106.0 mV	41.6 mV
0.65	411 mV	346 mV	348 mV	425 mV	374 mV	380.8 mV	36.1 mV
1.0	371 mV	316 mV	309 mV	-	-	332.0 mV	34.0 mV
4.0	199 mV	203 mV	238 mV	-	-	213.3 mV	21.5 mV

* Free of pitting corrosion

crevice chemistry conditions at 40°C as a function of chloride solution is shown in Figure 8 and can be approximately fitted by the following empirical equation:

$$E_{pit} = (183 + 141/[Cl^-] - 4.87/[Cl^-]^2)\,\mathrm{mV} \quad [Cl^-] > 0.10\ \mathrm{mol/kg} \tag{5}$$

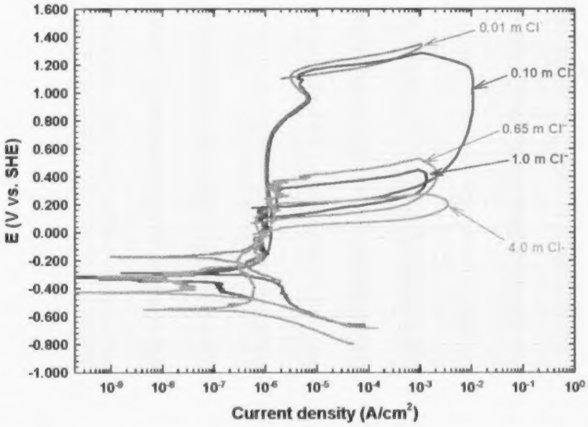

FIGURE 7
Cyclic polarization curves of Alloy 800 obtained at 40°C under neutral SG crevice chemistry conditions with different chloride concentrations.

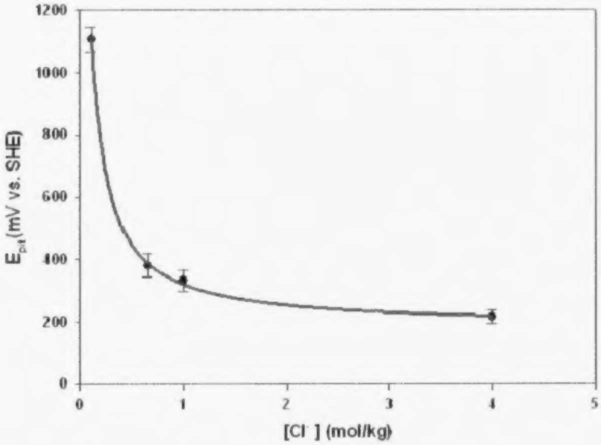

FIGURE 8
Pitting potential of Alloy 800 SG tubing material at 40°C under neutral SG crevice chemistry conditions as a function of chloride concentration.

The pitting potential of Alloy 800 SG tubing at three different temperatures under neutral SG crevice chemistry conditions as a function of chloride concentration in log scale is shown in Figure 9. It is seen that the pitting potential of Alloy 800 at 150°C under neutral crevice chemistry conditions follows a linear relationship with the log value of chloride ion concentration when the chloride ion concentration is less than 1 mol/kg. At 40°C and 300°C the linear relation between E_{pit} and log C_{Cl-} can also be seen in the range of 0.1 m ≤ C_{Cl-} ≥1 m. It is possible that the E_{pit} and Log $[Cl^-]$ may follow a linear relation. Attempts were made to check the linear relation between E_{pit} and log $[Cl^-]$ but failed because of an unreasonable high calculated activity coefficient value at high chloride ion concentrations based on the data obtained from the commercial OLI software Stream Analyzer [8] This observation also suggests that the calculated pH value of solutions containing very high chloride concentrations using the OLI software Stream Analyzer may have certain deviations.

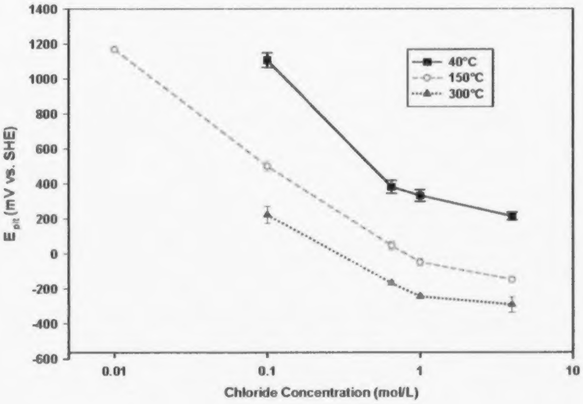

FIGURE 9
Pitting potential of Alloy 800 SG tubing material at 40°C, 150°C and 300°C under neutral SG crevice chemistry conditions as a function of chloride concentration.

3.4 Pitting Potential of Alloy 800 under Neutral Crevice Chemistry Conditions as a Function of Temperature

The pitting potential of Alloy 800 decreases with temperature under the same crevice chemistry conditions. The pitting potential of Alloy 800 as a function of temperature could be fitted with equations shown in Figure 10. In the figure, the pitting potential of Alloy 800 under neutral SG crevice chemistries with different chloride ion concentrations as a function of temperature in Kelvin scale was plotted against K^{-1}. It appears that the pitting potential in a crevice solution with fixed chloride concentration follows a linear relation with 1/K. This observation suggests that the breakdown of the passivity and the initiation of pitting corrosion by chloride ions are thermally activated.

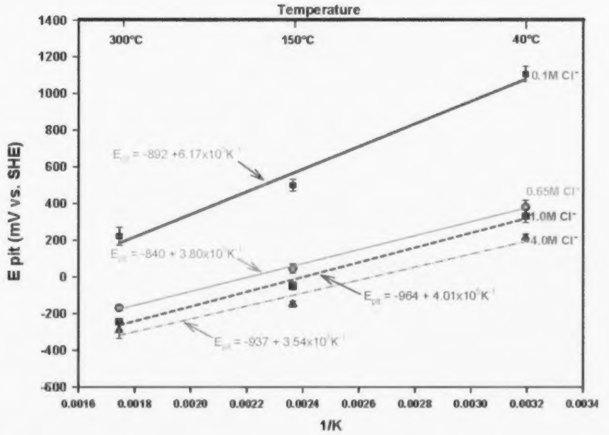

FIGURE 10
Pitting potential of Alloy 800 SG tubing material under neutral SG crevice chemistry conditions with different chloride ion concentrations as a function of 1/K.

4. Conclusions

Cyclic potentiodynamic polarization measurements were performed on Alloy 800 SG tubing materials in neutral SG crevice chemistries with different chloride concentrations at 40, 150, and 300°C, respectively. The electrochemical experimental results show that Alloy 800 is immune from pitting degradation if the chloride ion concentration in the neutral SG crevice chemistry is equal to 0.01 mol/kg or lower, except at 150°C. At 150°C, Alloy 800 is still susceptible to pitting corrosion even if the chloride ion concentration in the neutral crevice chemistry is as low as 0.01 mol/kg. The pitting potential of Alloy 800 SG tubing decreases with the increase of chloride ion concentration when the chloride concentration in the neutral crevice chemistry is higher than 0.01 mol/kg. In neutral crevice chemistries with a fixed chloride ion concentration, the pitting potential of Alloy 800 decreases as the temperature increases.

4.1. Empirical Equations of Pitting Potential of Alloy 800 SG tubing as a Function of Chloride Ion Concentration

The pitting potential of Alloy 800 in the neutral SG crevice chemistry as a function of chloride ion concentration could be fitted to empirical equations through a linear regression followed by an inverse second order regression. These empirical equations can be used to determine the pitting potential of Alloy 800 in neutral crevice chemistry with known chloride ion concentration.

The pitting potential of Alloy 800 SG tubing under secondary side SG neutral crevice chemistry conditions at 300°C can be fitted by the following empirical equations:

$$E_{pit} = (451 - 1966\,[Cl^-])\ mV \quad 0.01\ mol/kg > [Cl^-] \leq 0.20\ mol/kg \qquad (6)$$

$$E_{pit} = (-288 + 56.3/[Cl^-] - 0.49/[Cl^-]^2)mV\ [Cl^-] > 0.20\ mol/kg \qquad (7)$$

The pitting potential of Alloy 800 SG tubing under secondary side SG neutral crevice chemistry conditions at 150°C can be fitted by the following empirical equations:

$$E_{pit} = (1244 - 7544\,[Cl^-])\ mV \quad 0.01\ mol/kg \geq [Cl^-] \leq 0.10\ mol/kg \qquad (8)$$

$$E_{pit} = (-193.6 + 166.1/[Cl^-] - 9.68/[Cl^-]^2)\ mV\ [Cl^-] > 0.10\ mol/kg \qquad (9)$$

The pitting potential of Alloy 800 SG tubing under secondary side SG neutral crevice chemistry conditions at 40°C can be fitted by the following empirical equations:

$$E_{pit} = (183 + 141/[Cl^-] - 4.87/[Cl^-]^2)mV\ [Cl^-] > 0.10\ mol/kg \qquad (10)$$

4.2. Empirical Equations of Pitting Potential of Alloy 800 SG tubing as a Function of Temperature

The pitting potential of Alloy 800 in a neutral SG crevice chemistry with a fixed chloride ion concentration as a function of temperature could be fitted with quadratic equations shown in Equations 11-14:

$$E_{pit} = (-892 + 6.17 \times 10^5 K^{-1})\ mV \quad (0.1\ M\ Cl^-) \qquad (11)$$

$$E_{pit} = (-840 + 3.80 \times 10^5 K^{-1})\ mV \quad (0.65\ M\ Cl^-) \qquad (12)$$

$$E_{pit} = (-964 + 4.01 \times 10^5 K^{-1})\ mV \quad (1.0\ MCl^-) \qquad (13)$$

$$E_{pit} = (-937 + 3.54 \times 10^5 K^{-1})\ mV \quad (4.0\ MCl^-) \qquad (14)$$

4.3. Limitations of the Empirical Equations

The empirical equations are applicable to Alloy 800 SG tubing under nuclear SG secondary side crevice or under deposit conditions for stations using all volatile treatment (AVT) for SG feed water treatment. The experimental results had good reproducibility and the standard deviations of the data were less than 50 mV. It is known that certain SG impurities such as copper, magnesium [12, 13] and thiosulphate [14] will have significant impact on the pitting potential of SG tubing. Therefore, the empirical equations may not be valid if the SG systems contain the above mentioned impurities.

Acknowledgements

This work is funded by AECL. The experimental work was performed by M. Dupuis. The author would like to thank P. Angell and R.L. Tapping for the management support. M. Huang is acknowledged for his help on determining the crevice chemistries for testing and S. Klimas for reviewing this paper and many helpful suggestions.

REFERENCES

[1] Y.C. Lu, February 2002, "Localized Corrosion and its Prevention for Heat Exchanger Tubing under Steam Generator Crevice Conditions", Part I. Mechanisms and Electrochemical Approaches for Establishing Safe Potential/pH Zones, COG Report, COG 01 051

[2] Y. Lu, November 2006, "Minimize Corrosion Degradation of Steam Generator Tube Materials Updated ECP/pH Zone for Alloy 800 SG Tubing ", Proceedings of the 5th CNS International Steam Generator Conference, Toronto

[3] S. Liu and Y.C. Lu,"Evaluation of SCC Susceptibility of Alloy 800 under CANDU Steam Generator Secondary –Side Conditions", CW-127320-CONF-001, Proc. of the 5th CNS International Steam Generator Conference, Nov. 26-29 2006, Toronto. (2006)

[4] M. Mirzai, C. Maruska, S. Pagan, O. Lepik, G. Ogundele, M. Wright, and G. Kharshafdjian, 1997, "Stress Corrosion Cracking/Corrosion Fatigue/Fatigue in Alloy 600", Proceedings of the 8th International Symposium on Environmental Degradation of Materials in Nuclear Power Systems Water Reactors, Vol. 1, pp. 11-18, American Nuclear Society Inc., La Grange Park, IL, USA

[5] G.R. Burton and C.W. Turner, 2007, "Rationale for Crevice Chemistry Test Solution Compositions", COG 06 4057

[6] L. Chi, G. Goszczynski and Y.C. Lu,"Test Plan for Investigating the Low Temperature Degradation of Steam Generator Tubing Materials in the Environments Containing Intermediate Oxidation State of Sulphur", 153-33112-COG-009, COG OP-09-4076 (2009)

[7] P.V. Balakrishnan, November 1977, "Effect of Condenser Water in leaking on Steam Generator Chemistry", Paper Number IWC 77 12, Proceedings of the 38th Annual Meeting of International Water Conference, Pittsburgh, Pennsylvania, USA

[8] A. Anderko, P. Wang, and M. Rafal, 2002, "Electrolyte Solutions: From Thermodynamic and Transport Property Models to the Simulation of Industrial Processes", Fluid Phase Equilibria, 194-197, pp. 123-142

[9] ASTM Designation: "Standard Reference Test Method for Making Potentiostatic and Potentiodynamic Anodic Polarization Measurements", G5 94 (Reapproved 2011)

[10] R.S. Greeley, W.T. Smith, Jr., R.W. Stoughton, and M.H. Lietzke, 1960, "Electromotive Force Studies in Aqueous Solutions at Elevated Temperatures. I. The Standard Potential of the Silver Silver Chloride Electrode", Journal of Physical Chemistry, 64, pp. 652-657

[11] F. King, M.G. Bailey, C.F. Clarke, B.M. Ikeda, C.D. Litke, and S.R. Ryan, 1989, "A High-Temperature, High-Pressure, Silver Silver Chloride Reference Electrode: A User's Guide", Atomic Energy of Canada Ltd. Report, AECL 9890

[12] Y.C. Lu, D. Burns and M.G. Dupuis, 2009, "The Interactive Effects between Steam Generator Impurities on CANDU Steam Generator Tube Corrosion A Final Report", 153 33112 COG 007 COG 09 4058

[13] Y. C. Lu, 2010, "Effect of Hazardous Impurities on Steam Generator Tube", ICONE18-30120, Proceedings of the 18th International Conference on Nuclear Engineering (ICONE18), May 17-21, 2010, Xi'an, China.

[14] L. Chi and Y. C. Lu, "Electrochemical Studies of Steam Generator Tube Degradation in The Presence of Thiosulphate", 153-33112-PLA-003, Proc. of the 15th International Conference on Environmental Degradation of Materials in Nuclear Power Systems-Water Reactors, August 7-11, 2011 Colorado Springs, Colorado

FULL ARTICLE

NUCLEAR DATA AND THE EFFECT OF GADOLINIUM IN THE MODERATOR

J.C. Chow[A]*, F.P. Adams[A], D. Roubstov[A], R.D. Singh[B] and M.B. Zeller[A]

[A] Atomic Energy of Canada Limited, Chalk River Laboratories, Chalk River, Ontario, Canada, K0J 1J0
[B] Candu Energy Inc., 2280 Speakman Drive, Mississauga, Ontario, Canada, L5K 1B1

Article Info
Keywords: gadolinium cross-section, moderator poison, nuclear data, ZED-2
Article history: Received 24 April 2012, Accepted 9 June 2012, Available online 30 June 2012.
*Corresponding Author: (613) 584-3311 ext. 44437, chowj@aecl.ca

ABSTRACT

Recent cross-section measurements on gadolinium have raised concerns over the accuracy of moderator poison reactivity coefficient calculations. Measurements have been made at the ZED-2 (Zero Energy Deuterium) critical facility, Chalk River Laboratories, AECL, to study the reactivity effect of gadolinium in the moderator. Since the neutron capture cross-section of boron is well known, measurements were also made with boron to provide calibration data for measurements with gadolinium. The measurements have been used to quantify the bias of the reactivity effect in full-core simulations of ZED-2 using MCNP, a neutron transport code used extensively for simulations of nuclear systems, along with the ENDF/B-VII.0 cross-section data. The results showed a bias of −0.41 ± 0.07 mk/ppm, or −2.1% ± 0.3%, given a reactivity worth of −20.1 mk/ppm for gadolinium. Additional simulations also show that the gadolinium neutron capture cross-section has been over-corrected, relative to previous evaluations, in a beta version of ENDF/B VII.1, which incorporates the Leinweber data.

1. Introduction

With the highest neutron absorption cross-section in the thermal region of all naturally occurring elements, gadolinium is used in CANDU®[1] reactors to suppress excess reactivity or to shut down the reactor in case of emergency. Recent measurements on total neutron capture cross-section of gadolinium [1] have raised concerns over the accuracy of moderator poison reactivity coefficient calculations. It was reported [2] that the use of the Leinweber data helps to improve the prediction of total fission reaction rate as well as the ratio of ^{238}U capture to total fission reaction rate in gadolinium-poisoned fuel (UO_2-Gd_2O_3) in some BWR configurations. However, in the recent release of ENDF/B-VII.1 evaluated nuclear data library [3], the Leinweber data were not taken into account. In order to address this issue, measurements have recently been made at the ZED-2 (Zero Energy Deuterium) critical facility [4], Chalk River Laboratories, AECL, to study the reactivity effect of up to 1.5 ppm of gadolinium in the moderator. ZED-2 is a heavy-water-moderated reactor that operates predominantly in the thermal neutron region. Since the neutron capture cross-section of boron in the thermal region is known to within ±0.1% [5,6], measurements were also made with up to 6 ppm of boron to provide calibration data for measurements with gadolinium.

The measurements have been used to quantify the reactivity effect of gadolinium in the moderator in full-core simulations of ZED-2 using MCNP5 [7], a neutron transport code used extensively for simulations of nuclear systems. The objective of the analysis is to quantify the bias and uncertainty in the effective neutron multiplication factor, k_{eff}, in full-core MCNP simulations of ZED-2 as a function of gadolinium concentration. The MCNP models were executed on a computer cluster recently installed at the Chalk River Laboratories under the Linux platform. The targeted nuclear data library for the majority of the analysis is E70CRL [8], developed at AECL based on ENDF/B VII.0 [9]. However, results based on gadolinium nuclear data from a beta version of ENDF/B VII.1, which incorporated the results from Leinweber, as well as the release version of ENDF/B VII.1 [3] will also be presented for comparison.

2. The ZED-2 Core Configuration

The measurements were performed in the ZED-2 critical facility, which is categorized as a tank-type research reactor (see Figure 1). The calandria tank is an aluminum cylinder of ~3.4 m both in diameter and height, surrounded by a graphite reflector radially and at the bottom. High purity (>98 wt%) heavy water is used as moderator. Fuel channels can be installed from the top to form the reactor core. Each fuel channel is installed with five fuel bundles of ~50 cm in length. Criticality is achieved by raising the moderator level in the calandria tank. Major parameters taken for each experimental run include the critical height, temperature, and purity of the moderator, as well as the temperature of the fuel. Elaborated details about the ZED-2 facility can be found in [4].

---

[1] CANDU® is a registered trademark of Atomic Energy of Canada Limited (AECL).

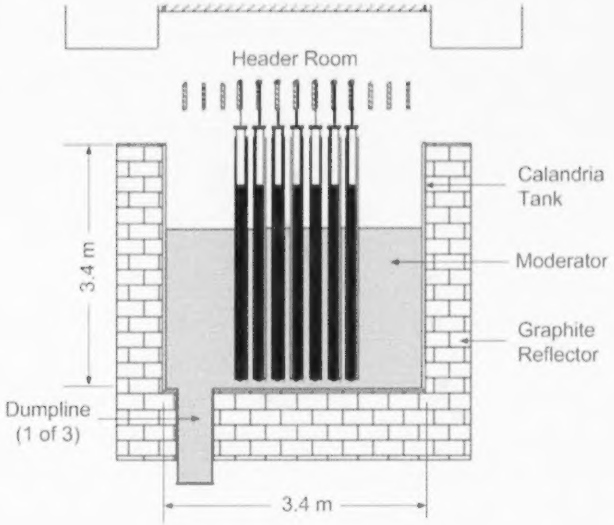

FIGURE 1
ZED-2 Reactor Layout.

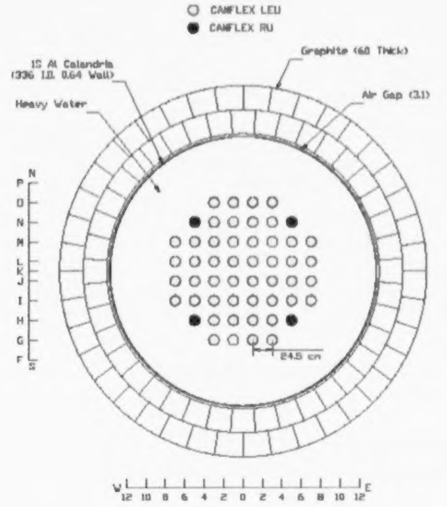

FIGURE 2
ZED-2 core configuration for present measurements.

The configuration of the reactor core for the present measurements is shown in Figure 2. The core consists of 52 fuel channels each of which was installed with five Low Enriched Uranium (LEU) or Recovered Uranium (RU) fuel bundles in a 24.5 cm pitch square lattice. The channels are often filled with water coolant. However, fuel channels for the present measurements were filled with air to avoid potential complications in the analyses.

In order to maintain a consistent setup for the measurements, the core configuration was left unaltered throughout the experiment except for the controlled addition of poison in the moderator. A reference measurement was taken at the beginning of each series before the addition of poison. In the main series of measurements, gadolinium was added to the moderator from nominal values of 0.5 to 1.5 ppm in increments of 0.5 ppm, and in the reference series with boron from nominal values of 2.0 to 6.0 ppm in increments of 2 ppm.

3. Analysis with MCNP5

The measurements have been analyzed with MCNP5. The targeted nuclear data library for the analysis is E70CRL [8], developed at AECL based on ENDF/B VII.0 [9]. The core parameters pertaining to modeling the experimental runs for the Boron and Gadolinium series are listed in Table 1 and Table 2, respectively, which were subsequently used, along with geometric and material data available elsewhere, e.g., [4], as input for development of MCNP models.

The data from the Boron series was first used to calibrate the system with respective to the poison concentration. Since the neutron capture cross-section of boron in the thermal region is known to within ±0.1% [6], which is equivalent to an uncertainty in computed k_{eff} of ±0.03 mk[2], the functional dependence of k_{eff} to boron concentration is expected to be negligibly small, on condition that the boron concentration is properly modeled. In the present measurements, the nominal boron concentrations[3] would be biased due to uncertainty in the ZED-2 moderator inventory, which is known to only ±2%. However, a calibration factor can be obtained by adjusting the nominal boron concentration value until the k_{eff} value matches that of the model without poison. Hence, the analysis started with developing a reference MCNP model, without poison, according to

TABLE 1
Boron Series – Core Parameters for MCNP Models

Case #	Boron Conc.* [ppm]	Moderator† Purity [wt% D_2O]	Channel Temperature [°C]	Moderator Temperature [°C]	Critical¶ Height [cm]
B1	0.0	98.743	21.50	21.55	131.650
B2	2.0	98.742	21.30	22.05	139.420
B3	4.0	98.740	21.63	22.19	148.248
B4	6.0	98.738	22.15	22.53	158.442

* These are nominal values based on the mass of the poison added relative to the known inventory of moderator in the system.
† Standard deviation in moderator purity = 0.005 wt% D2O.
¶ Standard deviation in critically height = 0.2 cm.

---

[2] This value was obtained by a sensitivity study of a model with 6 ppm of boron in the moderator.
[3] The nominal concentration was determined as the ratio of the mass of poison added to the moderator to the recorded moderator inventory.

TABLE 2
Gadolinium Series – Core Parameters for MCNP Models

Case #	Gd Conc.* [ppm]	Moderator† Purity [wt% D_2O]	Channel Temperature [°C]	Moderator Temperature [°C]	Critical¶ Height [cm]
G1	0.0	98.748	21.80	21.70	131.585
G2	0.5	98.748	21.75	21.79	138.248
G3	1.0	98.744	21.65	21.89	145.632
G4	1.5	98.739	21.45	22.51	153.926

* See footnotes in Table 1.

the configuration described in Section 2, followed by a case with the maximum nominal value of 6.0 ppm of boron in the moderator. Then, the boron content was adjusted until the k_{eff} value matched that of the case without poison to within ±0.1 mk, the statistical uncertainty inherent in the MCNP-computed k_{eff} values obtained with 100 million neutron histories. The adjustment in boron concentration to achieve the above condition was found to be −1.2%. The same adjustment was then applied to the other cases with nominal boron concentrations of 2.0 and 4.0 ppm. The resulting k_{eff} values with the adjusted concentrations are listed in Table 3 and plotted in Figure 3 as a function of boron concentration. The relatively small slope (0.003 mk/ppm) in the line in Figure 3 indicates that the functional dependence of the k_{eff} values on the boron concentration can be minimized, within uncertainty, with proper adjustments to the nominal values. Thus, the nominal boron concentrations are judged to have been overestimated due to uncertainty in the moderator inventory, and a correction factor of −1.2%, henceforth referred to as the boron calibration factor, should be applied to the nominal boron concentration values.

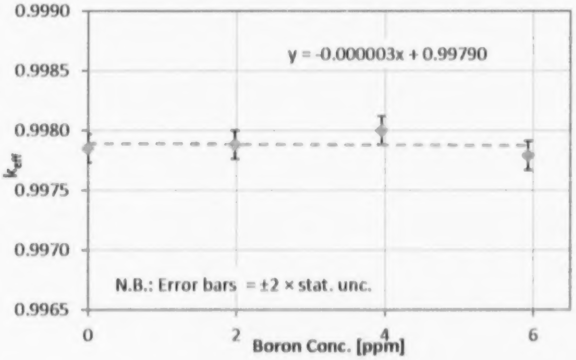

FIGURE 3
Boron series – MCNP k_{eff} values with adjusted Boron concentration.

Since the Boron and Gadolinium series were performed consecutively with the same moderator inventory and the same protocols were used for measuring and adding the poisons to the moderator, the boron calibration factor can also be applied to the Gadolinium series of measurements. The results of k_{eff} values obtained by applying the boron calibration factor, i.e., multiplying the nominal gadolinium concentration values by the factor 0.988, are shown in Table 4. A discussion on the results follows the assessment of uncertainties in Section IV below.

TABLE 3
Boron Series – MCNP k_{eff} Values with Adjusted Concentrations

Case	Adjusted Boron Conc. [ppm]	k_{eff}
B1	0.000	0.99785
B2	1.976	0.99788
B3	3.952	0.99800
B4	5.928	0.99779

TABLE 4
Gadolinium Series – MCNP k_{eff} Values with Boron-Calibrated Concentrations

Case	Boron-Calibrated Gd Conc [ppm]	k_{eff}
G1	0.000	0.99788
G2	0.494	0.99766
G3	0.988	0.99759
G4	1.482	0.99713

4. Assessment of Uncertainties

The total uncertainty in k_{eff} (σ_{keff}) obtained in an MCNP simulation of a ZED-2 full-core benchmark model, using fuel channels[4] similar to those in the present experiment, was assessed by Atfield [4] to be about ±3 mk, consistent with the biases in k_{eff} values observed in Table 3 and Table 4. In the following assessment, only terms that contribute to the uncertainty in k_{eff} bias due to the presence of gadolinium in the moderator are included.

The uncertainty in the computation of keff bias relevant to the present analysis is determined as follows:

$$\sigma_{k_{eff}} = \sqrt{\sigma^2_{\mathrm{stat}} + \sigma^2_{\mathrm{expt}} + \sigma^2_{\mathrm{cal}} + \sigma^2_{\mathrm{Gd}}} \qquad (1)$$

---

[4] The uncertainties in the dimensions of the fuel channels were found in reference [4] to be the largest contributors to the keff uncertainty.

where σ_{stat} is the statistical uncertainty intrinsic to the MCNP simulation, σ_{expt} is the experimental uncertainty, σ_{cal} is due to using the boron calibration factor to calibrate the gadolinium concentration, and σ_{Gd} is due to uncertainties in the gadolinium neutron capture cross-section.

The statistical uncertainty arises from the Monte Carlo nature of simulations using MCNP. All the MCNP models have been executed with 100 million active neutron histories yielding a statistical uncertainty, σ_{stat}, of ±0.06 mk.

Assuming no correlation among the contributing terms, the experimental uncertainty, σ_{expt}, can be expressed as:

$$\sigma_{expt} = \sqrt{\sigma^2{}_{hc} + \sigma^2{}_{pur}} \tag{2}$$

where σ_{hc} and σ_{pur} are uncertainties due to the critical height and purity of the moderator. Based on a sensitivity analysis by direct perturbation calculations similar to those performed in reference [4], σ_{hc} and σ_{pur} have been assessed as ±0.036 mk and ±0.065 mk (see footnote in Table 1), respectively, yielding an experimental uncertainty, σ_{expt}, of ±0.07 mk.

The uncertainty in the boron calibration factor is assessed as contributed by two terms; one is due to the statistical uncertainty[6] of ±0.06 mk intrinsic to the MCNP simulation; the other is due to uncertainty in the total boron neutron capture cross-section of ±0.1% in the thermal region [5,6], which is equivalent to an uncertainty in k_{eff} of ±0.03 mk for a model with 6 ppm of boron (with a total reactivity worth of 33.6 mk, obtained by adding 6 ppm of boron to the reference ZED-2 model without boron and comparing the k_{eff} values). Adding the two terms in quadrature yields an uncertainty of ±0.07 mk, or ±0.2% of the total boron reactivity worth of 33.6 mk. Therefore, the boron calibration factor is assessed as −1.2% ± 0.2%. By adding one ppm of gadolinium to the base model without gadolinium and comparing the keff values, the reactivity worth of gadolinium in the moderator in ZED-2 has been determined as −20.1 mk/ppm. Therefore, σ_{cal}, the uncertainty in k_{eff} due to the use of the boron calibration factor, is assessed as ±0.04 mk/ppm (= 20.1 mk/ppm × 0.2%).

The uncertainty attributable to the gadolinium neutron capture cross-section has been investigated from various sources. Figure 4 shows the uncertainties around the thermal region for ^{157}Gd from three sources. Note that only ^{157}Gd, which contributes ~80% of the total neutron capture cross-section, is included in this assessment. While Mughabghab [10] assigns a single value of ±0.32% at 0.0253 eV, ORNL [11] assigns values ranging from 0.3% to ~3%, and NNDC [12] assigns a value of ±4% for the entire thermal region. For the purpose of the present analysis, a value of ±2% is adopted. A sensitivity analysis of the three models containing gadolinium in the moderator has shown that an uncertainty of ±2% in the gadolinium neutron capture cross section is equivalent to a k_{eff} uncertainty, σ_{Gd}, of 0.50 mk/ppm. All the uncertainty components contained in Equation (1) and obtained according to the above assessments are listed in Table 5. It should be reiterated that only terms that contribute to the uncertainty in k_{eff} bias due to the presence of gadolinium in the moderator are included in the above assessments.

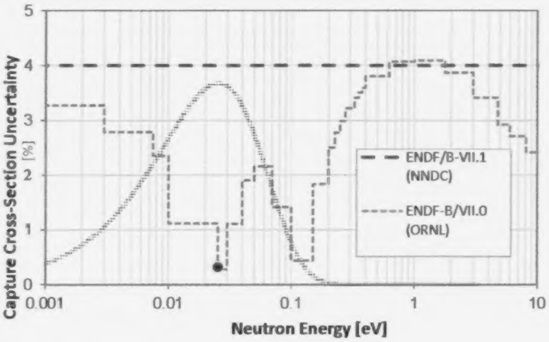

FIGURE 4
^{157}Gd Neutron Capture Cross-Section Uncertainty

TABLE 5
Sources of k_{eff} Uncertainties

Sources	Symbol	Contrib. to σ_{keff}
MCNP Statistical Uncertainty	σ_{stat}	±0.06 mk
Experimental (moderator height/purity)	σ_{expt}	±0.07 mk
Boron calibration	σ_{cal}	±0.04 mk/ppm
^{157}Gd Neutron Capture Cross-section	σ_{Gd}	±0.5 mk/ppm

5. Discussion of Results and Conclusions

The results of k_{eff} values obtained with boron-calibrated gadolinium concentrations are listed in Table 4. Note that the bias in k_{eff} values of ~−2 mk, attributable mainly to uncertainties in the dimensions of the fuel channel and fuel enrichment [4], would not affect the present results, which are based on relative measurements/calculations. A plot of k_{eff} values verses gadolinium concentrations is shown in Figure 5, in which the uncertainties are assigned according to Table 5. According to a linear regression analysis of the data points weighted with their respective variances, the bias in k_{eff} value in MCNP simulations of the ZED-2 full-core with gadolinium in the moderator is assessed as −0.41 ± 0.07 mk/ppm, or −2.1% ± 0.3%, for the target nuclear data library ENDF/B-VII.0, given a reactivity worth of −20.1 mk/ppm for gadolinium in ZED-2.

---

[6] Note that this statistical uncertainty arises from simulation of a model containing boron while σstat in Equation (1) arises from a model containing gadolinium.

While the above results were obtained with the E70CRL nuclear data library [8] based on ENDF/B VII.0 [9], additional MCNP simulations of the same models but incorporating the ^{157}Gd cross section data from the release version, as well as a beta version, of the ENDF/B VII.1 data library have also been performed. In the beta version, the measurements from [1] were taken into account, in which the scattering width (Γn) of the first resonance at 0.0314 eV was decreased by 7% from previous evaluations. The results of the additional simulations with ^{157}Gd cross section data from the ENDF/B VII.1 library are plotted in Figure 6 along with the results obtained with ENDF/B VII.0 [9]. While the results based on the release version of ENDF/B VII.1 are identical to those based on ENDF/B VII.0 within statistical uncertainties, those from the beta version of ENDF/B VII.1, which incorporates the data from Leinweber [1], deviate significantly from those based on the ENDF/B VII.0 data. In essence, Figure 6 shows that the gadolinium neutron capture cross section is overestimated in ENDF/B VII.0 [9] data and underestimated in the beta version of ENDF/B VII.1 which incorporates the Leinweber [1] data, indicating that the decrease of 7% might have been overcompensated.

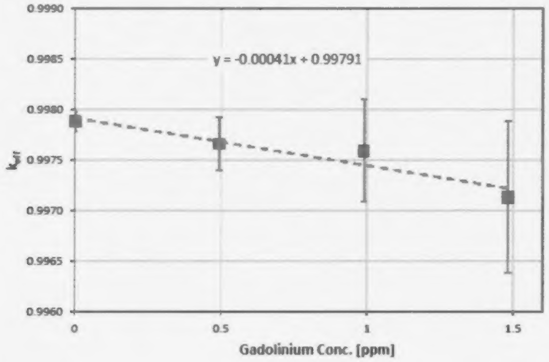

FIGURE 5
Gadolinium series –MCNP k_{eff} values with Boron-calibrated concentrations.

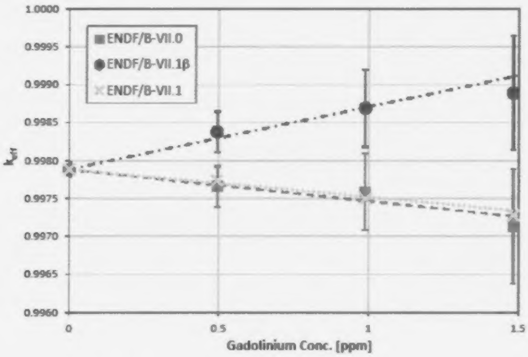

FIGURE 6
Comparison with ENDF/B-VII.1 data.

Based on the above results, it is concluded that the reactivity effect of gadolinium in the moderator can be calculated with MCNP5, along with the ENDF/B-VII.0 or ENDF/B-VII.1 nuclear data libraries, with a bias that is consistent with the nominal ±2% uncertainty of the nuclear data. The incorporation of the Leinweber data in the ENDF/B-VII.1 beta evaluation changed the sign of the apparent bias in the calculations, but the overall accuracy was not improved. The results provide confidence in the use of the ENDF/B-VII.0 or ENDF/B-VII.1 nuclear data evaluations in calculations of reactivity effect of gadolinium in the moderator.

6. Acknowledgements

We thank J. Atfield for help with the pre-experiment simulations, G. Cully, K. Thompson, and D. Grice for conducting the experiments, and L. Blomeley for compiling the experimental data which formed the basis of this work. We also thank the EC6 Group of Candu Energy Inc. for funding the experiment.

REFERENCES

[1] G. Leinweber et al., 2006, "Neutron Capture and Total Cross-Section Measurements and Resonance Parameters of Gadolinium", Nuclear Science and Engineering, 154, pp. 261-279
[2] G. Perret et al., 2009, "Impact of New Gadolinium Cross Sections on Reaction Rate Distributions in 10 × 10 BWR Assemblies", Nuclear Science and Engineering, 163, pp. 17 25
[3] M.B. Chadwick et al., 2011, "ENDF/B-VII.1 Nuclear Data for Science and Technology: Cross Sections, Covariances, Fission Product Yields and Decay Data", Nuclear Data Sheets, 112, pp. 2887-2996
[4] J. E. Atfield, March 2011, "28-Element Natural UO2 Fuel Assemblies in ZED-2 (ZED2 HWR EXP 001)", in International Handbook of Evaluated Reactor Physics Benchmark Experiments (IRPhEP), OECD – NEA/NSC/DOC (2006)
[5] International Atomic Energy Agency, Vienna, 2007, "International Evaluation of Neutron Cross-Section Standards", STI/PUB/1291
[6] A.D. Carlson et al., 2009, "International Evaluation of Neutron Cross Section Standards", Nuclear Data Sheets, 110, pp. 3215–3324
[7] X-5 Monte Carlo Team, April 2003, "MCNP - A General Monte Carlo N-Particle Transport Code, Version 5. Volume 1: Overview and Theory", LANL report LA-UR-03-1987 (Revised 10/3/2005)
[8] D. Altiparmakov, May 2010, "ENDF/B-VII.0 versus ENDF/B-VI.8 in CANDU® Calculations", Proceedings of PHYSOR 2010 – Advances in Reactor Physics to Power the Nuclear Renaissance, Pittsburgh, Pennsylvania, USA, on CD ROM, American Nuclear Society, LaGrange Park, IL, USA
[9] M.B. Chadwick et al., 2006, "ENDF/B-VII.0: Next Generation Evaluated Nuclear Data Library for Nuclear Science and Technology", Nuclear Data Sheets, 107, pp. 2931-3060
[10] S.F. Mughabghab, "Atlas of Neutron Resonances – Resonance Parameters and Thermal Cross Sections. Z=1-100", 5th Ed. Elsevier Science
[11] Oak Ridge National Laboratory, 2009, "SCALE: A Modular Code System for Performing Standardized Computer Analyses for Licensing Evaluation", ORNL/TM 2005/39, Version 6
[12] NNDC, "National Nuclear Data Center, 2011, Evaluated Nuclear Data File (ENDF) Retrieval & Plotting", http://www.nndc.bnl.gov/sigma/index.jsp, Brookhaven National Laboratory, ENDF/B-VII.1

FULL ARTICLE

MEASUREMENTS OF THE HIGH DOSE RATE PROFILES INSIDE A SHUTDOWN CANDU® REACTOR

C. Jewett[A*], J. Chow[A], D. Comeau[B], G. Jonkmans[A], B. Smith[A], B. Sur[A], D. Taylor[B], S. Yue[A]

[A] Atomic Energy of Canada Limited, Chalk River Laboratories, Chalk River, Ontario, Canada, K0J 1J0
[B] Point Lepreau Generating Station, Point Lepreau, NB, Canada, E5J 2S6

Article Info
Keywords: gamma-ray imaging; radiation measurement; CANDU® reactors; MCNP5 simulations; gamma-ray detectors

* Corresponding author: (613) 584-3311, jewettc@aecl.ca

ABSTRACT

The positions of the components of a reactor can change over time, due to radiation damage, sagging, etc. Thus, it is important to determine their positions. To satisfy this requirement of the staff at the Point Lepreau Generating Station, a method to determine the positions of reactor components has been developed and demonstrated. This method combines the use of dose rate measurements and Monte Carlo simulations. It first involves measuring the high γ-ray dose rates as a function of position within a reactor. Then it entails comparing these measurements with Monte Carlo simulations. In order to perform such measurements, a silicon diode detector and a scan drive system have been developed.

In 2009, measurements of the γ-ray dose rate profile of the shut down Point Lepreau Generating Station reactor were conducted. By comparing the locations of the local peaks in the dose rate data, it was possible to determine the distances between the steel reactor components. The measured data were then compared with Monte Carlo simulations to determine how precisely one could locate the positions of the adjuster rods. Using this technique, it was found that the retracted adjuster rods were 440 ± 60 mm below their designed positions.

1. Introduction

Since it is possible for the components of a reactor to shift over time, it is necessary to be able to determine their positions accurately. For example, the positions of the components of a reactor can have an impact on the neutron flux shape within the core of the reactor. Thus, the primary objective of this work was to accurately determine the positions of Adjuster Rods 15 and 16 (See Figure 2). It was also necessary to obtain accurate information regarding the radiation field distribution inside a reactor for a number of reasons. One of these reasons is the establishment of safe work plans, based on the doses workers would receive. Another reason is that it is important to know the highest levels of radiation that the in-core instrumentation will experience. If the radiation field is too intense for a detector to perform properly, then it must be replaced by one that will, so that safe operation of the reactor is guaranteed.

A method to create a 1-dimensional radiation profile of the interior of the PLGS reactor has been proposed and implemented. By profiling the interior of the reactor, it is possible to determine the positions of features, such as the adjuster rods, of the reactor. It is important to know the positions of these features, since they have an impact on the operation of the reactor. While the measurements described in this paper were performed on a shutdown reactor that was undergoing refurbishment, the plan is to perform these measurements again on the same reactor shortly before it is started up again. Knowing the positions of the adjuster rods will aid in the understanding of any neutron flux shape tilts that may occur. The measurements on the shutdown reactor were performed to demonstrate the viability of this method. This method employs a combination of measurement of the γ-ray dose rate as a function of position within one of the access pipes in the reactor core (called Startup Instrumentation (SUI) tubes), and simulations of that dose rate in MCNP5, a Monte Carlo radiation transport program [1]. Monte Carlo simulations were performed to aid in the understanding of the measured data, and assist in more accurately determining the positions of the adjuster rods. Since the geometry of the reactor is rather complex, developing an analytic solution to the γ-ray emission and transport problem is extremely difficult. In addition to this, the anisotropic nature of γ-ray scattering further complicates the γ-ray transport problem. Thus, Monte Carlo was chosen as the modeling technique.

This paper begins by describing the γ-ray dose rate detection system. It then describes the measurements performed at the PLGS reactor while it was being refurbished. Finally, this paper discusses the MCNP5 simulations, and compares the simulation results with the measured data to draw conclusions about the positions of the components of the reactor with respect to their assumed positions.

2. The γ-ray Detector System

A small, inexpensive gamma-radiation detector, based on a commercially available Silicon (Si) p-n junction diode, has been developed. This detector can accurately measure γ-radiation fields over a wide dynamic range from 0.2 to 600 Gy/hr [2] [3] [4] The current of the Si diode provides a measure of the γ-ray dose received by the diode, since the current produced by the diode is proportional to the ionization energy deposited in it [5].

The detector consists of a disc-shaped diode (1 mm in diameter and 0.3 mm thick), encapsulated within a steel jacket. The very small, slender shape of the detector enables it to meet the requirement that it make point-like measurements of the dose rate. Tests at the Chalk River Laboratories of Atomic Energy of Canada Limited (AECL) demonstrated the ability of the diode sensor to perform well in radiation fields as high as 600 Gy/hr. These tests also demonstrated the ability of the detector to survive a total absorbed dose of 10 kGy with only a 5% decrease in dose rate response [3].

Calibrating the detector requires knowledge of the relationship between the current and the γ-ray energy absorbed (dose) by the diode per unit time. The current was measured as a function of γ-ray dose rate by exposing the detector to a nominally 3.7×10^{11} Bq, point-like Co-60 source. The dose rate was varied from 0.2 Gy/hr to 2 Gy/hr by changing the distance between the detector and the Co-60 source. Figure 1 shows a plot of the measured detector current versus dose rate. The dose rate response function of the detector is linear, in accordance with expectations [5]. The current-to-dose rate calibration factor was 28.3 pA/(Gy/hr) before the detector was exposed to the reactor. While it was in the PLGS reactor, the diode received a maximum dose rate of 1079 Gy/h. After the detector was exposed to the reactor, the current it emitted was re-measured as a function of dose rate by using another calibrated Co-60 source. The results of these measurements, which appear in Fig. 1, revealed a decrease in the current-to-dose rate calibration factor to 27.5 pA/(Gy/hr).

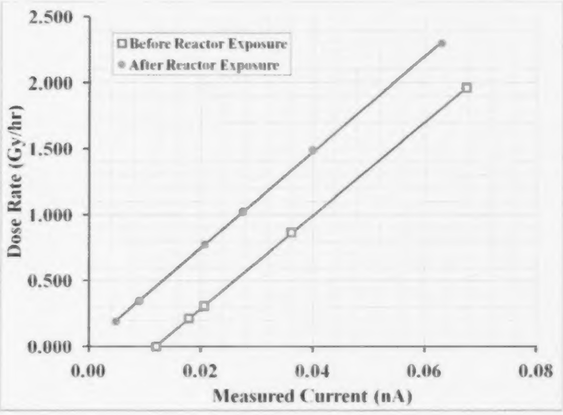

FIGURE 1
Plots of the diode detector current signal versus dose rate calibration data for the silicon diode detector. The offset between the y-intercepts of the two lines is due to the instrument offset of the Keithley 6487, and thus has no physical meaning.

An automated scan drive system was built to raise and lower the diode detector within the start up instrumentation (SUI) tube. The scan drive system consisted of four parts: a take-up reel, a stepper motor, a modified eddy current pusher and a rotary encoder. The Mineral Insulated (MI) cable was wrapped around the take-up reel. The stepper motor, which the data acquisition (DAQ) computer controlled via a motor controller, turned both the take-up reel and the four rubber wheels of the eddy current pusher. The rubber wheels of the eddy current pusher gripped the MI cable, and pushed or pulled it, depending on the motions of the stepper motor to which it and the take-up reel were geared. Finally, the rotary encoder, which touched the surface of the take-up reel, measured the position of the detector based on the distance take-up reel rotated. This system could position the detector to within 1 mm for every metre the diode travelled [4].

A Keithley 6487 picoammeter, with a dynamic range of 0.1 nA to 30.1 nA, was used to read the current from the detector. The error on the measured currents ranged from 0.001 nA to 0.46 nA [6]. After reading the detector's current, the Keithley sent its value to the Data Acquisition (DAQ) computer. In addition to the current signal, the DAQ computer also recorded the time of each measurement and the position of the detector.

3. Measurements of the γ-radiation Profile of the Reactor

A radiation profile measurement of the PLGS reactor was made to determine the positions of the withdrawn adjuster rods. The radiation dose rate profile of the shutdown reactor depended on both the operational history of the reactor and the amount of time that the reactor had been shutdown when the dose rate profile measurements were made. Thus, the positions of the adjuster rods and other features of the reactor were determined from the relative values of the measured dose rate. Nevertheless, the diode was calibrated to provide absolute values of the dose rates in the reactor for safe work planning.

The most basic parts of a CANDU® reactor are: the calandria, the core, the shielding surrounding the calandria, and the control and diagnostic instruments of the reactor.

The calandria, which is made of steel, holds the core. The core holds the fuel channels, and is filled with heavy water. The heavy water acts as a moderator, which slows downs the fast fission neutrons until they have thermal energies. During the measurements that this paper describes, the reactor had been shut down, and its core had been emptied of all of the fuel channels and heavy water. Thus, while the radiation profile measurements were being conducted in 2009, the calandria contained only air and a few access pipes. The access pipes enable the control and diagnostic instruments of the reactor to enter the core. The shielding that surrounds the calandria consists of light water (see Figure 2), surrounded by a 1220 mm thick concrete enclosure. Examples of diagnostic instruments that enter the access ports are neutron flux detectors, which provide the operators with neutron flux information, while the reactor is running. The adjuster rods are an example of control devices that enter the access ports. The adjuster rods and other control and diagnostic devices had been completely withdrawn from the core into the light water shielding during the 2009 radiation profile measurements [7].

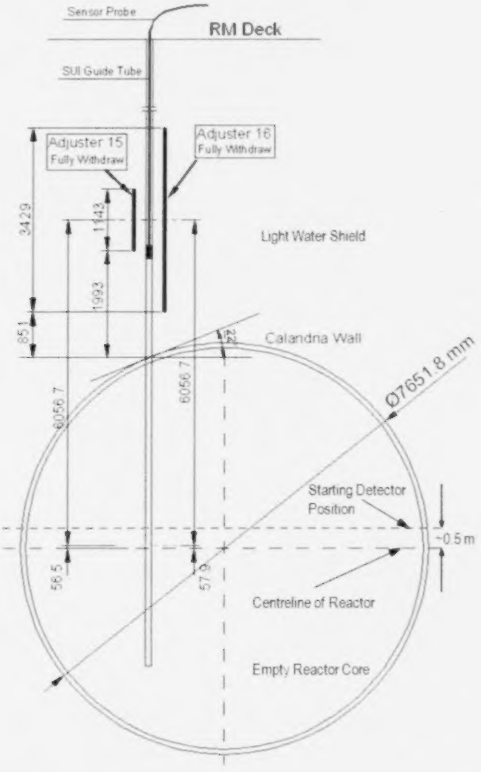

FIGURE 2
A diagram of the reactor features relevant to the PLGS dose rate profile measurements. The diagram includes the RM deck, the outer calandria wall, VP2 SUI guide tube and Adjuster Rods 15 and 16. In this diagram, the adjuster rods are in their fully retracted states.

The reactivity mechanisms (RM) deck of the PLGS reactor provided the platform for the γ-ray dose rate profile measurements (see Figure 2). The γ-ray scan equipment and DAQ were placed upon the RM deck, while the scan equipment moved the detector up and down the in-core start-up instrumentation (SUI) tube that was ported to viewport 2 (VP2).

The starting position of the detector was about 0.5 metres above the centreline of the core of the reactor (see Figure 2). The scan drive system took measurements from this position to a point 9970 mm above it in 10 mm increments. At each position, 30 current measurements were performed to reduce the noise in the current data.

While the reactor was running, the components of the reactor that were in the core absorbed the neutrons generated by fission reactions in the fuel. These reactor components are made of steel, aluminum and zirconium alloys. While steel is a strong neutron absorber, due to the large (n,γ) thermal cross sections of the isotopes of which it is composed, zirconium alloys and aluminum are rather weak neutron absorbers [8]. After absorbing the neutrons generated in the fuel, the reactor components became activated via (n,γ) reactions. These activation products range from Fe-55 to Ni-59 to Si-28, etc. Most of these activation products either have very short or very long half-lives, and thus, had either completely decayed away by the time of the measurement, or exhibited extremely low decay rates. The two activation products whose half lives are intermediate in duration are Fe-55 (999 d) and Co-60 (1925 d). Fe-55 emits mostly 6 keV X-rays, while Co-60, on the other hand, emits 1173 and 1332 keV γ-rays. Thus, the decay of Co-60 was the dominant source of radiation in these measurements. The Co-59 concentration in the zirconium alloys is typically 20 ppm or less [8]. The Co-59 concentration in the steel used in a CANDU® reactor is up to 700 ppm for the calandria shell and nozzles, and is estimated to be 2000 ppm for the adjuster rods. Therefore, the dominant sources of Co-60 γ-rays were the irradiated steel components of the reactor. These include the calandria walls and the adjuster rods. Brand new SUI tubes had been installed just before the measurements, and hence did not contain any Co-60. In the case of the radiation profile measurements, the calandria and the two adjuster rods adjacent to the VP2 SUI tube were the dominant sources of γ-rays. Figure 2 is a diagram of the reactor components that were germane to these measurements.

4. Experimental Analysis and Results

To minimize the impact of ambient electronic noise at the reactor facility, thirty current readings were taken at each detector position (10 mm increments). The statistical mode was then taken as the detector current for each set of five consecutive positions covering a 50 mm range. The mode rather than the mean was chosen, since the mean values were very noisy. The full width at half maximum (FWHM) of the current for each of these positions was also determined. The upper and lower errors on each mode current were then obtained from the differences between the mode current and the upper and lower limits of the FWHM. The modes were determined over 50 mm intervals, since these were the smallest intervals for which the FWHM limits were reasonably symmetrical and not oversized. The noise in the current data thus had a limiting effect on the accuracy of the position data. The error on the position, σ_z, is thus given by

$$\sigma_z^2 = \sigma_{scan}^2 + \sigma_{range}^2 \qquad (1)$$

The error on the ability of the scan drive to position the detector, σ_{scan}, is equal to Δz × (1 mm/m), where Δz is the distance in metres the detector travelled to reach the position z. The quantity σ_{range} is taken as half the 50 mm interval range. Based on Equation 1, the accuracy on the position varied from 25 mm for measurements near the bottom of the SUI tube to 27 mm for measurements near its top. The detector positions were taken as the central positions over each 50 mm mode interval.

The current mode values were converted to dose rates via linear current-to-dose rate conversions obtained from the calibrations described in Section 2. These linear conversion formulae consisted of the following: $D_1 = m_1 I$ and $D_2 = m_2 I$. D_1 is the linear fit obtained from the calibration data taken with the diode sensor before it was exposed to the reactor, and D_2 is the linear fit obtained after the diode was exposed to the reactor. The slopes of these two lines are $m_1 = 35.3731$ Gy/hr/nA and $m_2 = 36.3771$ Gy/hr/nA. The small increase in the slope of the calibration line is due to a gradual degradation of the ability of the diode to produce current as it was exposed to the radiation in the reactor. Thus, to obtain a better estimate of the dose rate, D, of the reactor from the measured currents and the two sets of calibration data, it was calculated from the error-weighted average of D_1 and D_2:

$$D = \left(\frac{D_1}{\sigma_{D_1}^2} + \frac{D_2}{\sigma_{D_2}^2} \right) \sigma_D^2 \qquad (2)$$

The errors, σ_D, on the dose rates were calculated via the following formula:

$$\frac{1}{\sigma_D^2} = \frac{1}{\sigma_{D1}^2} + \frac{1}{\sigma_{D1}^2} \qquad (3)$$

The errors on D, D_1, D_2 and the measured current are σ_D, σ_{D1}, σ_{D2} and σ_I [9]. The errors on D_1 and D_2 were simply calculated from $\sigma_{D1}^2 = I^2\sigma_{m1}^2 + m_1^2\sigma_I^2$ and $\sigma_{D2}^2 = I^2\sigma_{m2}^2 + m_2^2\sigma_I^2$. The errors on the current modes can be found from $\sigma_I^2 = \sigma_{Keithley}^2 + \Delta_{FWHM}^2$. The variable $\sigma_{Keithley}$ represents the error due to the uncertainty in the Keithley 6487 reading. The error due to the noise in the current readings is Δ_{FWHM}. Its value for a given position was calculated by taking the larger of the two differences between the mode current and the upper and lower FWHM limits. Thus, as one can see from Equation 4, the error on the dose rate, D, depends upon the measured current, I, and the two calibration factors, m1 and m2. The resulting plot of measured dose rates versus detector positions appears in Fig. 3.

$$\frac{1}{\sigma_D^2} = \frac{1}{I^2\sigma_{m_1}^2 + m_1^2\sigma_I^2} + \frac{1}{I^2\sigma_{m_2}^2 + m_2^2\sigma_I^2} \qquad (4)\ [9]$$

The horizontal axis of Fig. 3 was divided into three sections, named A, B and C. The largest measured dose rate of 1079±36 Gy/h occurred at a detector position of 17013±2.5 mm. The calandria (see Fig. 2), was the dominant source of Co-60 γ-rays. The main calandria shell alone contains about 2.7×106 cm3 of steel. In contrast, the two adjuster rods on either side of VP2 contain only about 1800 cm3 of steel. Since the calandria is the dominant source of γ-rays, and the calandria edge is the part of the calandria that is closest to the VP2 SUI tube, the inner edge of the calandria is expected

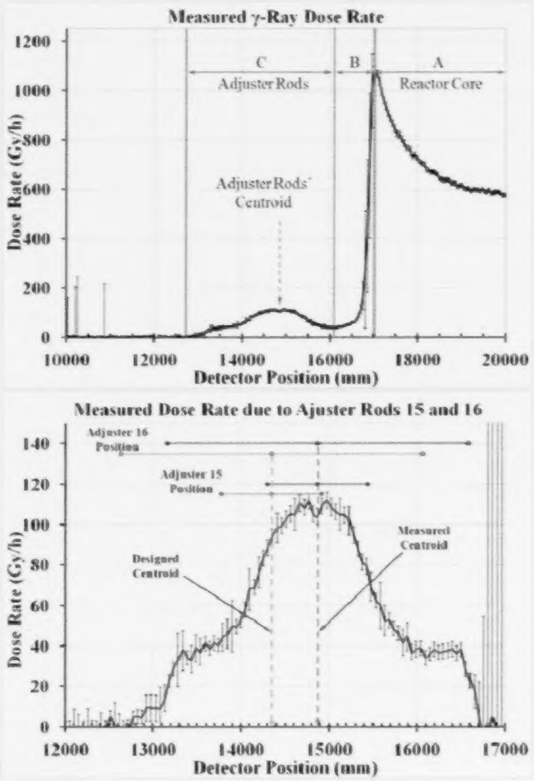

FIGURE 3

Top: A plot of the γ-ray dose rate profile measured within the VP2 SUI tube. Bottom: A plot of the measured γ-ray dose rate profile with the contribution of the calandria subtracted.

to be the position at which the dose rate was the largest. Therefore, in the analysis, it was assumed that the 17013 mm sensor position is the location at which the VP2 SUI tube meets the inner edge of the calandria wall. This 17013 mm peak position also marks the upper boundary of section A, which covers the calandria from its interior to its edge. The position at 17013 mm was used as a reference point to help in the determination of the locations of Adjuster Rods 15 and 16, which sit on either side of the VP2 SUI tube. Section B represents the locations between the edge of the calandria wall and the point at 16095 mm, which is the local minimum in the dose rate due to the calandria and the adjuster rods.

Section C covers the detector positions from 16095 mm to the point (12719 mm) at which the γ-ray field due to the adjuster rods first drops to 0.01 Gy/hr. Thus, the dose rate in Section C was assumed to be due to the adjuster rods alone, since they sit on either side of the VP2 SUI tube. The longer adjuster rod, Adjuster Rod 16, is 3429 mm long, and the shorter adjuster rod, Adjuster Rod 15, is 1143 mm long. All of the adjuster rods had been fully withdrawn from the core during these measurements. After converting the measured detector currents to dose rates, and determining the location of the calandria edge in the measured dose rate profile, the locations of Adjuster Rods 15 and 16 were extracted from the data. The first step in this process involved fitting a combined exponential-inverse square curve to the calandria dose rate data in Section B of the Fig. 3 plot. The equation obtained with this fit is

$$D = \frac{exp\left(-3.49 \times 10^{-3} \Delta z\right)}{2.86 \times 10^{-8} \Delta z^{2} - 1.18 \times 10^{-6} \Delta z + 8.25 \times 10^{-4}} \qquad (5)$$

In this formula, D is the fitted dose rate and Δz is the vertical distance above 17013 mm, the location of the calandria dose rate peak. The numerator of Equation 5 represents the exponential absorption of the γ-rays as they propagate through the water shielding above the calandria shell. The denominator, which is a quadratic in Δz, represents the inverse square decrease in the intensity of the γ-ray field with distance from the calandria shell. The fitted curve was then subtracted from the dose rate data to obtain the contributions solely due to the adjuster rods. In this fashion, the adjuster rod dose rate plot in Fig. 3 was obtained.

The centroid of the dose rate peak due to the adjuster rods appears at about 14868 mm. Assuming that the centres of Adjuster Rods 15 and 16 were aligned with the centroid of the dose rate peak, this suggests that the centres of the adjuster rod were 2145 mm above the calandria edge. The expected position of the centres of the retracted adjuster rods, based on the reactor commissioning data, was 2565.5 mm above the calandria edge (see Fig. 2). This suggests the possibility that the adjuster rods were out of position by 400 to 500 mm when in their fully retracted state. This deviation from the expected value of the positions of the adjuster rods is well beyond the 70 mm uncertainty which applies to the fully inserted position. In order to better understand the dose rate profile measurements, and more accurately determine the positions of the adjuster rods, simulations of the γ-ray dose rate profile of the PLGS reactor were performed in MCNP5.

5. Simulations with MCNP5

The following components of the shutdown PLGS reactor were simulated in MCNP5: the concrete shielding, the light water inside the concrete shielding, the calandria walls, the air inside the calandria, the VP2 SUI tube, a column of Si tally cells within the VP2 SUI tube, and Adjuster Rods 15 and 16.

In order to isolate the contributions of each activated steel component to the total γ-ray dose rate, one MCNP5 input file was created for each steel part. Accurately modeling the γ-ray sources due to these reactor components required the determination of the amount of Co-60 that had been produced in them while the reactor was running. While the reactor was running, Co-60 was produced by the capture of neutrons by Co-59, and decayed with a half-life, $\lambda_{Co\text{-}60}$, of 1925 days. Equation 6 shows this production and decay relationship. The product, $\phi_n\sigma_{Co\text{-}59}$, is average neutron flux times neutron capture cross section. This product gives the total ^{59}Co(n,γ)^{60}Co reaction rate. It is given by Equation 7, which is the sum or integral of the reaction rates at all of the neutron energies. Solving Equation 6 for $N_{Co\text{-}60}$ yields Equation 8, which gives the number of Co-60 nuclei as a function of time.

$$\frac{dN_{Co-60,i}}{dt} = \phi_n \sigma_{Co-59} - \lambda_{Co-60} \qquad (6)$$

$$\phi_n \sigma_{Co-60} \equiv \int \phi_n(E,r) \sigma_{n,\gamma}(E) dE \qquad (7)$$

$$N_{Co-60,i}(t) = \frac{V_i \rho_{Co-59} \phi\sigma}{\lambda_{Co-60} - \phi\sigma}\left[e^{-\phi\sigma t} - e^{\lambda_{Co-60} t}\right] \qquad (8)$$

In the above formulae, $N_{Co\text{-}60,i}$(r) is the amount of Co-60 as a function of position in reactor component *i*. V_i is the volume of reactor component *i* and $\rho_{Co\text{-}59}$ is the density of Co-59. The value of *t* is the total reactor run time. Finally, ϕ(E,r) is the neutron flux as a function of energy and position, and $\sigma_{n,\gamma}(E)$ is the neutron capture cross section for Co-59. The values of $\phi\sigma$ for the steel components were then calculated by running core criticality calculations of a generic CANDU® core model in MCNP5. Having obtained the simulated Co-60 density distributions within the calandria walls, nozzles and adjuster rods, these distributions were then used to simulate the γ-ray sources that were present in the PLGS reactor when the measurements were made.

6. Analysis of the Data Obtained via MCNP5 Simulations

Each γ-ray simulation provided the contribution of one of the steel components to the dose in each silicon tally cell in the SUI tube. MCNP5 provided these tally doses in units of MeV/g/γ-ray. Thus, in order to determine the contributions of the steel components to the total dose rate, it was necessary to determine the rate at which each component emitted γ-rays, which can be determined from the criticality calculation tallies, Equation 8, and the rate at which the reactor produced fission neutrons as a function of time and position [10]. The fission neutron production rate is given by Equation 9

$$\frac{dn}{dt} = \frac{P_{th}}{E_{rec}} \bar{\nu} \qquad (9)$$

The average thermal power of the PLGS, P_{th}, for each day from its initial start-up until it was shut down for refurbishment was provided by measurements taken by PLGS staff. The uncertainties on these power measurements were within 1%. The recoverable energy per fission, E_{rec}, was estimated to be 205.9 ± 0.6 MeV, assuming a mid-life burn-up percent fuel composition of 0.4% U-235, 99.4% U-238, 0.2% Pu-239 and 0.006% Pu-241. The average number of neutrons emitted per fission, $\bar{\nu}$, was estimated to be 2.83 ± 0.01 [11]. The values of $\phi\sigma$ for each steel reactor component were obtained from knowledge of the volumes of the steel parts, the neutron flux tallies associated with each steel part, and estimates of the cobalt impurity concentrations in the steel. As will be demonstrated in the next section, the uncertainties in the initial cobalt concentrations were the dominant sources of uncertainty in the simulated results. Armed with the estimated γ-ray emission rates of the steel reactor components, we then used them to convert the γ-ray dose rate tallies into total dose rates for comparison with the measured data.

7. Results of the MCNP5 Simulations

Figure 4 contains plots of the simulation results obtained with the analysis method described in the Section VI. The measured dose rate data are also included in the plots for comparison. The initial estimated ^{59}Co concentrations that were used to obtain the results in Figure 4 and Figure 5 were: 1) 1400 ppm (adjuster rods), 2) 560 ppm (mid-calandria shell), 3) 84 ppm (calandria sub-shells), 4) 84 ppm (calandria rings), 5) 119 ppm (calandria tubesheets) and 6) 700 ppm (nozzles). Since the cobalt concentrations are not well known, these cobalt concentrations were obtained by adjusting them until the simulated dose rate data matched the measured dose rate data. These cobalt impurity concentrations are all reasonable for stainless-steel alloys. According to PLGS staff, the cobalt concentration in the stainless steel of the adjuster rods was about 2000 pp. The cobalt concentration in the calandria shell was given as 700 ppm. Typical cobalt impurity concentrations in stainless steel range from 10 ppm to 700 ppm. The largest reasonable cobalt concentration in a stainless-steel alloy is about 2000 ppm. The errors on the cobalt impurity levels in the calandria shell pieces were estimated by calculating the dose rates with all of the initial cobalt concentrations set to 10 ppm and then to 700 ppm. The upper and lower error bars on the simulated calandria dose rate data were then obtained by calculating the differences between the dose rates obtained with the lower and upper values of the cobalt concentration and the values used to obtain Figure 4 and Figure 5. The errors on the cobalt impurity levels in the adjuster rods were estimated by taking half the difference between 700 ppm and 10 ppm.

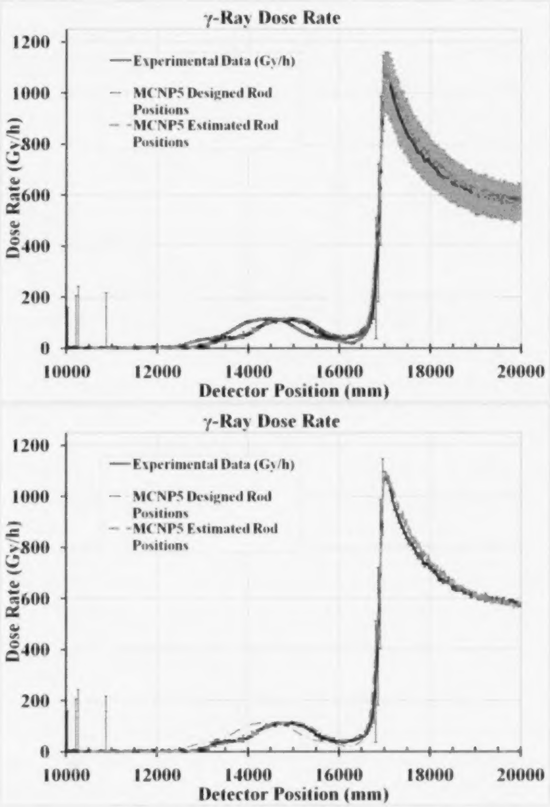

FIGURE 4
Top: Overlaid plots of the measured and simulated dose rates for the adjuster rods at their estimated and designed retracted positions with error bars on the simulated data. Bottom: Overlaid plots of the measured and simulated dose rates for the adjuster rods at their estimated and designed retracted positions without error bars on the simulated data.

The primary objective of performing the MCNP5 simulations was to determine the positions of Adjuster Rods 15 and 16 more accurately. This entailed aligning the simulated dose rate peak due to the calandria and nozzles with the measured dose rate peak, so that the simulated and measured curves would match each other as closely as possible. When compared with the MCNP5 geometry, it was found that the location of the 1079 Gy/hr peak in the dose rate data is 3421 mm above the centre axis of the main calandria shell. This is 97 mm below the inner calandria edge, which is 3518 mm above the centre of the calandria. This is due to the nearly 80 mm radius VP2 hole in the calandria shell. This hole results in a diminished dose rate at the calandria edge, where VP2 meets the calandria shell. The position error with which this alignment was made is estimated to be ± 30 mm, since that is the distance by which one can shift the alignment in the plots and still obtain a reasonable fit. Fig. 5 contains re-scaled plots of the dose rates obtained by simulating the adjuster rods 480 mm and 400 mm below their designed positions (MCNP5 Estimated Pos. 1 and Pos. 2). As one can see from the graph in this figure, the "Pos. 1" data and "Pos. 2" data bracket the measured dose rates associated with the adjuster rods. Thus, the estimated uncertainty with which the positions of the adjuster rods were simulated is half the distance between Pos. 1 and Pos. 2 or ± 40 mm. By adding the squares of the errors on the position measurement (27 mm), the alignment (30 mm), and simulated position (40 mm), we obtained a total error on the positions of the adjuster rods of 57 mm. The average of Pos. 1 and Pos. 2 is 440 mm, and hence, the conclusion is that the adjuster rods were 440 ± 60 mm below their fully retracted designed positions at the time of the dose rate profile measurements. Fig. 5, which includes the dose rate data obtained by simulating the adjuster rods at their designed positions, provides confirmation of the fact that the adjuster rods were out of position.

8. Conclusions

The γ-ray dose rate profile of a CANDU® reactor that was undergoing refurbishment was measured for the first time in 2009. This measurement employed a small, inexpensive silicon diode sensor and a scan drive system. These measurements produced a γ-ray dose rate profile that revealed the locations of the steel features of the PLGS reactor. The maximum reactor γ-ray dose rate was measured to be 1079±36 Gy/h. Based upon MCNP5 simulations, this dose rate maximum occurred about 90 mm below the calandria edge.

MCNP5 simulations helped to confirm the fact that the adjuster rods were out of position with respect to their fully retracted, out-of-core state. By combining the measured and simulated data, it was determined that the adjuster rods were off from their out of core position by 440 ± 57 mm.

Finally, this work demonstrated the fact that by combining the detector and scan drive system measurement technique with MCNP5 simulations, it is possible to obtain a one-dimensional image of the interior of a shut down reactor, based upon its γ-ray dose rate profile. Future experiments are being proposed to evaluate the fully inserted, in-core design positions of the adjuster rods by performing additional γ-ray profile scans.

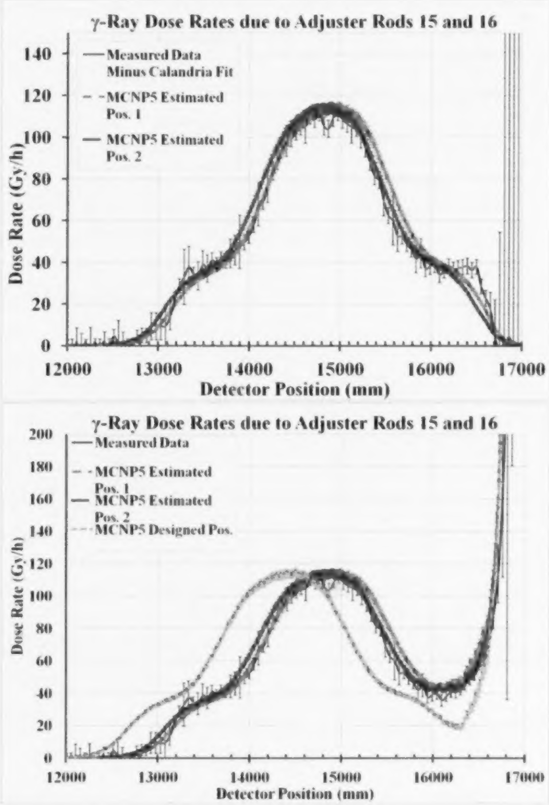

FIGURE 5

Top: Overlaid plots of the measured and simulated dose rates due to Adjuster Rods 15 and 16. The Position 1 data (MCNP5 Estimated Pos. 1) were created by simulating the adjuster rods at their estimated locations, 480 mm below their designed positions. The Position 2 data were generated by simulating the adjuster rods 400 mm below their designed positions. Bottom: Overlaid plots of the simulated dose rate data and the measured dose rate data in the region associated with the adjuster rods.

REFERENCES

[1] X-5 Monte Carlo Team, 2003, MCNP — A General Monte Carlo N-Particle Transport Code, Version 5, Volume I: Overview and Theory, LA-UR-03-1987, April 24, (Revised 2/1/2008)

[2] B. Sur, S. Yue, and A. Thekkevarriam, 2007, "Radiation Exposure Rate and Liquid Level Measurement Inside a High Level Liquid Waste (HLLW) Storage Tank", 28th Annual CNS Conference, Saint John, New Brunswick, Canada

[3] B. Sur, S. Yue and G. Jonkmans, 2009, "A Detector System for Measuring High Radiation Fields", Sixth American Nuclear Society International Topical Meeting on Nuclear Plant Instrumentation, Control, and Human-Machine Interface Technologies, Knoxville, Tennessee, USA

[4] S. Yue, et al., 2010, "Measurement of a Gamma Radiation Profile inside a CANDU® Reactor", Proceedings of the 18th International Conference on Nuclear Engineering, Xi'an, China

[5] G.F. Knoll, 1989, Radiation Detection and Measurement, 2nd Edition, John Wiley & Sons

[6] Keithley Instruments, 2002, Model 6487 Picoammeter/Voltage Source Reference Manual, Doc. No. 6487-901-01 Rev. A, Keithley Instruments, Inc. Cleveland, OH, USA

[7] P.M. Mathew, et al., 2009, "Severe Core Damage Accident Analysis for a CANDU Plant", OECD/NEA Workshop, "Implementation of Severe Accident Management Measures", Schloss Bottstein, Switzerland

[8] Allegheny Technologies Wah Chang, 2003, "Technical Data Sheet: Reactor Grade Zirconium Alloys for Nuclear Waste Disposal"

[9] Weisstein, Eric W. "Maximum Likelihood." From MathWorld--A Wolfram Web Resource. http://mathworld.wolfram.com/MaximumLikelihood.html

[10] John R. Lamarsh, 1966, Introduction to Nuclear Reactor Theory, Addison-Wesley Publishing Company, Inc.

[11] V. I. Kopeikin, et al., 2004, "Reactor as a Source of Antineutrinos: Thermal Fission Energy", Physics of Atomic Nuclei, Vol. 67, No. 10, pp. 1892-1899

FULL ARTICLE

OPTIMIZATION OF THE SPATIAL MESH FOR NUMERICAL SOLUTION OF THE NEUTRON TRANSPORT EQUATION IN A CLUSTER-TYPE LATTICE CELL

R.S. Davis*

Atomic Energy of Canada Limited, Chalk River Laboratories, Chalk River, Ontario, Canada, K0J 1J0

Article Info
Keywords: neutron transport equation, mesh optimization, cluster lattice cell
Article history: Received 15 April 2012, Accepted 25 June 2012, Available online 30 June 2012.
*Corresponding Author: (613) 584-3311 ext. 44278, davisr@aecl.ca

ABSTRACT

For programs that solve the neutron transport equation with an approximation that the neutron flux is constant in each space in a user-defined mesh, optimization of that mesh yields benefits in computing time and attainable precision. The previous best practice does not optimize the mesh thoroughly, because a large number of test runs of the solving software would be necessary. The method presented here optimizes the mesh for a flux that is based on conventional approximations but is more informative, so that a minimal number of parameters, one per type of material, must be adjusted by test runs to achieve thorough optimization. For a 37 element, natural-uranium, CANDU® lattice cell, the present optimization yields 7 to 12 times (depending on the criterion) better precision than the previous best practice in 37% less computing time.

1. Introduction

Many computer programs that solve the neutron transport equation require the input data to specify a computational mesh that partitions the space to be analyzed, and make the approximation that in each thus-defined mesh space the neutron flux (hereafter just called "flux") is constant as a function of position. The choice of the mesh structure directly affects the speed and precision of the resulting transport calculations. "Precision" in this context means agreement between the solution that the program calculates and an exact solution of the continuous transport equation that the program represents in its discretized approximation. Such precision is one of the requirements for the accuracy of a mathematical model; examples of other requirements are accuracy of physical data and conformance of the continuous equation to the actual physics. This statement supposes that imprecision is not to be deliberately introduced to cancel out inaccuracy from other sources, i.e. no phenomenological fitting. This paper describes a method of optimizing such a mesh, so that it yields more precise results using fewer mesh spaces than with earlier optimization methods, with particular application to a cluster-type lattice cell.

One purpose that mesh optimization can serve is economy; the mesh is to yield the best compromise between computing time, which depends primarily on the number of mesh spaces, and the precision of the results, which depends on their fineness. This goal is important if the mesh is to be used many times; for example, if a mathematical model that uses the mesh is to be validated for design and operation of nuclear facilities.

Another purpose that mesh optimization can serve is maximum precision. Finer mesh spaces reduce discretization error, but roundoff error increases with the number of mesh spaces, so that mesh optimization is also necessary for maximum precision. Since an exact solution of the transport equation is not available, a reference solution with maximum precision is necessary to gauge the precision of each mesh that is proposed for optimization for economy.

Optimization of a mesh involves test runs with varied meshes to learn the resulting precision and the execution time for each proposed mesh. An infinite variety of meshes can represent any one physical configuration, but practicality limits the number of test runs. Consequently, optimization requires inference techniques that can identify a practicably small subset of all possible meshes, with assurance that the optimum mesh will be in that subset. This paper describes an improved technique, which identifies a smaller such subset of the meshes that describe a cluster-type lattice cell than previous common practice, described below, identifies. As illustration, this paper uses it to optimize a two-dimensional representation of a 37 element, natural-uranium, CANDU® lattice cell [1, 2, 3, 4, 5] in the lattice code WIMS AECL [6], and compares that mesh with a mesh that was optimized for the same purpose, configuration, and software by previous common practice. The improved technique yields a greatly different mesh, which yields considerable gain in precision and somewhat reduced computing time compared with previous best practice.

2. Basic Previous Methods

The algorithm derived here that performs part of the optimization of a mesh is based on a technique of adaptive meshing that underlies most related previous work [6, 7, 8] as is shown below: since the flux in each mesh space is approximated to be constant, the imprecision incurred by the use of a proposed mesh is an increasing function of the greatest range, i.e., maximum minus minimum, of the actual flux in a mesh space. Thus, part of the optimization becomes the well-defined condition of having equal range of flux in each mesh space. Use of the actual flux in this measure would be impractical, but optimization can be achieved with an approximation of the actual flux.

Although this basic concept is widely used, there seems to be no standard name for the approximate flux thus used; it is hereafter called the "mesh-criterion flux". It is denoted $f(\vec{r})$; the origin of coordinates is the center of the fuel channel. The equation for $f(\vec{r})$ differs, depending on what part of the cell is at $\vec{r}$. Its units cancel out in use, so it is here considered unitless.

The optimization used by the cited and other work follows from the approximations that inside a cylindrical region of approximately uniform neutronic properties

$$f(\vec{r}) = a_1\, \rho_1(\vec{r})^2 + b_1 \qquad (1)$$

and outside a cylinder, in a surrounding region with properties contrasting the cylinder,

$$f(\vec{r}) = a_2 \log(\rho_2(\vec{r})) + b_2 \qquad (2)$$

in which $\rho(\vec{r})$ is distance from the central axis of the cylinder. These approximations follow from the diffusion equation in the limit of small distances [9].

The symmetry of these expressions implies that each such region is to be subdivided into annular mesh spaces with which to represent the discretized flux. Thus, the above-stated condition of equal range of flux in each mesh space is that

$$\max_{\vec{r} \in \text{Annulus}} (f(\vec{r})) - \min_{\vec{r} \in \text{Annulus}} (f(\vec{r})) = \frac{\max_{\vec{r} \in \text{Region}} (f(\vec{r})) - \min_{\vec{r} \in \text{Region}} (f(\vec{r}))}{N_{\text{Annulus}}} \qquad (3)$$

in which N_{Annulus} is the number of annuli used in a cylindrically bounded region.

The approximations in Equations (1) and (2) are realistic only if the coefficients a and b depend on neutron energy, but mesh-based transport-analysis software uses the same mesh at every energy. Equation (3) resolves this paradox; it yields a set of annuli that is independent of the coefficients a and b (with a removable singularity at $a = 0$), and thus has the necessary independence of energy. More sophisticated approximations would lack this property. With Equations (1) and (2), Equation (3) yields the results, found in the cited and much other work, that inside a cylinder the annuli have equal area, and outside an isolated cylinder the annuli have equal ratios of inner to outer radius.

The weakness of the approximations in Equations (1) and (2) is that they are appropriate only for isolated cylinders. Multiplicity of cylinders, such as fuel rods in a bundle and fuel channels in a lattice, causes azimuthal variation of flux and different fluxes in different fuel rods, for which those equations give no estimate. Proper account of these additional variables without a more informative mesh-criterion flux would call for an impractical number of test runs. Most related previous work, here called "previous common practice", uses an equal number of annuli in every fuel rod, an equal number of sectors in every annulus (except where sectors are obviously redundant because of symmetry), and an equal angle spanned by every sector in an annulus [6, 7, 8]. Even with these simplifications, additional test runs are required to decide the numbers of sectors, and yet the thus-derived mesh is not optimal, as is shown in Section 5.

3. Present Method

3.1 Basic Idea

The method of optimization presented here uses a mesh-criterion flux that is based on the conventional approximations in Equations (1) and (2), but that consists of more informative linear combinations of those expressions. It approximates the azimuthal dependence of the actual flux and relates fluxes in different parts of the lattice cell to the greatest extent possible with such approximations. An algorithm then derives an optimum mesh from that mesh-criterion flux, guided by parameters that must be adjusted by test runs. This approach reduces the number of parameters that must be adjusted by test runs to one parameter for each distinctive category of material, i.e. coolant, fuel, fuel sheaths, each material in the fuel channel (typically pressure tube, annular void, and calandria tube), and moderator. This seems to be the minimum set of parameters that must be determined by test runs, because the actual flux depends on the characteristics of these materials in a manner that requires transport calculations.

The parameters to be thus adjusted may be defined in various ways; those used here are interpretable as numbers of mesh annuli, hereafter denoted $N_{category}$, that are to be used in each of the above-listed categories of material, with dimensions that occur in the actual problem. This sort of definition facilitates human judgement in the selection of test runs, because it is familiar to users of the sort of transport software here considered. As is shown below, all the detailed parameters that characterize a mesh, denoted $N_{category}$ with additional subscripts, are uniquely determined by a set of values of $N_{category}$ for the above-listed categories, so that only the set of values of $N_{category}$ has to be selected by test runs.

Because fuel composition changes according to the flux in it, fuel is represented as a distinct material in each mesh space (except for amalgamation among mesh spaces that have equal fluxes because of symmetry), with uniform initial composition. The parameters $N_{category}$ thus determine not only the representation of the flux, but also the representation of the fuel materials.

This basic idea is applied below to a cluster-type lattice cell, such as in a CANDU lattice.

3.2 Structural Materials

Structural materials, i.e., fuel sheaths and fuel-channel components, are designed to have minimal effect on the neutron flux by choice of materials and by minimization of quantity. Consequently, representation of azimuthal variation in them has proven unnecessary if the fuel bundle is centered in the fuel channel [6, 7, 8]. Less symmetric configurations have not yet been analyzed by the methods described here. Because flux in structural materials is dominated by regions they surround, radial variation is represented in accordance with Equations (2) and (3). This procedure is no different from the previous common practice; one parameter for the mesh in each structural material is to be adjusted by test runs.

3.3 Lumen of Fuel Channel

3.3.1 Materials

To define the mesh-criterion flux in the lumen of the fuel channel, the materials to consider are coolant and fuel. Consequently, two parameters, $N_{coolant}$ and N_{fuel}, are used in the definition of the mesh-criterion flux in the lumen, and are to be chosen per test runs. In the following, $f(\vec{r})$ is defined using terms with a range of 1 over a cylinder containing one category of material, and each such term is multiplied by either $N_{coolant}$ and N_{fuel}. A maximum value of 1 is imposed on the range of the mesh-criterion flux in every mesh space in the lumen. This combination of normalization and condition has the effect that $N_{coolant}$ and N_{fuel} can be interpreted as numbers of annuli. A direct illustration of this feature follows Equation (5).

A consequence of this normalization is that in any subset of the lumen, the required number of mesh spaces is the Ceiling of the range of the mesh-criterion flux in that subset, in which Ceiling is a function that returns the smallest integer greater than or equal to the argument.

Since the fuel is in cylinders surrounded by the contrasting material coolant, and the lumen, containing fuel and coolant, is cylindrical and is surrounded by the contrasting materials fuel channel and moderator, the mesh-criterion flux in the lumen is based on adaptations of Equation (1) to these cylinders.

3.4 Mesh Optimization in Coolant

The mesh-criterion flux used in the coolant is, by adaptation of Equation (1),

$$f(\vec{r}) = f_{\text{Coolant}}(\vec{r}) \quad \text{for} \quad (\vec{r} \in \text{lumen}) \wedge (\vec{r} \notin \text{fuel rod}), \tag{4}$$

in which

$$f_{\text{Coolant}}(\vec{r}) = N_{\text{Coolant}} \frac{r^2 - R_{\text{Coolant Inner}}{}^2}{R_{\text{Coolant Outer}}{}^2 - R_{\text{Coolant Inner}}{}^2} + f(R_{\text{Coolant Inner}}). \tag{5}$$

$R_{Coolant\ Outer}$ is the inside radius of the fuel channel, and $R_{Coolant\ Inner}$ is the radius of the central rod of the fuel bundle if there is one, 0 if not. r is the magnitude of $\vec{r}$ and is equal to $\rho(\vec{r})$. $f(R_{Coolant\ Inner}$ is defined by Equation (6) below as the mesh-criterion flux at the surface of the central fuel rod if any, 0 if not. Because the range of $f(\vec{r})$ in the coolant is $N_{Coolant}$ and the range of $f(\vec{r})$ in each mesh space is limited to 1, $N_{Coolant}$ is the number of annuli.

Azimuthal dependence in coolant does not need to be represented, because the fuel rods are packed closely in comparison with mean free paths in the coolant, and symmetrically [6, 7, 8]. The resulting mesh in the coolant is identical to the previous common-practice mesh, per Equation (3), but Equation (5) has further importance because of its use in the following section.

Because of the small neutronic effect of fuel sheaths, the mesh-criterion flux is defined to be continuous at the boundaries that would exist between fuel and coolant in the absence of the sheaths. Thus, even though Equations (4), (6), and (7) have domains in different materials, they are interrelated by this condition of continuity at the boundaries between their domains. Equation (5) includes constant terms whose purpose is to satisfy this continuity condition, even though they have no effect in the derivation of the mesh by Equation (3). In related equations below, this condition of continuity is practically important; adherence to it in Equation (5) maintains logical consistency.

3.5 Mesh Optimization in Fuel

3.5.1 Mesh-Criterion Flux in Fuel

The mesh-criterion flux in the central rod of the fuel bundle, if there is one, or that otherwise would be considered to apply in the innermost rod of the fuel bundle if it were central, is, by adaptation of Equation (1),

$$f(\vec{r}) = N_{\text{Fuel}} \frac{r^2}{R_{\text{Inner Fuel}}^{\;2}} \quad \text{for} \quad (\vec{r} \in \text{central fuel}) \qquad (6)$$

in which $R_{Inner\ Fuel}$ is the radius of the fuel in the fuel rod closest to the cell's center, which is the central fuel rod if one exists. The numbers of annuli used in different fuel rods depend on N_{Fuel} through Equations (7) and (8), which contain expressions that do not generally yield integer values even when N_{Fuel} is an integer. For this reason, a non-integer value of N_{Fuel} will in general result from the optimization, and the number of annuli used in a central rod is Ceiling(N_{Fuel}). If there is no central fuel rod, then Equation (6) only serves as a definition of the parameter N_{Fuel} by stating how many annuli the innermost rod would have if it were central.

In a non-central cylinder of fuel, the mesh-criterion flux is the sum of Equations (5) and (6), applied at the location of the cylinder,

$$f(\vec{r}) = f_{\text{Coolant}}(\vec{r}) + N_{\text{Fuel}} \frac{\left(\vec{r} - \vec{P}_{\text{Fuel}_j}\right)^2 - R_{\text{Fuel}_j}^{\;2}}{R_{\text{Inner Fuel}}^{\;2}} \quad \text{for} \quad (\vec{r} \in \text{fuel cylinder number } j) \qquad (7)$$

in which $\vec{P}_{\text{Fuel}_j}$ is the center of the fuel rod and $R_{\text{Fuel}j}$ is its radius. This sum satisfies the condition of continuity of flux between coolant and fuel, and it thus represents the increase in the gradient of the flux in the fuel that is caused by proximity to the moderator [6]. Because $R_{\text{Fuel}j}$ is constant, its inclusion in Equation (7) has no effect on the derived mesh; but it yields continuity between fuel and coolant, which is essential to the logic. Because the two terms in Equation (7) are multiplied by the two independent quantities $N_{Coolant}$ and N_{Fuel}, the sum does not represent the actual flux in any energy group. Rather, a high value of N_{Fuel} leads to a correspondingly exaggerated gradient of the flux in the fuel. This yields correspondingly enhanced fineness of the mesh in the fuel.

The use of $R_{\text{Inner Fuel}}^{\;2}$ in Equation (7) implies that the parameter a in Equation (1) is the same in fuel rods of different radii and that the number of annuli necessary in a central rod depends quadratically on its radius, which is a reasonable approximation if their initial compositions are the same. The present process has not been applied with fuel rods of different initial compositions; with strong differences, distinct values of N_{Fuel} for each initial composition would presumably be necessary for good optimization.

Thus, geometry and two quantities chosen per test runs, $N_{Coolant}$ and N_{Fuel}, completely determine the mesh-criterion flux in every fuel rod and in the coolant. That and the condition of a maximum range of 1 in each mesh space then completely determine the mesh in fuel and coolant as follows.

3.6 Optimization of Annuli in Fuel

The restriction to a range of 1 in each annulus and the difference in $f(\vec{r})$ between the center of a cylinder of fuel and its surface nearest the moderator yields the number of annuli in fuel cylinder number j,

$$N_{\text{Fuel}_j} = \text{Ceiling}\left(f\left(\vec{P}_{\text{Fuel}_j} + R_{\text{Fuel}_j}\hat{P}_{\text{Fuel}_j}\right) - f\left(\vec{P}_{\text{Fuel}_j}\right)\right) \qquad (8)$$

in which $\hat{P}_{\text{Fuel}_j}$ is a unit vector pointing away from the center of the fuel channel, i.e. $\vec{P}_{\text{Fuel}_j} / P_{\text{Fuel}_j}$, and the condition of uniform range of mesh-criterion flux implies that the outside radius of the k^{th} annulus in fuel cylinder number j is

$$\rho_{\text{Fuel}_{j,k}} : f\left(\vec{P}_{\text{Fuel}_j} + \rho_{\text{Fuel}_{j,k}}\hat{P}_{\text{Fuel}_j}\right) - f\left(\vec{P}_{\text{Fuel}_j}\right) = \left(f\left(\vec{P}_{\text{Fuel}_j} + R_{\text{Fuel}_j}\hat{P}_{\text{Fuel}_j}\right) - f\left(\vec{P}_{\text{Fuel}_j}\right)\right)\frac{k}{N_{\text{Fuel}_j}} \qquad (9)$$

in which $1 \le k \le N_{\text{Fuel}_j}$.

Figure 1C shows in a particular example (described below) how the annuli become finer as fuel rods are farther off-center, in addition to the conventional trend toward thinner annuli toward the outside in each fuel rod.

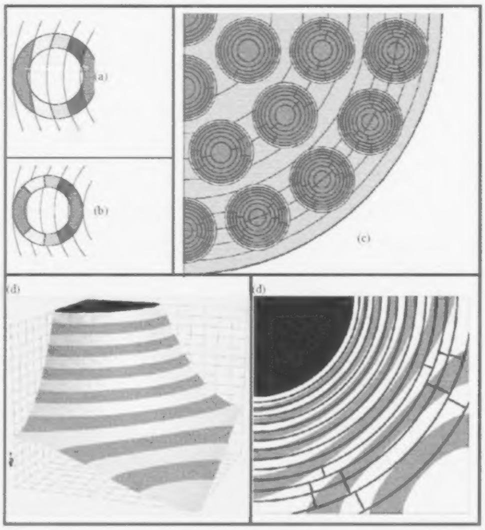

FIGURE 1
Derivation of mesh from mesh-criterion flux. (a) annulus in fuel, divided along contours of mesh-criterion flux in coolant; (b) approximation of division in above figure with sectors; (c) optimum mesh in the lumen for 37-Element example; (d) surface plot of mesh-criterion flux in moderator in one quadrant of a cell; (e) contour plot and optimum mesh for above example, in moderator.

3.7 Optimization of Sectors in Annuli Fuel

The second term in Equation (7) is invariant under rotation about the center of the cylinder; all the azimuthal dependence in Equation (7) is in the first term, which is identical to Equation (5). In the optimization of sectors within the above-described annuli, $f(\vec{r})$ may be defined by either of those equations with the same result. For simplicity, Equation (5) is used here.

The required number of angular subdivisions in the k^{th} annulus is determined by the range of the azimuthal variation of the mesh-criterion flux in that annulus. Thus,

$$N_{\text{Fuel}\,j,k} = \text{Ceiling}\left(f\left(\vec{P}_{\text{Fuel}\,j} + \rho_{\text{Fuel}\,j,k}\,\hat{P}_{\text{Fuel}\,j}\right) - f\left(\vec{P}_{\text{Fuel}\,j} - \rho_{\text{Fuel}\,j,k}\,\hat{P}_{\text{Fuel}\,j}\right)\right) \quad (10)$$

If $N_{\text{Fuel}\,j,k} \leq 1$, the annulus is not divided into sectors. Otherwise, Figure 1A shows an exemplary annulus with $N_{\text{Fuel}\,j,k} = 5$, subdivided along contours of Equation (5), which occur at uniform steps of the value of Equation (5). However, WIMS AECL and similar software subdivides annuli along azimuthal boundaries, into sectors. Consequently, the subdivision in Figure 1a is approximated by the sectors exemplified in Figure 1b, such that each defining contour of Equation (5) intersects a sector boundary at the root-mean-square radius of the annulus,

$$\overline{\rho}_{\text{Fuel}\,j,k} = \left(\rho_{\text{Fuel}\,j,k}{}^{2} + \rho_{\text{Fuel}\,j,k-1}{}^{2}\right)^{1/2}$$

Thus, the angles are

$$\theta_{\text{Fuel}\,j,k,l} : f\left(\vec{P}_{\text{Fuel}\,j} + \overline{\rho}_{\text{Fuel}\,j,k}\left(\Re\left(\theta_{\text{Fuel}\,j,k,l}\right)\hat{P}_{\text{Fuel}\,j}\right)\right) - f\left(\vec{P}_{\text{Fuel}\,j} - \rho_{\text{Fuel}\,j,k}\,\hat{P}_{\text{Fuel}\,j}\right) =$$
$$\left(f\left(\vec{P}_{\text{Fuel}\,j} + \rho_{\text{Fuel}\,j,k}\,\hat{P}_{\text{Fuel}\,j}\right) - f\left(\vec{P}_{\text{Fuel}\,j} - \rho_{\text{Fuel}\,j,k}\,\hat{P}_{\text{Fuel}\,j}\right)\right) \frac{l}{N_{\text{Fuel}\,j,k}} \quad (11)$$

in which $\Re(\theta)$ is a rotation operator through the azimuthal angle θ , and $0 < l < N_{\text{Fuel}\,j,k}$. For each such *l*, two symmetrically related solutions θ exist, so there are $2\,N_{\text{Fuel}\,j,k} - 2$ sectors. Figure 1C shows in a particular example how the mesh boundaries between sectors conform in their spacing, but do not necessarily coincide, with mesh boundaries in the coolant.

A pair of sectors that are defined by the same values of *l* will have equal fluxes by symmetry, and therefore may be defined to have the same material, as is illustrated by the colors in Figures 1a and 1b. Although an annulus has $2\,N_{\text{Fuel}\,j,k} - 2$ sectors, only $N_{\text{Fuel}\,j,k}$ different fluxes occur in them. In the example in Figure 1c, the fuel is represented as 50 different materials, though with uniform initial composition.

3.8 Moderator

3.8.1 Mesh-Criterion Flux in Moderator

The mesh-criterion flux in the moderator is defined to satisfy reflective or periodic boundary conditions on the cell boundaries, by supposing that it is in an infinite lattice. Departures from such boundary conditions are managed independently of the optimization process, as is described in Section 5. The mesh-criterion flux is

$$f(\vec{r}) = -\sum_{\vec{P}_{\text{Channel}\,j} \in K(N)} \left(\log\left(\left|\vec{r} - \vec{P}_{\text{Channel}\,j}\right|\right)\right) + \frac{2\pi\,\vec{r}^{\,2}}{s\tan(\pi/s)\,P_1^2} \quad \text{for} \quad (\vec{r} \in \text{moderator}) \quad (12)$$

The origin of coordinates is the center of the cell. P_1 is the distance from there to the center of a nearest neighbor. *K(N)* is the set of locations of centers of fuel channels at distances $\leq N\,P_1$ from the center of the cell of interest (including distance 0); the x axis points to a nearest neighbor. *s* is the number of sides of each cell, e.g., four for a square lattice. The first term represents the mesh-criterion flux in the moderator due to each cell with a channel in *K(N)* per Equation (2). The second term represents the infinite number of other cells approximated as a continuous medium, which yields a flux in the cylinder occupied by *K(N)* per Equation (1). Equation (12) has no particular normalization; there is no simplification analogous to the normalization of the mesh-criterion flux in the lumen because of the weighting in Equation (13).

Equation (12) only approximately satisfies the boundary condition of zero gradient perpendicular to the cell's boundaries. The coefficient of $\vec{r}^{\,2}$ is determined by the condition that the perpendicular gradient integrated around the cell's boundaries is 0. The approximation improves, i.e., the maximum magnitude of perpendicular gradient across the boundary decreases, as *N* increases. The set *K(3)* is recommended; it has only 29 members in a square lattice, but it satisfies the reflective boundary condition with precision, defined by (maximum magnitude of gradient across boundary linearly extrapolated across cell) / (range of $f(\vec{r})$ in moderator), better than 0.1%. Equation (12) with *K(3)* for one quarter of a square lattice cell is shown as a surface plot in Figure 1d, and as a contour plot in Figure 1e.

3.8.2 Optimization of the Mesh in the Moderator

The number of annuli used in the moderator is $N_{\text{Moderator}}$, which is another parameter to be optimized by test runs. As a function of the magnitude, r , the mesh-criterion flux has its greatest range when $\vec{r}$ is directed along a diagonal, e.g. in the direction π/s . The mesh in the moderator cannot be optimized by setting the radii of the annuli and then assigning sectors in each, as elsewhere in the cell, because of the more complicated dependence of the mesh-criterion flux on position. However, in the procedure used here, an initial assignment is made, that annulus *j* has outside radius

$$r_{\text{Moderator}\,j} : \left(f\left(\vec{r}\left(R_{\text{Channel}}, \pi/s\right)\right) - f\left(\vec{r}\left(r_{\text{Moderator}\,j}, \pi/s\right)\right)\right) = \left(f\left(\vec{r}\left(R_{\text{Channel}}, \pi/s\right)\right) - f\left(\vec{r}\left(\frac{P_1}{2\cos(\pi/s)}, \pi/s\right)\right)\right) \frac{\sum_{k=1}^{j} w_k}{\sum_{k=1}^{N_{\text{Moderator}}} w_k} \quad (13)$$

in which the positions $\vec{r}$ are expressed in polar coordinates of radius and angle. R_{Channel} is the inside radius of the moderator. The weights, w_k , are all 1 for this initial assignment.

Sectors are assigned to each annulus in accordance with its radii. Minimization of the number of mesh spaces subject to a restriction on the range of the mesh-criterion flux is equivalent to maximization of the area of each mesh space subject to the same restriction. In a first-order approximation, this maximum occurs when the radial variation and the azimuthal variation of the mesh-criterion flux are equal. Consequently, in annulus number *j*, in each of the 2*s* symmetrically related sectors, the number of sectors is

$$N_{\text{Moderator}\,j} = \text{NInt}\left(\frac{f\left(\vec{r}\left(\bar{r}_{\text{Moderator}\,j},\theta_{\min j}\right)\right)-f\left(\vec{r}\left(\bar{r}_{\text{Moderator}\,j},\pi/s\right)\right)}{f\left(\vec{r}\left(r_{\text{Moderator}\,j-1},\pi/s\right)\right)-f\left(\vec{r}\left(r_{\text{Moderator}\,j},\pi/s\right)\right)}\right) \tag{14}$$

in which NInt (x) is a function that returns the integer nearest x, $\bar{r}_{\text{Moderator}\,j} = \left(r_{\text{Moderator}\,j}{}^2 + r_{\text{Moderator}\,j-1}{}^2\right)^{1/2}$

is the root-mean-square radius of moderator annulus *j*, and $\theta_{\min j} = \cos^{-1}\left(\tfrac{1}{2}P_1/\bar{r}_{\text{Moderator}\,j}\right)$

if the circle of radius $\bar{r}_{\text{Moderator}\,j}$ intersects the cell boundary, 0 otherwise.

If $N_{\text{Moderator}j}$ >1 then $N_{\text{Moderator}j}$ sectors are defined in each symmetrically related sector. Their bounding angles are such that the range of the mesh-criterion flux is the same in every sector in annulus number *j*. Any adjacent two sectors whose common boundary is one of the 2*s* lines of reflection symmetry are then merged, because the range of the mesh-criterion flux is no greater in that union than in its components.

In accordance with Section 2, the incurred error attributed to each annulus is the range of the mesh-criterion flux in each of its sectors if it has them, or in the whole annulus if not. The criterion of optimization requires all of the attributed incurred errors to be equal. Although the above-described steps are designed for that goal, the attributed incurred errors typically vary, because Equation (14) changes discontinuously as a function of the properties of an annulus. Worst is the transition in consecutive annuli from no sectors to two sectors, which changes the attributed incurred error by almost a factor 2.

As a partial remedy, the radii of the annuli are then reassigned per Equation (13), but this time weight is the inverse of the incurred error attributed to annulus number k. Then, the above-described assignment of sectors per Equation (14) is repeated. This reduces the range of variation of the attributed incurred errors typically to ±20% of the average. Better apportionment of these weights would yield better optimization, but further iteration by the above-described procedure makes the mesh worse, not better, because of the discontinuous behavior of Equation (14).

4. Tracking Lines

In software that uses collision probabilities, such as WIMS-AECL, most of the computing time is consumed in preparing a matrix of collision probabilities. This time depends on the number of tracking lines, which are used for ray tracing [6], as well as the fineness of the mesh. For the sake of precision consistent with the fineness of the mesh, different spacings are used for different ranges of distance of tracking lines from the cell center. The spacing of tracking lines in each radial range is proportional to the thickness of the thinnest annulus through which each tracking line passes at its closest approach to the center of the lattice cell. The ratio is denoted N_{Line}, defined such that a larger value means more lines, and is another parameter to be optimized by test runs.

The number of angles of tracking lines, N_{Angle}, is another parameter to be optimized by test runs. One value is used throughout each test run.

5. Results for 37-Element Example

5.1 Choice of Parameters

The above logic yields an optimized mesh, given a set of values of the parameters. The other component of optimization is the choice of that set of values. Even with the more informative mesh-criterion flux, this optimization occurs in a rather high-dimensioned space. The mesh in structural materials is fairly simple to optimize, and the present method offers no improvement on previous common practice. Test runs with the present mesh optimization have confirmed earlier findings that, for economy, one annulus in each such material is optimum, and for the highest precision one annulus in each fuel sheath and three annuli in each other structural material suffice. However, there remain the five parameters N_{Coolant}, N_{Fuel}, $N_{\text{Moderator}}$, N_{Line}, and N_{Angle}.

Although sophisticated methods exist for optimization in multidimensional space with a minimum number of test runs, for the present work many sets of these parameters have been given test runs, with the goal of general understanding of the effects of varied choices as well as finding an optimum.

5.5 Optimization Metrics

Although the mesh-criterion flux derived above closely resembles plots of actual flux [6], its ultimate test is the agreement between calculations made with meshes optimized in accordance with it and a reference calculation optimized for precision. The reference calculation for the 37 element, natural-uranium, CANDU lattice cell [1, 2, 3, 4, 5] example used here is derived from the parameters $N_{Coolant} = 40$, $N_{Fuel} = 8.2$, $N_{Moderator} = 60$, $N_{Line} = 4.4$, and $N_{Angle} = 11.1$ annulus in each fuel sheath, and 3 annuli in each fuel-channel component. (This fineness makes a diagram impracticable.)

Two metrics of agreement are used throughout the present work: agreement of k_∞ , and agreement of change of k_∞ upon removal of coolant. The latter is hereafter called "CVR" for "coolant void reactivity". From each test run, these quantities are compared at a predetermined set of five irradiation times that correspond approximately to fresh fuel, equilibrium short-term poison, maximum k_∞ , half-way thereafter to the following point, and $k_\infty = 1$ Root-mean-squares over those five irradiation points of the two metrics are shown in Figure 2. A few test runs have also gauged the degrees of agreement in change of k_∞ as a function of fuel temperature and of moderator boron concentration. Agreements by these criteria are similar to the agreements in CVR. These optimization metrics are the important ones for applications thus far made of the present process; it has not been tested against other optimization metrics, such as detailed power and flux distributions.

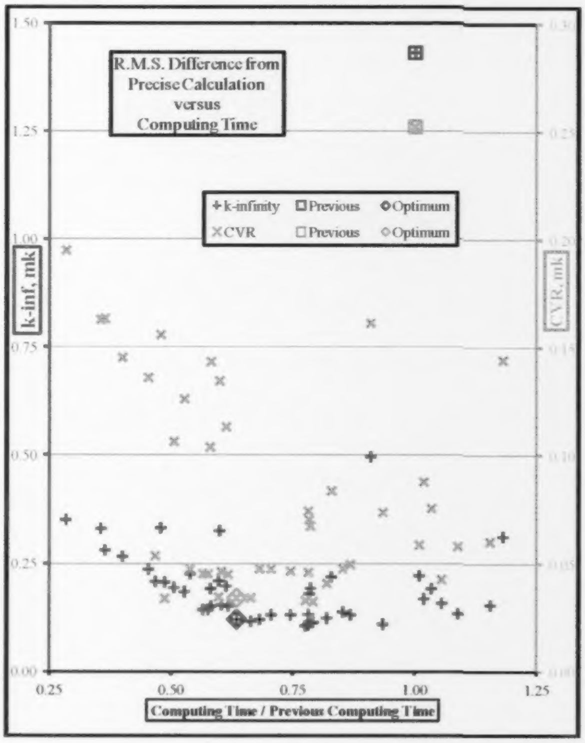

FIGURE 2
Root-Mean-Square differences from precise calculation in milli-k versus computing times relative to previous best practice for 37-Element example.

Finer and coarser reference meshes have also been tried; results have nearly the same relative positions as shown in Figure 2, but with the whole set of discrepancies shifted higher by 0.1 to 0.2 milli k. Thus, the present reference mesh seems to be near a shallow optimum of precision.

Computing times shown in Figure 2 are expressed as multiples of the computing time on the same computer with a previous "standard" mesh, which is further described below.

5.3 Optimization

The best possible precisions for different amounts of computing time are the lower envelopes of the two sets of results. Figure 2 shows that greater computing time can be rewarded with greater precision up to 0.63× the computing time for the previous best-practice mesh, and computing time above that is wasted; a discontinuity in the trend occurs at that point in the agreements for k_∞ , and the agreements for CVR, although not so clearly patterned, are consistent with it. The mesh at that transition is labelled "Optimum" in Figure 2, because it will indeed be optimal for any purpose other than an overwhelming need for speed. Its parameters are $N_{Coolant} = 10$, $N_{Fuel} = 4.2$, $N_{Moderator} = 15$, $N_{Line} = 1.5$, and $N_{Angle} = 7$. It is shown in Figures 1c and 1e.

5.4 Comparison with Previous Common-Practice Optimization

5.4.1 Subject of Comparison

The above-described "optimum" mesh is here compared with a mesh that was previously designed as a "standard" mesh for the same configuration. Like the "optimum" mesh derived here, that previous mesh is optimized for a good compromise of speed with economy, and intended to be run on the same version of WIMS AECL [6], using present-day computing hardware. The one important difference is that that mesh was designed according to previous common practice as described in Section 2. Because of these similarities and differences, that mesh is referred to here as "previous best practice". It is shown in Figures 3a and 3b.

5.4.2 Precision

Figure 2 also shows precisions obtained with the previous best-practice mesh; they are near the upper-right, i.e., least favorable corner. In 0.63× the computing time for the previous best-practice mesh, the "optimum" mesh yields about 12× better precision in k_∞ and 7× better precision in CVR. These strong differences correspond with strong contrasts between the two meshes, which are described below.

5.4.3 Mesh in Lumen

The respective meshes in the lumen are shown in Figures 1c and 3a. In the coolant, the optimum mesh is identical to the previous best-practice mesh. In the fuel, the previous best-practice mesh has the same 4 annuli in each cylinder of fuel, with 2 sectors in each annulus except in the central rod, making 8 mesh spaces in each fuel cylinder except for 4 in the central rod. The optimum mesh in the fuel is much finer and more varied; the consecutive rings of fuel have 5, 6, 6, and 7 annuli, and the numbers of sectors range from 1 to 6. In the outer ring, each cylinder of fuel has 22 subdivisions after deducting for symmetry per Section 3, versus 8 in the previous best-practice mesh there. This contrast is probably the main reason for improved precision.

5.4.4 Mesh in Moderator

The opposite contrast occurs in the moderator; the respective meshes are shown in Figures 1e and 3b. The previous best-practice mesh there has there 36 annuli, totalling 434 mesh spaces. The optimum mesh has only 15 annuli, totalling only 62 mesh spaces. The contour bands that underlie the mesh in Figure 1e show how the apportionment of sectors results from optimization according to the mesh-criterion flux. Although the optimum mesh uses only 1/7 as many mesh spaces, the narrowest sectors in the optimum mesh have angular span of only 9.7°, while all the sectors in the previous best-practice mesh have angular spans of 15°. This means that most of the sectors in the previous best-practice mesh have wastefully small ranges of the mesh-criterion flux, yet some of those sectors have larger ranges than in the optimum mesh.

Similar contrast occurs in the apportionment of annuli, and is due to the representation of reflective boundary conditions in the present mesh-criterion flux. Indeed, test runs show good precision with $N_{\text{Moderator}} = 12$, but a value of 15 allows for deviation from reflective boundary conditions in a multicell case. Similarly, although the above-described optimization yields a particularly large mesh space in each corner of a square cell as shown in Figure 1e, that mesh space is divided into two radially for better representation in a multicell case.

6. Conclusion

For neutron-transport software that divides the analyzed configuration into mesh spaces and makes the approximation of constant flux in each such space, optimization of the mesh can have great effects on the accuracy of the solution and on the execution time. For a lattice cell with cluster geometry, inference of an optimum mesh from the mesh-criterion fluxes given by Equations (7) and (12), in comparison with the previous best practice based on Equations and (2), enables an optimum mesh to be formed with fewer test runs of the solving software, and produces a mesh that requires less computing time but produces a considerably more precise result for the integral parameters against which it has been tested. This conclusion has not yet been tested against detailed parameters, such as power and flux distributions.

Improved precision stems mainly from informed, finer subdivision in fuel rods, emphasizing those that are farther off-center, while improved execution time stems mainly from informed reduction in the number of subdivisions in the moderator. However, the latter reduction can degrade flux mapping in the moderator.

The observed improvements stem ultimately from use of a more informative mesh-criterion flux. In other transport calculations, optimization by means of similarly informative mesh-criterion fluxes may also improve precision and/or reduce computing time.

7. Acknowledgements

The author thanks the following colleagues in AECL for their knowledgeable help in the work described and in the preparation of this paper: F. Adams, N. Alderson, D. Altiparmakov, J. Pencer, S. Pfeiffer, D. Roubtsov, A. Trottier. The author is solely responsible for any errors of fact or deficiencies in expression that remain in spite of their help.

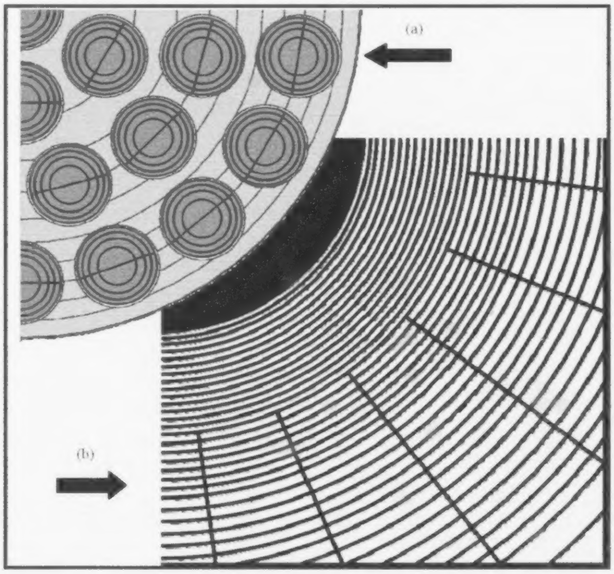

FIGURE 3
Previous best practice mesh; (a) previous best practice lumen; (b) previous best practice moderator.

REFERENCES

[1] International Atomic Energy Agency, Vienna, June 1996, "In Core Fuel Management Benchmarks for PHWRs", IAEA-TECDOC-887
[2] International Atomic Energy Agency, Vienna, April 2002, "Heavy Water Reactors: Status and Projected Development", Technical Reports Series No. 407
[3] K.S. Kozier, 2002, "Assessment of CANDU Reactor Physics Effects Using a Simplified Whole-Core MCNP Model", PHYSOR 2002 Conference, Seoul, Korea
[4] M.A. Lone, 2001, "Fuel Temperature Reactivity Coefficient of a CANDU Lattice Numerical Benchmark of WIMS AECL (2 5d) Against MCNP", 22nd Annual Conference of the Canadian Nuclear Society, Toronto, Canada
[5] J.M. Pounders, F. Rahnema, D. Serghuita, and J. Tholammakkil, 2011, "A 3D stylized half-core CANDU benchmark problem", Annals of Nuclear Energy, 38(4), pp. 876-896
[6] D. Altiparmakov, September 2008, "New Capabilities of the Lattice Code WIMS AECL", PHYSOR 2008 Conference, Interlaken, Switzerland
[7] G. Harrisson and G. Marleau, April 2012, "Computation of a Canadian SCWR Unit Cell with Deterministic and Monte Carlo Codes", PHYSOR 2012 conference, Knoxville, Tennessee, USA
[8] W. Shen, September 2006, "Development of a Multicell Methodology to Account for Heterogeneous Core Effects in the Core-Analysis Diffusion Code", PHYSOR 2006 conference, Vancouver, British Columbia, Canada
[9] M. Abramowitz, I.A. Stegun, 1972, "Handbook of Mathematical Functions: with Formulas, Graphs, and Mathematical Tables", Dover Publications, New York

FULL ARTICLE

SELF-EXCITED ACOUSTIC RESONANCE OF ISOLATED CYLINDERS IN CROSS-FLOW

A. Mohany*

University of Ontario Institute of Technology, Faculty of Engineering and Applied Science, Oshawa, Ontario, Canada, L1H 7K4

Article Info
Keywords: acoustic resonance, vortex shedding, single cylinder, two-tandem cylinders, two side-by-side cylinders.
Article history: Received 14 April 2012, Accepted 25 June 2012, Available online 30 June 2012.

*Corresponding Author: (613) 584-3311 ext. 5720, Atef.Mohany@uoit.ca

ABSTRACT

Self-excited acoustic resonance is a design concern in many engineering applications such as tube bundles of heat exchangers and boilers. Since this phenomenon is not yet fully understood, it can be dangerously unpredictable. Due to the complexity of the flow-sound interaction mechanisms in tube bundles, the simplified cases of a single cylinder and two cylinders in various arrangements, tandem and staggered, are investigated in some detail. A summary of these investigations is presented in the current paper. It is found that the aeroacoustic response of two-tandem and side-by-side cylinders in cross-flow can be considerably different from that of a single cylinder under similar flow conditions. Moreover, for the case of two tandem cylinders, the acoustic resonance is excited over two different ranges of flow velocity; the pre-coincidence and the coincidence resonance ranges. The pre-coincidence acoustic resonance phenomenon is found to be similar to the acoustic resonance mechanism of in-line tube bundles.

I. Introduction

The vortex-shedding phenomenon has been a subject of research since it was observed by Leonardo da Vinci. Vortex shedding occurs due to the boundary layer separation around bluff bodies in cross-flow. The boundary layer separates into two shear layers that trail and roll-up in the near field forming a periodic vortex street. In the case of a duct containing a bluff body such as a circular cylinder, when the vortex shedding frequency coincides with one of the acoustic natural frequencies of the duct, a feedback cycle may occur where the vortex shedding acts as a sound source and excites an acoustic standing wave which, in turn, enhances the shedding process and thereby creates a strong acoustic resonance. This process is known as flow-excited acoustic resonance.

While there has been a large amount of research on the flow around circular cylinder(s) because of its wide application in engineering practices, see for example Zdravkovich [1, 2], Igarashi [3, 4], Ljungkrona et al. [5], Lin et al. [6], Alam et al. [7] and Sumner [8, 9], the flow-excited acoustic resonance phenomenon has received considerably less attention. Better understanding of this excitation mechanism and the details of the coupling mechanism and the associated energy transfer between the flow field and the resonant sound field for the simple cases of a single, tandem, and side-by-side cylinders is necessary in order to explain the phenomenon of flow-excited acoustic resonance in more complex flow situations such as those existing in tube arrays. It would also help developing effective means to control and avoid the occurrence of acoustic resonances.

The flow patterns around two cylinders arranged close to one another in tandem, side-by-side, or staggered configuration, as shown in Figure 1, are very different from the case of a single cylinder in cross-flow due to the interference mechanism. This interference could create hydrodynamic forces that may enhance or suppress the vortex shedding process. Pressure measurements and flow visualization have often been used in the literature to identify the interference regions between two cylinders. Zdravkovich [1] reported that for the case of two tandem cylinders, there is no existence of vortex shedding behind the upstream cylinder for spacing ratios (L/D) less than 3.8, where L is the center to center distance between the cylinders and D is the cylinder diameter. Moreover, a "critical spacing" was introduced to specify the center-to-center spacing at which vortices start to form in the gap between the cylinders. The critical spacing (L/D) was found to be about 3.5, and it is slightly influenced by Reynolds number. For the case of two side-by-side cylinders with intermediate spacing ratios, $T/D < 2.2$, the wakes exhibit bi-stable flow. This is characterized by a wide-open wake behind one cylinder and a closed-narrow wake behind the other creating a biased jet between the two cylinders that can switch its biased direction to either of the two cylinders. However, for large spacing ratios, $T/D > 2.2$, the two side-by-side cylinders do not exhibit bi-stable flow properties.

Instead, the wakes appear more symmetric and will become dominated by vortex shedding at a single frequency.

The vortex-shedding could be altered by the excited acoustic standing wave, and a significant change to the flow pattern around the bluff body could take place. The acoustic standing wave forces the flow to oscillate around the bluff body. The effect of acoustic resonance on the vortex shedding process can be investigated by either oscillating the flow around a fixed body using an external sound field, or by oscillating the body itself. Both of these approaches provide controlled experiments to investigate the flow-acoustic coupling process, and may explain the changes in the flow patterns and the exerted hydrodynamic forces on the cylinders due to the applied sound. But it is rather difficult to understand the mechanism of energy transfer between the flow field and the sound field unless the self-excited resonance case is investigated.

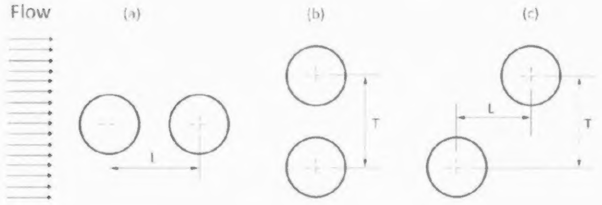

FIGURE 1
Two cylinders arranged in (a) tandem; (b) side-by-side; and (c) staggered.

Blevins studied the effect of sound on vortex shedding from a single cylinder [10]. His experiments were performed in a wind tunnel with and without externally applied sound field at Reynolds numbers up to 8.5×10^4. The acoustic standing wave was excited across the test section using two electromagnetic speakers. It was observed that the sound field could correlate the vortex shedding in the span-wise direction, which makes the shedding process more intense. Blevins measured the coherence between a flush-film and a movable probe along the cylinder span with and without externally applied sound [10]. He observed that for the case of externally applied sound, the vortex shedding is two-dimensional and the turbulence intensity in the approach flow does not have any effect on the coherent structure of the vortex shedding. Moreover, by applying sound field at the acoustic resonance frequency of the duct "first cross mode", the broadness of the vortex-shedding peak was reduced as the amplitude of the sound wave was increased. The broad vortex shedding peak was replaced by a sharp peak at the sound frequency when the sound pressure amplitude was increased to 250 Pa. Blevins investigated this entrainment process by placing the cylinder at different locations in the transverse direction [10]. He concluded that it is the acoustic particle velocity, not the acoustic pressure that causes the entrainment process.

In the case of oscillating bluff body, whether the oscillations are self-induced or externally imposed, the lock-in condition can be achieved if the oscillating frequency in the transverse direction is close to the vortex shedding frequency. Lock-in can also be achieved if the oscillating frequency in the stream-wise direction is close to twice the vortex-shedding frequency [11]. The lock-in condition in the forced oscillation has some similarities with the case of acoustic resonance. One of the early investigations of the wake structure behind a vibrating circular cylinder was performed by Koopmann [12]. The experiments were conducted in a low turbulence wind tunnel at Reynolds number ranges of 100, 200 and 300. For the case of a stationary cylinder, three-dimensional pattern of the vortex shedding was observed. However, when the cylinder vibrates at a frequency equal or close to that of the natural vortex shedding process, the wake structure behind the cylinder becomes two dimensional, i.e., the vortices along the cylinder span are correlated (shed in-phase) and the vortex filaments are shedding parallel to the cylinder. Moreover, during this two-dimensional shedding, the upstream turbulence did not have any effect on the wake structure. This observation is similar to that observed by Blevins [10] for the case of externally applied sound. Koopmann [12] examined also the conditions for which the vortex shedding frequency was locked-in to the oscillation frequency of the cylinder. He observed that when the cylinder oscillates with a frequency equal to that of the vortex shedding, a minimum oscillation amplitude of about 10% of the cylinder diameter is required to initiate the lock-in mechanism. Nevertheless, the upper and lower ranges of oscillation frequencies for the lock-in region, around ±25% of the vortex shedding frequency, depend on the oscillation amplitudes and to some extent depend also on Reynolds number. Moreover, Koopmann [12] observed that when the cylinder oscillates at the upper frequency limit, the longitudinal spacing between the vortex filaments decreases, and when the cylinder oscillates at the lower frequency limit, the longitudinal spacing between the vortex filaments increases.

Griffin & Ramberg [13] conducted experiments in an open-jet wind tunnel at Reynolds numbers of 144 and 190 to investigate the effect of cylinder vibration on the wake structure of vortex shedding. Velocity measurements in the near field and flow visualization were performed. They found that by increasing the oscillation amplitude of the cylinder, the length of vortex formation decreases. Moreover, the lateral vortex spacing is inversely proportional to the oscillation amplitude, whereas the longitudinal vortex spacing is inversely proportional to the oscillation frequency, which is similar to that observed by Koopmann [12].

Bishop and Hassan [14] investigated the effect of forced oscillation on the hydrodynamic forces, including lift and drag forces, exerted on a single cylinder. Their experiments were performed in a water tunnel with a Reynolds number in the range of 5×10^3 to 10×10^3. The investigation focused on measurements of both the amplitude and the phase angle of the hydrodynamic forces with respect to the cylinder displacement. The phase angle is important because it influences the mechanism of energy transfer between the flow field and the cylinder oscillation, which will be discussed in some details later on. Bishop and Hassan [14] found a remarkable sudden change in both the phase and amplitude of the hydrodynamic forces at the frequency coincidence.

Many years later, Zdravkovich [15] examined the flow visualizations of previous studies and he noted that for a reduced velocity smaller than that at the frequency coincidence, the vortex formed on one side of the cylinder is shed just before the cylinder reaches the position of the maximum amplitude on the opposite side. For a reduced velocity larger than that at the frequency coincidence, the vortex with the same circulation as before is shed when the cylinder reaches the position of the maximum amplitude on the same side. Therefore, Zdravkovich [15] explained this phase jump as a lack in the synchronization between the cylinder oscillation and the "newly shed vortices".

For the case of self-excited acoustic resonance, Blevins and Bressler [16] have performed experiments on the acoustic resonance in heat exchanger tube bundles. The first phase of their experiments focused on the aeroacoustic response of a single cylinder in cross-flow under resonance conditions, and the second phase investigated the aeroacoustic response of different tube array configurations. The main objective of these experiments was to develop a model that can be used to predict the resonant sound pressure level for a single and multiple cylinders in cross flows.

From the previous investigations, it is clear that a crucial event in the mechanism of acoustic resonance is the ability of sound to modulate, and essentially "lock-in", the process of vortex shedding. While this phenomenon is relatively well understood for the case of a single cylinder there are many unresolved issues for the more complex case of multiple cylinders in close proximity. In the present paper, a summary of a research program that was conducted on the flow-sound interaction mechanism of multiple bluff bodies in cross-flow is presented. Both experimental and numerical results are outlined in the paper.

2. Experimental Set-up

The experiments were performed in an open loop wind tunnel. The test section was made of 25.4 mm thick clear acrylic walls, to facilitate a flow-visualization study in the future, and had a cross-section of 76.2 mm in width by 254 mm in height. These dimensions were carefully selected to ensure coincidence between the first acoustic resonance frequency (f_a = 688 Hz) and the frequency of vortex shedding from single, tandem, and side-by side cylinders.

Several cylinders with different diameters were used. The largest diameter produced a maximum wind tunnel blockage ratio of about 10%. The cylinders were made of aluminum and were rigidly mounted on the test section sidewall to eliminate the effect of cylinder vibration on the flow-sound interaction mechanism. Two windows attached to the sidewalls were used to provide flexibility in setting up different cylinder diameters, different arrangements and different spacing ratios.

The flow velocity inside the test section was calibrated by means of a pitot tube and a pressure transducer. The fluctuating pressure on the top wall of the duct was measured by means of a 1/4" condenser microphone, which was flush-mounted on the test section wall at the location of the maximum acoustic pressure. A Hewlett-Packard analyzer was used for spectral analysis. Each spectrum was obtained by averaging 100 samples. Data was collected at a sampling rate of 4100 Hz. More details about the experimental set-up and instrumentation can be found in Mohany and Ziada [17].

3. Aeroacoustic Response of a Single Cylinder

Figure 2(a) shows a typical pressure spectrum for a 19 mm single cylinder in cross-flow, and Figure 2(b) shows a waterfall plot of pressure spectra for the same cylinder. At off-resonance conditions, two frequency components can be observed in Figure 2(a), the lower component is the vortex shedding frequency, while the higher component near 688 Hz is the first acoustic mode of the duct housing the cylinder. As the flow velocity is increased, the frequency of the vortex shedding component and its amplitude are increased until the vortex shedding frequency becomes close to that of the acoustic mode, where the lock-in phenomenon is initiated and an intense acoustic resonance is produced, as shown in Figure 2(b). The recorded maximum sound pressure level for this case is 155.6 dB. As can be seen in Figure 2(b), during the lock-in range, high frequency components are also generated. These components are not the higher acoustic modes ($f(2\lambda/2)$, $f(3\lambda/2)$, $f(4\lambda/2)$,...) but rather the higher harmonics of the first acoustic mode ($2f(\lambda/2)$, $3f(\lambda/2)$, $4f(\lambda/2)$,...). These higher harmonics are generated by nonlinear effects due to the very high acoustic pressure at resonance. Figure 3 is constructed from Figure 2(b), and depicts the frequency and the amplitude of the vortex shedding component in pressure spectra as functions of the reduced velocity. Similar response was obtained for a 25.4 mm single cylinder in cross-flow as shown in Figure 4. The lock-in region for this case is wider and the maximum acoustic pressure at resonance is much higher than those observed for all other tested cases of single cylinders. The reduced velocity U_r presented in all figures is based on the frequency of the lowest cross-mode of the test section, f_a, as illustrated in equation 1;

$$U_r = \frac{U}{f_a \times D} \qquad (1)$$

It is clear from Figures 3 and 4 that within a certain range of Reynolds number, the Strouhal number for a single cylinder is about 0.2. If acoustic resonance is initiated at a constant Strouhal number, given by equation 2, increasing the diameter will also increase the critical flow velocity U for the onset of resonance.

$$St = \frac{f_a \times D}{U} \qquad (2)$$

This feature is illustrated in Figure 5, which shows the vortex shedding frequency and the lock-in range for four single cylinders with different diameters, D = 0.5", 0.625", 0.75", and 1". It is clear from this figure that increasing the cylinder diameter will result in higher critical flow velocity and dynamic head at the onset of resonance. The flow excitation energy at the resonance conditions will therefore be higher for larger diameter cylinders.

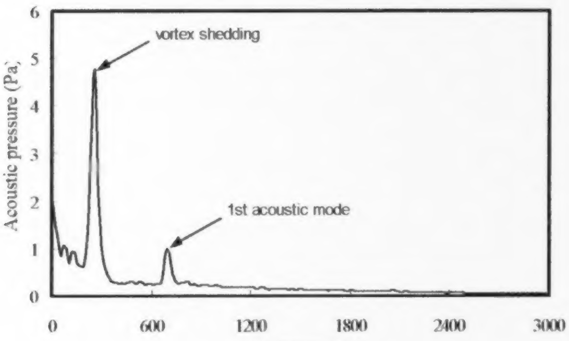

FIGURE 2(A)
Pressure spectrum measured on the top wall of the test section for a single cylinder with D = 19 mm at a flow velocity of 25 m/s [17].

A numerical simulation of the flow-excited acoustic resonance is performed to reveal the details of flow-sound interaction mechanisms, including the nature and the locations of the aeroacoustic sources in the flow field. A deep understanding of the flow-sound interaction mechanism and the resulting energy transfer between the flow and the resonant sound fields would improve our ability to alleviate and control the occurrence of acoustic resonance. This can be achieved by identifying the location of the aeroacoustic sources in the flow field and developing suitable means to mitigate the energy transfer mechanism [18]. In this simulation, the flow field and the sound field are simulated

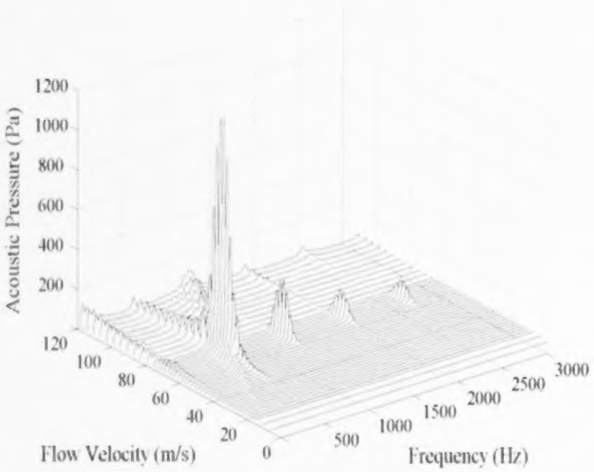

FIGURE 2(B)
Pressure spectra measured on the top wall. Single cylinder tests; D = 19 mm [17].

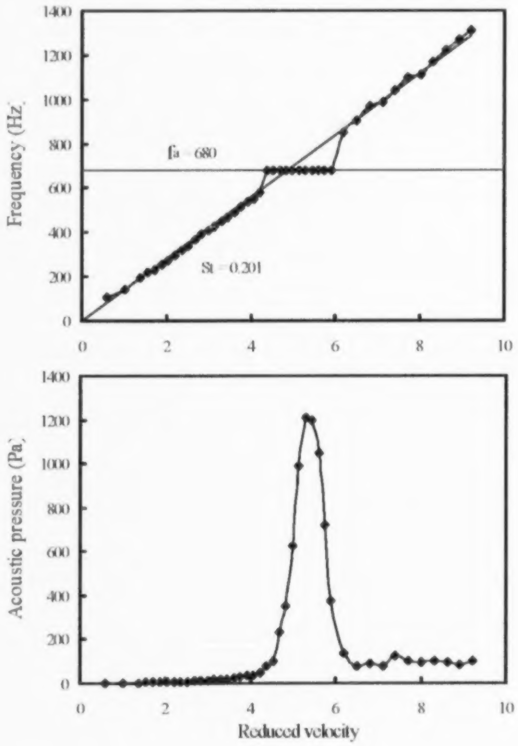

FIGURE 3
Frequency and amplitude of pressure fluctuation on the test section top wall at the frequency of vortex shedding. Single cylinder tests; D = 19 mm [17].

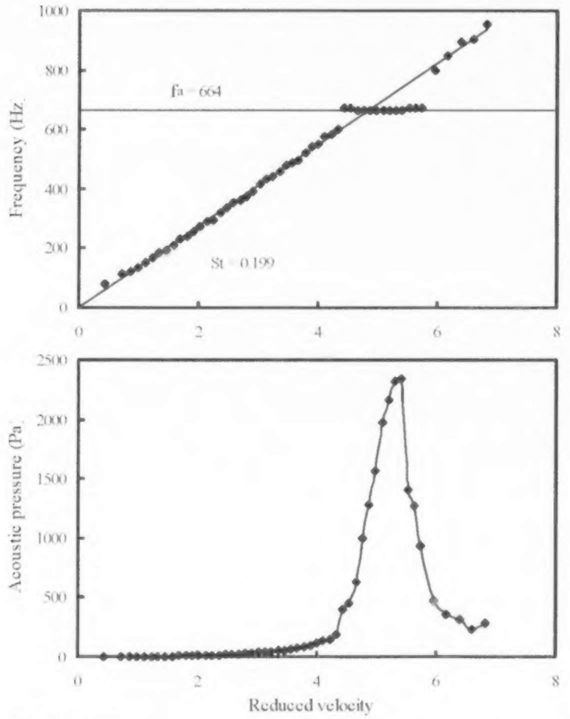

FIGURE 4
Frequency and amplitude of pressure fluctuation on the test section top wall at the frequency of vortex shedding. Single cylinder tests; D = 25.4 mm.

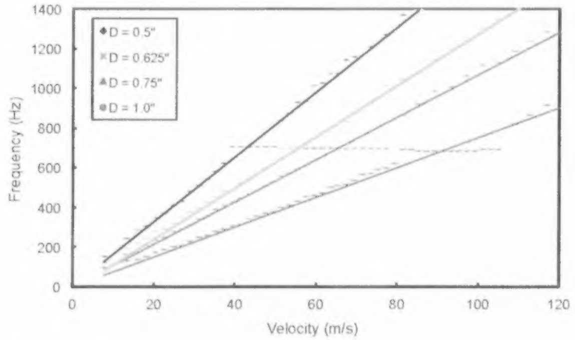

FIGURE 5
Aeroacoustic response of a single cylinder in cross-flow.

separately (i.e., uncoupled). In order to simulate the coupling phenomenon, the simulation of the unsteady flow field was repeated with applying an oscillatory cross-flow velocity perturbation, which simulates the acoustic particle velocity of the resonant sound field. The acoustic sources (or sinks) in the flow field are then predicted by combining the solution of the acoustic field, which is modeled by the finite-element method using ABAQUS, with the acoustically coupled unsteady flow field, which is modeled using the Spalart-Allmaras (S-A) turbulent model in FLUENT to predict the vorticity distribution in the cylinder wake. Howe's theory of aerodynamic sound [19, 20], equation 3, is then used to calculate the instantaneous acoustic power generated by the convection of the unsteady vorticity field within the sound field. The net acoustic energy is the integration of the instantaneous acoustic power over a complete acoustic cycle. Therefore, the locations within the flow field where the acoustic energy is either absorbed or generated can be identified. Details of the numerical simulation can be found in [21].

$$\Pi = -\rho \int \vec{\omega} \cdot (\vec{u} \times \vec{v}) d\forall \qquad (3)$$

Where Π is the instantaneous acoustic power, $\vec{\omega}$ is the vorticity, $\vec{u}$ is flow velocity, and $\vec{v}$ is acoustic particle velocity. As mentioned earlier, to account for the effect of the resonant sound on modifying the flow around the cylinder, a cross-flow oscillation was applied at the top and the bottom boundaries as well as at the inlet to mimic the acoustic resonance of the first cross mode. The amplitude and the frequency of the cross-flow perturbation were changed independently to examine the sensitivity of the flow to this perturbation and also to determine the minimum amplitude at which the lock-in occurs. Figure 6 shows the dependence of the lock-in on the amplitude and frequency of the cross-flow oscillation for the case of a single cylinder in cross-flow. It is found that the minimum perturbation amplitude at which the lock-in occurs was 2.5% of the main flow velocity. This minimum amplitude was obtained near the condition of frequency coincidence, i.e., when the excitation frequency, f_a, approximated the natural vortex shedding frequency, f_v, ($0.975 < f_a/f_v < 1.025$). As the excitation frequency deviated from the vortex shedding frequency, the minimum amplitude required to lock-in the shedding frequency increased as shown in Figure 6. The lock-in region obtained from the simulation is indicated by the broken line in Figure 6.

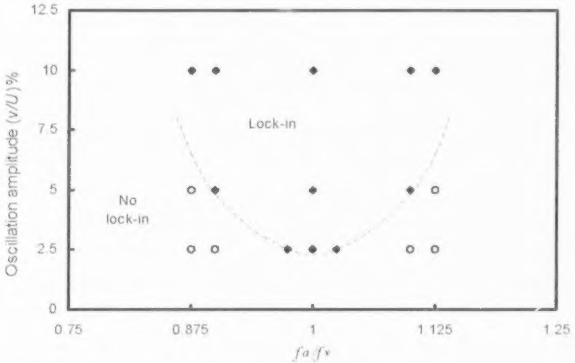

FIGURE 6
Dependence of the lock-in on the amplitude and frequency of the cross-flow oscillation for the case of a single cylinder. ◆, Lock-in; ○, No lock-in [21].

Figure 7 shows the total acoustic energy over one cycle. The red colour in these figures represents net positive energy and the blue colour represents net negative energy. The total energy transfer per cycle for different downstream locations is shown in Figure 8. For each streamwise location, the total energy represents the energy integrated over a rectangular area with a height extending along y = ± 10 D and a small width of $\triangle x$ centered at the streamwise location x. As can be seen from this figure, the total energy transfer just downstream of the cylinder is positive and is larger than that occurring in the downstream region, which means that there is a strong acoustic source located there, resulting in a net positive energy transfer from the flow field to the sound field.

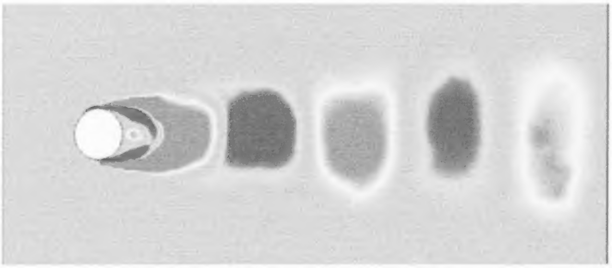

FIGURE 7
Total acoustic energy over one cycle. $f_a/f_v = 1$. [21].

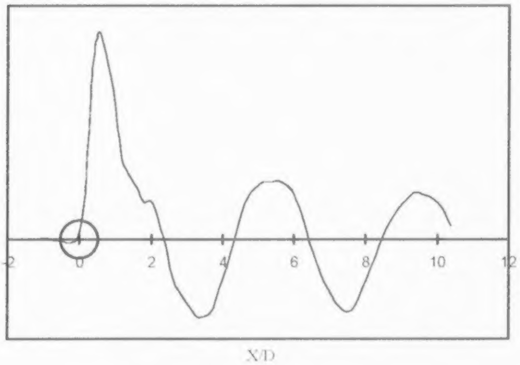

FIGURE 8
Total energy transfer per cycle at different downstream locations. Mohany and Ziada [21].

4. Aeroacoustic Response of Two Tandem Cylinders

The aeroacoustic response for the case of two tandem cylinders in cross-flow with spacing ratios within the proximity interference region, L/D < 3.5, is considerably different from that of a single cylinder in cross-flow. Figure 9 represents the frequency and the amplitude of the vortex shedding component in pressure spectra as functions of the reduced velocity for two tandem cylinders with spacing ratio, L/D = 2. It is clear from Figure 9 that the acoustic resonance of the first mode occurs over two different ranges of flow velocity. The first resonance range occurs before the velocity of frequency coincidence and is called the pre-coincidence acoustic resonance, while the second resonance range occurs at the velocity of frequency coincidence and is called the coincidence acoustic resonance. More details about these resonance ranges can be found in references [17, 22].

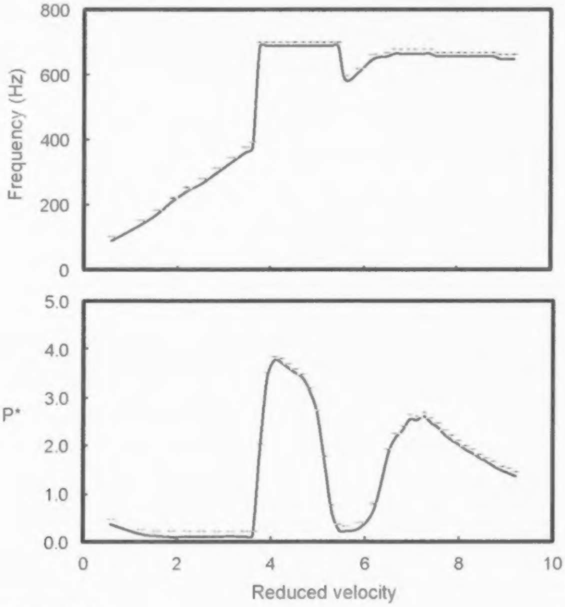

FIGURE 9
Aeroacoustic response of two tandem cylinders with L/D = 2; D = 25.4 mm.

It should be noted here that the acoustic pressure, P_{rms}, in Figure 9 is normalized by the dynamic head, $\frac{1}{2}\rho U^2$, and the Mach number, M, as shown in equation 4;

$$P^* = \frac{P_{rms}}{\frac{1}{2}\rho U^2 M} \tag{4}$$

This normalization procedure has been suggested by Blevins [23] and has been used by Mohany and Ziada [17] to properly account for the main parameters influencing the sound pressure level of acoustic resonances excited by vortex shedding from single cylinders. As the spacing ratio between the tandem cylinders is increased beyond 3.5, the flow pattern changes to that corresponding to the wake interference regime. The aeroacoustic response at these large spacing ratios is found to be similar to that of a single cylinder. A typical example for L/D = 4.5 is shown in Figure 10. It is also observed that as the spacing ratio is increased, the

Strouhal number increases towards 0.2 and the amplitude of the maximum acoustic pressure decreases, which indicates a transition to the single cylinder features.

A comparison between the pre-coincidence acoustic resonance and the acoustic resonance mechanism of in-line tube bundles shows interesting similarity. The acoustic resonance of in-line tube bundles normally starts and subsides before the flow velocity reaches that corresponding to the frequency coincidence conditions. This similarity is highlighted in Figure 11, which compares the acoustic response of tandem cylinders with that of in-line tube bundles with nearly equal streamwise tube spacing ratio. The Strouhal number of vortex shedding for the in-line tube bundles is seen to be similar to that for the case of two tandem cylinders. Moreover, the acoustic resonance for in-line tube bundles and the pre-coincidence resonance of tandem cylinders are seen to be initiated at the same reduced velocity. With respect to the resonance intensity, it is clearly stronger for tube bundles because they have lower radiation losses and larger number of acoustic sources than in the case of two tandem cylinders.

As discussed in Mohany and Ziada [22], the pre-coincidence acoustic resonance of two tandem cylinders with spacing ratios within the proximity interference region is only observed when the cylinder diameter exceeds a certain value. However, for two tandem cylinders with small cylinder diameter, the first acoustic mode is excited over a single range of flow velocity, which is similar to the resonance mechanism of a single cylinder in cross-flow. Figure 12 shows a typical response of two tandem cylinders with a spacing ratio of L/D = 2.5, which is the same spacing ratio as that of Figure 11 but for smaller cylinder diameter, D = 7.6 mm. Figure 13 summarizes the results of the aeroacoustic response for the case of two tandem cylinders in cross-flow with different spacing ratios and cylinder diameters. The solid data points correspond to the cases when the pre-coincidence resonance is excited. It is clear from Figure 13 that as the spacing ratio increases, the flow energy required to excite the pre-coincidence acoustic resonance decreases, which means that the pre-coincidence resonance is easier to excite for large spacing ratios with smaller diameter cylinders in comparison with that for small spacing ratios.

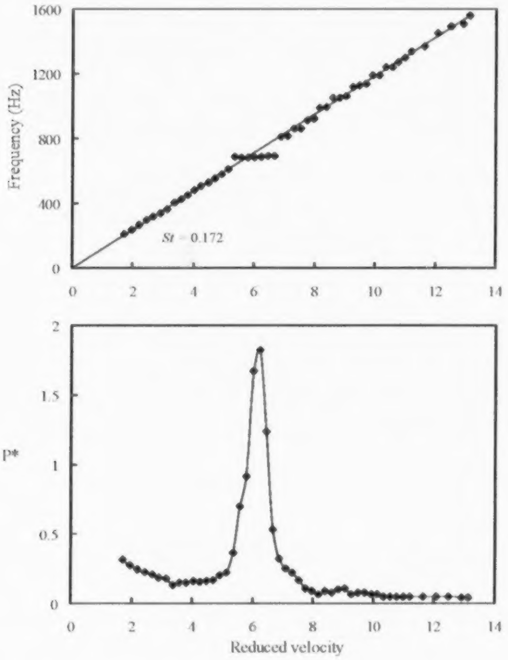

FIGURE 10
Aeroacoustic response of two tandem cylinders. L/D = 4.5; D = 12.7mm, Mohany and Ziada [17].

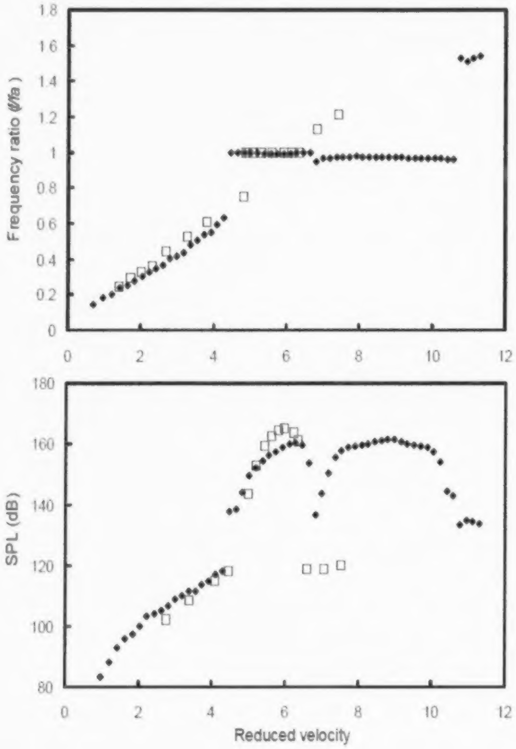

FIGURE 11
Comparison between the acoustic response of two tandem cylinders with that of in-line tube bundles. •, two tandem cylinders with L/D = 2.5; □, in-line tube bundles with X_L = 2.6 and X_T = 3.0 [22].

Mohany and Ziada [21] conducted a numerical simulation of the flow-excited acoustic resonance for the case of two tandem cylinders in cross-flow. The wake structure behind the tandem cylinders before applying the cross-flow oscillation is shown in Figure 14. The wake structure around

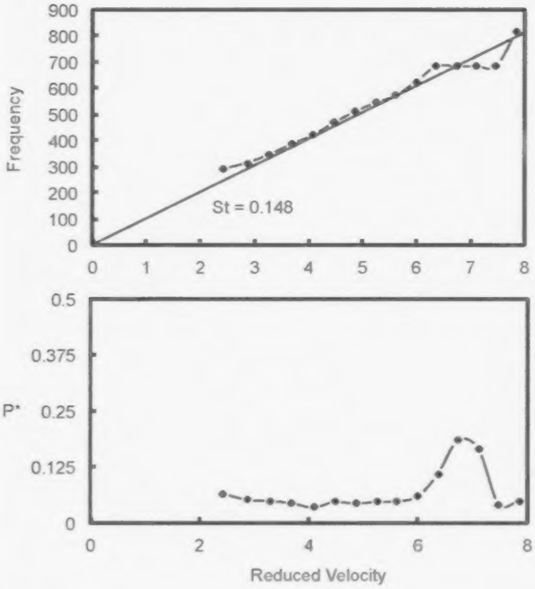

FIGURE 12
Aeroacoustic response of two tandem cylinders with L/D = 2.5; D = 7.6 mm, Mohany and Ziada [22].

the tandem cylinders after applying the cross-flow oscillation at a frequency ratio of 1.2, which corresponds to the pre-coincidence acoustic resonance range, is shown in Figure 15. A comparison between Figures 15 and 14 shows that for the pre-coincidence acoustic resonance, the wavelength of the wake structure is smaller than that before applying the cross-flow oscillation. This is because the wake for this case is locked into an oscillation frequency which is higher than the vortex shedding frequency, $f_a = 1.2\ f_v$.

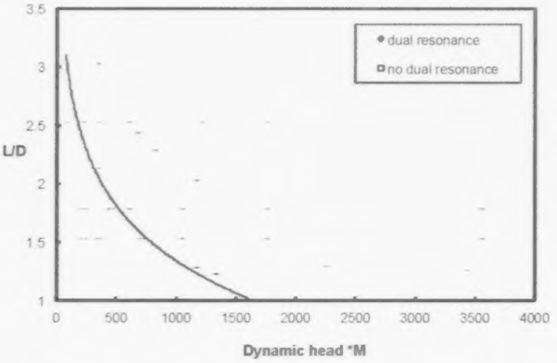

FIGURE 13
Dependence of the pre-coincidence acoustic resonance on the spacing ratio and the flow excitation energy.

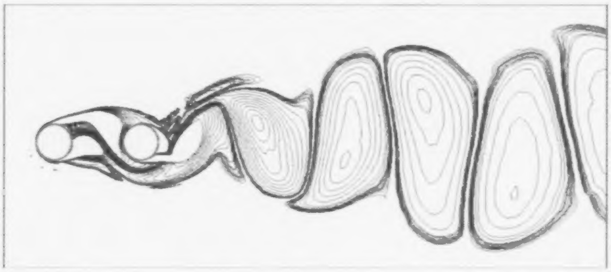

FIGURE 14
Vorticity contours behind two tandem cylinders, L/D = 2.5, at Re = 25000 before applying the cross-flow oscillation.

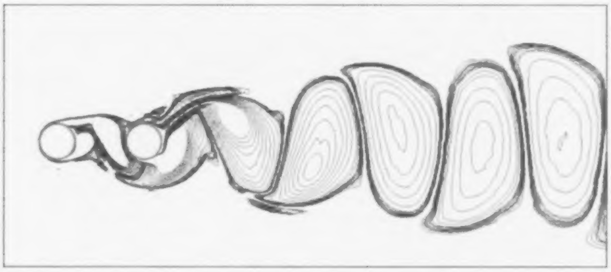

FIGURE 15
Vorticity contours behind two tandem cylinders, L/D = 2.5, at Re = 25000, pre-coincidence acoustic resonance, $f_a = 1.2\ f_v$.

Figure 16 represents the total acoustic energy over one cycle during the pre-coincidence acoustic resonance for L/D = 2.5 and Figure 17 is the distribution of the total energy transfer at different downstream locations. It is clear from Figures 16 and 17 that during the pre-coincidence acoustic resonance a strong acoustic source in the flow field is located in the gap between the cylinders. Moreover, the energy transfer from the flow field to the sound field associated with this acoustic source is dominant. Based on extensive measurements of the dynamic lift force acting on the tandem cylinders and its phase with respect to the resonant sound field in combination with flow visualization, Mohany and Ziada [24] suggested that the pre-coincidence acoustic resonance is caused by the instability of the separated shear layers in the gap between the cylinders.

5. Aeroacoustic Response of Two Side-by-Side Cylinders

For two side-by-side cylinders with small and intermediate spacing ratios, T/D < 2.2, the wakes exhibit bi-stable flow features as those reported in the literature [25, 26, 27]. Two Strouhal numbers of vortex shedding are observed before the onset of acoustic resonance. However,

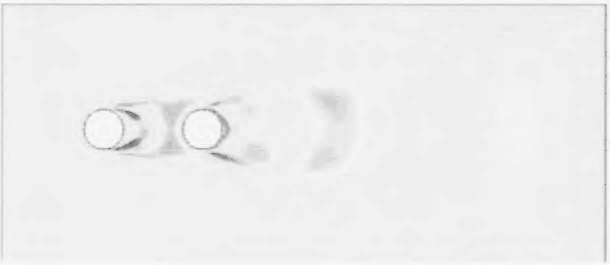

FIGURE 16
Total acoustic energy over one cycle for two tandem cylinders at conditions simulating the pre-coincidence acoustic resonance. L/D = 2.5; Re = 25000; f_a/f_v = 1.2 [21].

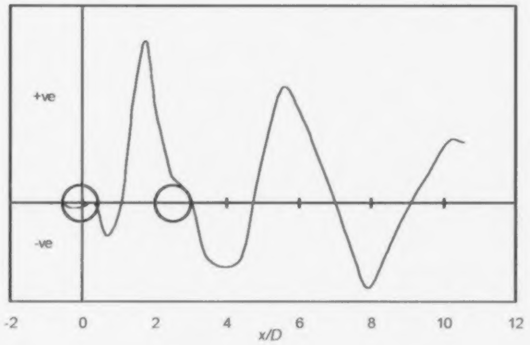

FIGURE 17
Total energy transfer per cycle for different downstream locations. Two tandem cylinders at conditions simulating the pre-coincidence acoustic resonance. L/D = 2.5; Re = 25000; f_a/f_v = 1.2 [21].

during the experiments, self-excited acoustic resonance occurred at an intermediate Strouhal number which lies between those corresponding to the bi-stable flow regimes. Figure 18 represents the aeroacoustic response of two side-by-side cylinders in cross-flow with spacing ratio of T/D = 1.25. In this case, two vortex shedding frequencies are distinguished at the off resonance conditions, which are generated by the narrow and wide wakes behind the cylinders. The two Strouhal numbers observed in this case are 0.12 and 0.36, as indicated by the straight lines in Figure 18. It is seen that the lock-in range does not correspond to either of these Strouhal numbers. Interestingly, after the lock-in resonance subsides near U_r = 5.6, the low frequency component of vortex shedding is recovered and its frequency is still lower than the acoustic resonance frequency. Parker and Stoneman [28] describe this behaviour as "locking up" for resonance that occurs above a natural frequency, which has occurred in this situation. From the presented data, it appears that the resonant sound field synchronizes the vortex shedding process and thereby eliminates the bi-stable flow phenomenon. Vortex shedding in this case must occur at an intermediate frequency between the two frequency components associated with the bi-stable flow.

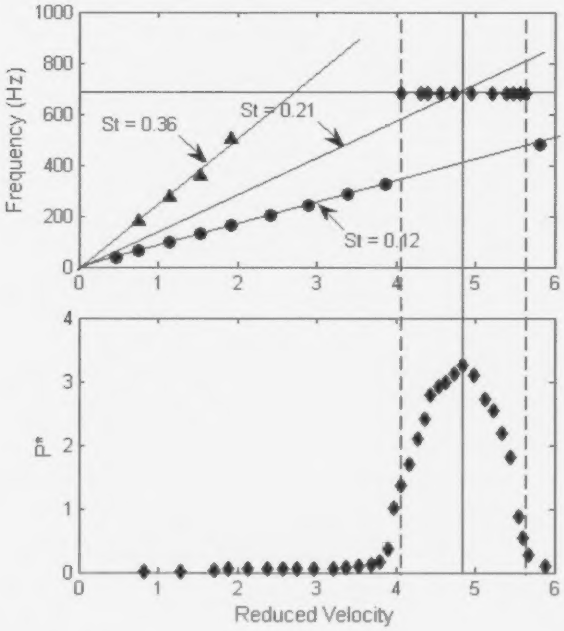

FIGURE 18
Aeroacoustic response of two side-by-side cylinders with T/D = 1.25 and D = 21.8 mm. •, lower vortex shedding frequency; ▲, higher vortex shedding frequency; ◆, first resonance mode frequency, Hanson et al. (2009).

To confirm this supposition, a numerical simulation of the flow-sound interaction mechanism for this case was performed. Figure 19 shows the wake structure behind the two cylinders with spacing ratio of T/D = 1.25 at the off resonance condition, which shows clearly the bi-stable flow regimes. The wake structure behind the cylinders after applying the cross-flow perturbation, which mimic the excitation of acoustic resonance, is shown in Figure 20. A comparison between Figures 19 and 20, shows that after applying the cross-flow perturbation, the flow in the wakes of the cylinders is synchronized and thereby the bi-stable biased flow is eliminated. More details can be found in Mohany et al. [30].

The aeroacoustic response of two side-by-side cylinders with large spacing ratios, T/D > 2.2, exhibits a single vortex shedding frequency of about 0.22, which agrees well with the values reported in the literature. The acoustic

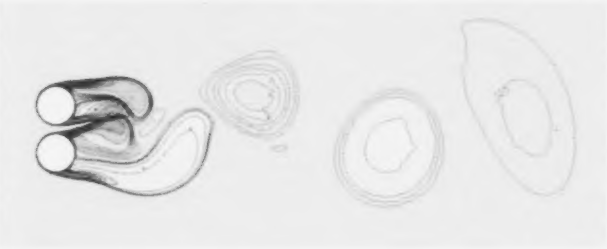

FIGURE 19
Vorticity contours behind two side-by-side cylinders, T/D = 1.25, at Re = 25000, no acoustic excitation.

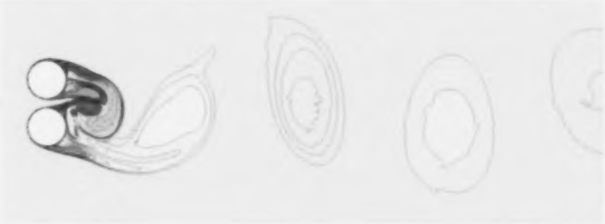

FIGURE 20
Vorticity contours behind two side-by-side cylinders, T/D = 1.25, at Re = 25000, with acoustic excitation.

resonance is excited by the vortex shedding observed before the onset of resonance. This behavior is clear in Figure 21, which represents the aeroacoustic response of two side-by-side cylinders in cross-flow with spacing ratio of T/D = 2.5. A numerical simulation is performed for this case and the wake structure behind the cylinders at the off resonance conditions is shown in Figure 22. It is clear from this figure that a symmetric wake structure behind the cylinders with one vortex shedding frequency, which is similar to that of a single cylinder in cross-flow, is formed.

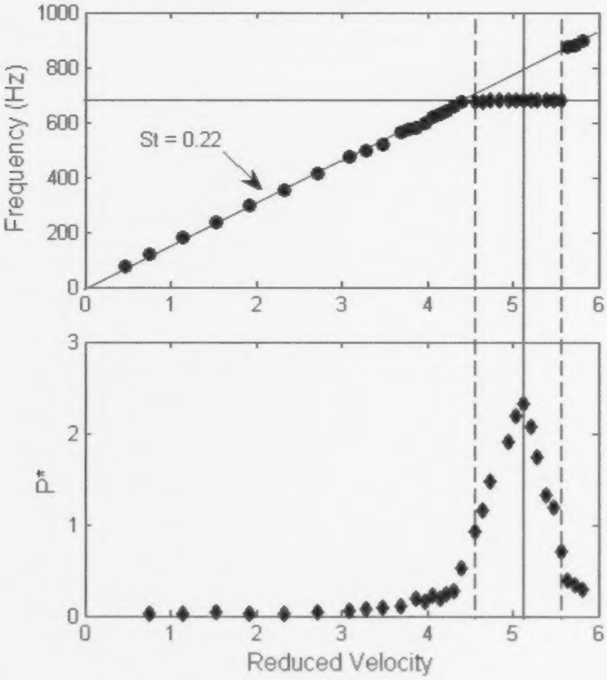

FIGURE 21
The aeroacoustic response of the two side-by-side cylinders with T/D = 2.5 and D = 21.8 mm. •, vortex shedding frequency; ♦, first resonance mode frequency [29].

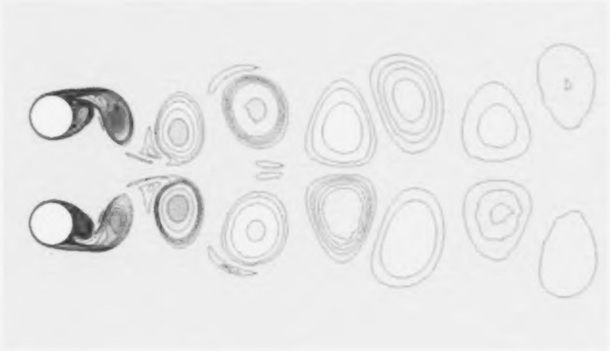

FIGURE 22
Vorticity contours behind two side-by-side cylinders, T/D = 2.5, at Re = 25000, no acoustic excitation.

6. Conclusion

A summary of a research program on the acoustic resonance mechanism of single, two tandem, and two side-by-side cylinders is presented in this paper. The aeroacoustic response of a single cylinder is similar to that reported in the literature. Acoustic resonance is excited by the natural vortex shedding observed before the onset of resonance. The Strouhal number of vortex shedding is 0.2 ± 0.005. As the diameter for the single cylinder is increased, the required flow velocity to excite the acoustic resonance increases, which results in a stronger acoustic resonance and a wider lock-in range of flow velocity. The acoustic resonance of the tandem cylinders within the proximity interference region occurs over two different velocity ranges. The one occurring at higher reduced velocities, the coincidence resonance range, is excited by the natural vortex shedding process, as in the single cylinder case. The other range, the pre-coincidence resonance range, is initiated at a much lower reduced velocity, and appears to be excited by the shear layers that form in the gap between the two cylinders. Moreover, a comparison between the pre-coincidence acoustic resonance and the acoustic resonance mechanism of in-line tube bundles shows interesting similarity. For two side-by-side cylinders with small and intermediate spacing ratios, i.e., $T/D < 2.2$, the flow is shown to exhibit a bi-stable behaviour at the off resonance conditions. Acoustic resonance for this case is excited at an intermediate Strouhal number, which lies between those corresponding to the bi-stable flow regimes. However, for two side-by-side cylinders with large spacing ratios, $T/D > 2.2$, the flow at the off resonance conditions is symmetric and exhibit a single vortex shedding frequency. The acoustic resonance for this case is excited by the vortex shedding observed before the onset of resonance.

REFERENCES

[1] M.M. Zdravkovich, 1977, "Review of Flow Interference Between Two Circular Cylinders in Various Arrangements". Transactions of the ASME, Journal of Fluids Engineering, 99(4), pp. 618-633.
[2] M.M. Zdravkovich, 1985, "Flow Induced Oscillations of Two Interfering Circular Cylinders". Journal of Sound and Vibration, 101(4), pp. 511-521
[3] T. Igarashi, 1981, "Characteristics of the Flow Around Two Circular Cylinders Arranged in Tandem - 1st report". Bulletin of the Japan Society of Mechanical Engineers (JSME), 24(188), pp. 323-331
[4] T. Igarashi, 1984, "Characteristics of the Flow Around Two Circular Cylinders Arranged in Tandem: 2nd Report", Unique phenomenon at small spacing. Bulletin of the Japan Society of Mechanical Engineers (JSME), 27(233), pp. 2380-2387
[5] L. Ljungkrona, Ch. Norberg, and B. Sunden, 1991, "Free-Stream Turbulence and Tube Spacing Effects on Surface Pressure Fluctuations for Two Tubes in an In-Line Arrangement". Journal of Fluids and Structures, 5(6), pp.701-727
[6] J.-C. Lin, Y. Yang, and D. Rockwell, 2002, "Flow Past Two Cylinders in Tandem: Instantaneous and Averaged Flow Structure". Journal of Fluids and Structures, 16(8), pp. 1059-1071
[7] Md.M. Alam, M. Moriya, K. Takai, and H. Sakamoto, 2003, "Fluctuating Fluid Forces Acting on Two Circular Cylinders in a Tandem Arrangement at a Subcritical Reynolds Number". Journal of Wind Engineering and Industrial Aerodynamics 91(1-2), pp. 139-154
[8] D. Sumner, M.D. Richards, and O.O. Akosile, 2008, "Strouhal Number Data for Two Staggered Circular Cylinders". Journal of Wind Engineering and Industrial Aerodynamics 96(6-7), pp. 859-871
[9] D. Sumner, 2010, "Two Circular Cylinders in Cross-flow: A Review". Journal of Fluids and Structures 26(6), pp. 849-899
[10] R.D. Blevins, 1985, "The Effect of Sound on Vortex Shedding from Cylinders". Journal of Fluid Mechanics, 161, pp. 217-237.
[11] P. Anagnostopoulos, 2002, "Flow-Induced Vibrations in Engineering Practice", WIT Press
[12] G.H. Koopmann, 1967, The Vortex Wakes of Vibrating Cylinders at Low Reynolds Numbers. Journal of Fluid Mechanics, 28(3), pp. 501-512
[13] O.M. Griffin, and S.E. Ramberg, 1974, "The Vortex-street Wakes of Vibrating Cylinders". Journal of Fluid Mechanics, 66(3), pp. 553-576
[14] R.E.D. Bishop, and A.Y. Hassan, 1964, "The Lift and Drag Forces on a Circular Cylinder Oscillating in a Flowing Fluid". Proceedings of the Royal Society of London, Series A, 277(1368), pp. 51-75
[15] M.M. Zdravkovich, 1982, "Modification of Vortex Shedding in the Synchronization Range", Transactions of the ASME, Journal of Fluids Engineering, 104(4), pp.513-517
[16] R.D. Blevins and M.M Bressler, 1993, "Experiments on Acoustic Resonance in Heat Exchanger Tube Bundles". Journal of Sound and Vibration, 164(3), pp. 503-533.
[17] A. Mohany, and S. Ziada, 2005, "Flow-excited Acoustic Resonance of Two Tandem Cylinders in Cross-flow". Journal of Fluids and Structures, 21(1), pp. 103-119
[18] S.A.T. Stoneman, K. Hourigan, A.N. Stokes, and M.C. Welsh, 1988, "Resonant Sound Caused by Flow Past Two Plates in Tandem in a Duct", Journal of Fluid Mechanics, 192, pp. 455-484
[19] M.S. Howe, 1975, "Contributions to the Theory of Aerodynamic Sound, with Application to Excess Jet Noise and the Theory of the Flute". Journal of Fluid Mechanics, 71(4), pp. 625-673
[20] M.S. Howe, 1984, "On the Absorption of Sound by Turbulence and Other Hydrodynamic Flows". IMA Journal of Applied Mathematics, 32(1-3), pp. 187-209
[21] A. Mohany, and S. Ziada, 2009, "Numerical Simulation of the Flow-Sound Interaction Mechanisms of a Single and Two-Tandem Cylinders in Cross-Flow". Journal of Pressure Vessel Technology, 131(3), p. 031306
[22] A. Mohany, and S. Ziada, 2009, "A Parametric Study of the Resonance Mechanism of Two Tandem Cylinders in Cross-flow". Journal of Pressure Vessel Technology, 131(2), p. 021302
[23] R.D. Blevins, 1990, "Flow-Induced Vibration", 2nd ed., Van Nostrand Reinhold, New York.
[24] A. Mohany, and S. Ziada, 2009, "Effect of Acoustic Resonance on the Dynamic Lift Forces Acting on Two Tandem Cylinders in Cross-flow". Journal of Fluids and Structures, 25(3), pp. 461-478.
[25] P.W. Bearman, and A.J. Wadcock, 1973, "The interaction Between a Pair of Circular Cylinders Normal to a Stream". Journal of Fluid Mechanics, 61(3), pp. 499-511
[26] H.J. Kim, and P.A. Durbin, 1988, "Investigation of the Flow Between a Pair of Circular Cylinders in the Flopping Regime". Journal of Fluid Mechanics, 196, pp. 431-448.
[27] D. Sumner, S.S.T. Wong, S.J. Price, and M.P. Paidoussis, 1999, "Fluid Behaviour of Side-by-side Circular Cylinders in Steady Cross-flow". Journal of Fluids and Structures, 13(3), pp. 309-338
[28] R. Parker, and S.A.T. Stoneman, 1989, "The Excitation and Consequences of Acoustic Resonances in Enclosed Fluid Flow around Solid Bodies". Proceedings of the Institution of Mechanical Engineers, Part C: Journal of Mechanical and Engineering Science, 203(1), pp. 9-19
[29] R. Hanson, A. Mohany, and S. Ziada, 2009, "Flow-excited Acoustic Resonance of Two Side-by-side Cylinders in Cross-flow". Journal of Fluids and Structures, 25(1), pp. 80-94.
[30] A. Mohany, M. Hassam, and S. Ziada, 2011, "Numerical Simulation of the Flow-sound Interaction Mechanisms of Two Side-by-side Cylinders in Cross-flow". ASME Pressure Vessels & Piping Conference (PVP 2011), July 17-21, Baltimore, Maryland, USA, PVP2011-57282

TECHNICAL NOTE

A NOVEL BORON-LOADED LIQUID SCINTILLATOR FOR NEUTRON DETECTION

G. Bentoumi*, X. Dai, E. Pruszkowski, L. Li, B. Sur

Atomic Energy of Canada Limited, Chalk River Laboratories, Chalk River, Ontario, Canada, K0J 1J0

Article Info
Keywords: scintillation, boron, linear alkylbenzene, neutron
Article history: Received 13 April 2012, Accepted 25 June 2012, Available online 30 June 2012.
*Corresponding Author: (613) 584-3311 ext. 46727, BentoumG@aecl.ca

Abbreviations

LS - Liquid scintillator; LAB - Linear alkylbenzene; PPO - 2,5-diphenyloxazole; bis-MSB - 1,4-bis[2-methylstyryl]benzene; NRU - National Research Universal reactor; PMT - Photomultiplier tube; UV - Ultraviolet; IR - Infrared

ABSTRACT

A boron-loaded liquid scintillator (LS) has been optimized for neutron detection application in a high gamma field environment. It is composed of the solvent linear alkylbenzene (LAB), a boron-containing material, o-carborane ($C_2B_{10}H_{12}$)*; a fluor, 2,5-diphenyloxazole (PPO); and a wavelength shifter, 1,4-bis[2-methylstyryl] benzene (bis-MSB). Preparation of the liquid scintillator and optimization of its chemical composition are described. The boron-loaded LS has been tested with a neutron beam at the National Research Universal (NRU) reactor. A peak at an equivalent energy of 60 keV is observed in the energy spectrum and is attributed to neutrons. The results confirm the possibility of using B-10 loaded scintillator as a sensitive medium for neutron detection in a relatively large background of gamma rays.*

1. Introduction

Helium-3 filled ionization chamber tubes have been extensively used in neutron detection because of their good neutron-to-gamma discrimination capability. However, there is currently a global shortage of ^{3}He. As a result, it is necessary to design new neutron detectors relying on other mechanisms that are as effective as the ^{3}He detectors. Thermal neutron capture by boron-10 (^{10}B) has a cross section of 3838 barns, which leads to an average deposit of 2.34 MeV in the surrounding medium [1]. In a scintillator, part of this energy transforms to optical photons that can be detected easily using a photomultiplier tube (PMT) [1, 2]. Neutron detectors using solid, liquid or gas scintillators have been studied for replacing ^{3}He detectors.
Several ^{10}B-loaded liquid scintillator compositions are commercially available. However, they have several drawbacks. For instance, they typically contain a high content of Trimethyl Borate, which is unstable and decomposes in contact with moisture. These liquid scintillators are also flammable and yield lower light output. Therefore, new and improved liquid scintillators are needed for effective detection of neutrons.

2. Method

A general-purpose liquid scintillator based on the solvent linear alkyl benzene (LAB) is proposed herein. It has the general formula $C_6H_5C_nH_{2n+1}$, where n is an integer between 10 and 16. LAB is produced easily and has a high flash point (130 °C) [3]. Consequently a low-cost, high efficient and safe neutron detector can be prepared. In general, scintillator light output is enhanced by adding fluor PPO and wavelength-shifter bis-MSB.

Due to the nature of charge transfer between the solvent (LAB) and solutes (PPO and bis-MSB) and the light scintillation process, the optimization of the solutes' concentrations is of great importance. For this, we initially varied the PPO concentration from 0 to 30 g/l. When optimal concentration of PPO was established, the concentration of bis-MSB was varied from 0 to 1g/l. Solutions were produced by combining in different proportion pure LAB and highly concentrated LAB solution with 30 g/L PPO and 0.2 g/L bis-MSB. For light yield quantification, the samples were transferred to a 10 mm cylindrical quartz cell and a UV light source was used for excitation. Emitted blue light, primarily around 425 nm, was collected by an optical fibre for analysis with an Ocean Optics HR4000 UV-NIR spectrometer. Figure 1 shows an example of the emission spectrum for the scintillator LAB with the solutes PPO and bisMSB. A suitable integration time was chosen to allow accurate readouts. The area underneath the emission peak was determined. Firstly, each sample's yield curve was divided by its respective integration time to normalize

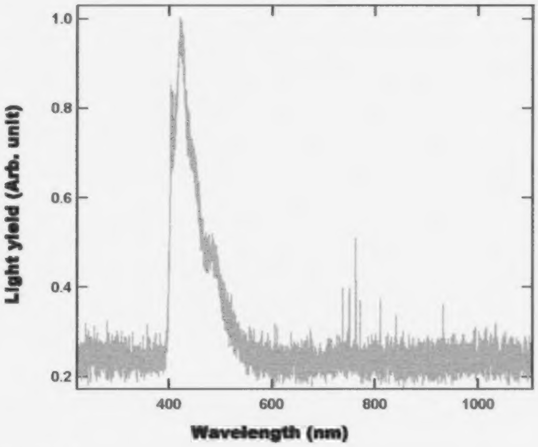

FIGURE 1
Emission spectra of scintillator including solvent LAB and solutes PPO and bisMSB.

the results. Then, the background light corresponding to range 600 - 650 nm was subtracted from the curve. Lastly, the area under each peak was determined using a Riemann sum.

3. Results and Conclusion

The results, as shown on Figures 2 and 3, show that scintillator light yield depends strongly on the concentrations of the fluors. For low PPO concentration (< 5g/l), light yield increases rapidly before saturation. For PPO concentration more than 5g/l, light yield is constant. The situation is somewhat similar by increasing the bis-MSB concentration. Thus, the optimal concentration for maximum light yield is 5 g/L of PPO and nearly 500 mg/L of bis-MSB.

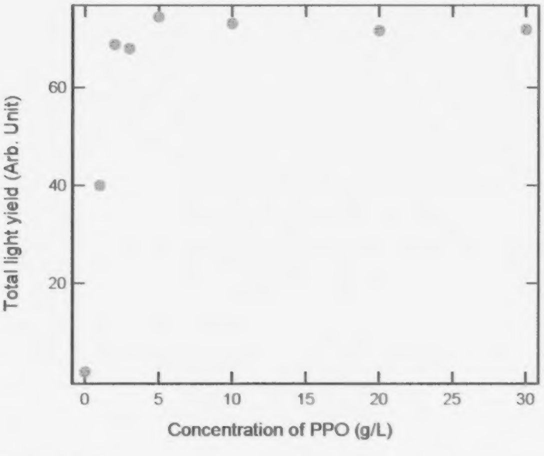

FIGURE 2
Light yield variation versus 2,5-diphenyloxazole (PPO) concentration in LAB.

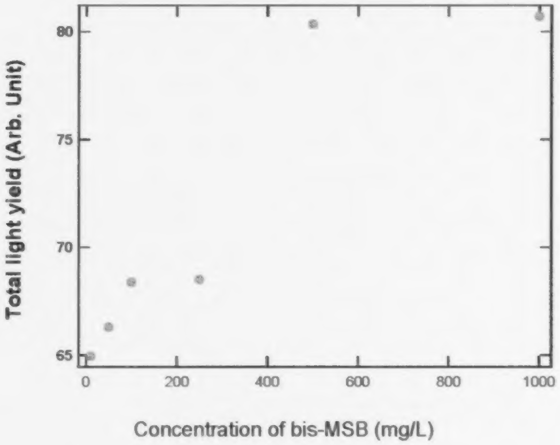

FIGURE 3
Light yield variation versus 1,4-bis[2-methylstyryl]benzene (bis-MSB) concentration in LAB.

In order to test performance of this optimized liquid scintillator, 5% of O-carborane ($C_2H_{12}B_{10}$) containing natural boron was loaded in the LS. As stated in the equation:

$$ {}^{1}_{0}n + {}^{10}_{5}B \rightarrow \begin{cases} {}^{7}_{3}Li(1.015\ MeV) + {}^{4}_{2}He(1.777\ MeV) & 6\% \\ {}^{7}_{3}Li\ (0.840\ MeV) + {}^{4}_{2}He(1.47MeV) + \gamma(0.478\ MeV) & 94\% \end{cases} $$

^{10}B neutron capture leads to creation of an alpha particle with an average energy of 1.48 MeV. It was demonstrated early [4,5] that in liquid scintillator, the quenching factor for 1 to 2 MeV alpha particles is in the range 20-25. Hence ^{10}B neutron capture is expected to generate a peak in the range 60-75 keV.

As shown on Figure 4, tests with a neutron beam were done at the National Research Universal (NRU) reactor. Due to the presence of gamma radiation and in order to extract the neutron contribution in the detected signal, four types of measurements were performed using combinations of cadmium sheet (to block neutron beam) and lead bricks (to stop gamma rays). The energy spectrum was acquired in four different conditions and calibrated using a Cobalt-60 source. Figure 5 shows the four energy spectra recorded for about 5 minutes. The presence of a peak around 60 keV is directly correlated to neutrons. Based on that correlation and the excepted equivalent energy for such capture interaction [2, 4, 5], the peak was definitely attributed to neutron capture by ^{10}B. To our knowledge, this is the first time such a measurement has been made with a LAB-based scintillator.

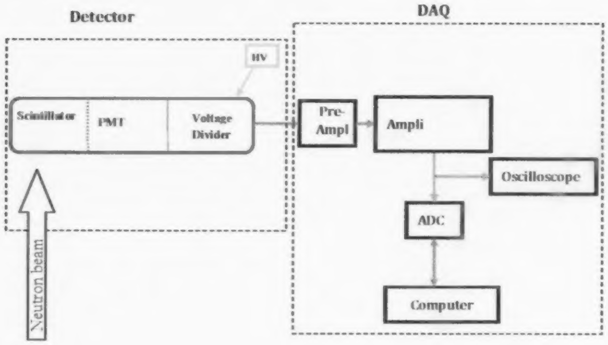

FIGURE 4
Experimental setup for scintillator characterization.

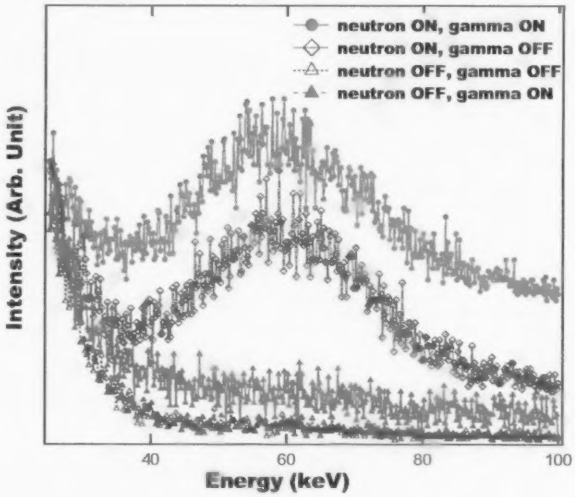

FIGURE 5
Energy spectra recorded in four conditions by the boron loaded LAB based scintillator. (△) Neutron OFF, gamma OFF, (•) Neutron ON, Gamma ON, (▲) Neutron OFF, Gamma ON, (◊) Neutron ON, Gamma OFF.

These measurements were possible despite the presence of gamma rays and are very encouraging for the use of boron-loaded LAB based scintillator in neutrons detection.

In conclusion, a boron-loaded liquid scintillator based on LAB solvent was prepared and its chemical composition has been optimized for high light output. Neutron beam measurements have shown a new peak around 60 keV. With a systematic study, this peak is confirmed to be due to neutron capture by boron-10. This confirmed the feasibility of using boron-loaded LAB as a safe, effective liquid scintillator for neutron detection.

REFERENCES

[1] Glenn F. Knoll, 2010, "Radiation Detection and Measurement", 4th ed. USA: John Wiley &Son Ltd.
[2] M. Yeh, A. Garnov, and R.L. Hahn, 2007, "Gadolinium-loaded Liquid Scintillator for High-precision Measurements of Antineutrino Oscillations and the Mixing Angle, 013". Nuclear instruments and Methods in physics Research A, 578(1), pp. 329-339
[3] T. Marrodán Undagoitia, F. von Feilitzsch, L. Oberauer, W. Potzel, and A. Ulrich, J. Winter, and M. Wurm, 2009, "Fluorescence Decay-time Constants in Organic Liquid Scintillators". Review of Scientific Instruments, 80(4), paper 043301 (2009)
[4] Wuon-Shik Kim, Hyeon-Soo Kim, Ki-Hwan Kim, Yong-Uhn Kim, and Ki-Hyon Kim, 1997, "Gamma-ray Pulse Height Spectrum of ^{241}Am-Be Source by ^{6}Li-BC501 (n-γ) Spectrometer System". Journal of Radioanalytical and Nuclear Chemistry, 215(2), pp. 257-261
[5] H. M. O'Keeffe, E. O'Sullivan, M. C. Chen, 2011, "Scintillation Decay Time and Pulse Shape Discrimination in Oxygenated and Deoxygenated Solutions of Linear Alkylbenzene for the SNO+ Experiment". Nuclear Instruments and Methods in Physics Research A, 640(1), pp. 119-122

TECHNICAL NOTE

INVERSE COLLIMATOR-BASED RADIATION IMAGING DETECTOR SYSTEM

A. Das*, B. Sur, S. Yue, G. Jonkmans

Atomic Energy of Canada Limited, Chalk River Laboratories, Chalk River, Ontario, Canada, K0J 1J0

Article Info
Article history: Received 29 May 2012, Accepted 20 June 2012, Available online 30 June 2012.
*Corresponding Author: (613) 584-3311 ext.43468, DasA@aecl.ca

ABSTRACT

A radiation imaging system has been developed using the concept of inverse collimation, where a narrow shielding pencil is used instead of a classical collimator. This imaging detector is smaller, lighter and less expensive than a traditionally collimated detector, and can produce a spherical raster image of radiation sources in its surroundings. A prototype was developed at Atomic Energy of Canada Limited – Chalk River Laboratories, and the concept has been successfully proven in experiments using a point source as well as real sources in a high ambient field area. Such a radiation imaging system is effective in locating radiation sources in areas where accessibility is low and risk of radiological contamination is high, with applications in decontamination and decommissioning activities, nuclear material processing labs, etc.

1. Introduction

Imaging and visual representation of radiation sources and radiological contamination have applications in several fields: radiation protection, decommissioning and cleanup, waste management, to name a few. Improvements in techniques for imaging high radiation fields are making such imaging systems smaller, faster and more cost effective.

Development of a radiation source imaging system at Chalk River Laboratories (CRL) was motivated in part by a need to image the sources of radiation inside a radioactive isotope processing hot-cell. Manual access inside the hot-cell is restricted for radiological safety reasons and equipment entering the cell has size and weight restrictions. In imaging of radiation sources using non-directional sensors, directionality is achieved through use of heavy shielding collimators. The use of collimators, including variations such as pinhole and parallel hole collimators, is a common technique in many prior applications [1, 2, 3, 4] for imaging radiation sources. However, the bulk and weight of this general collimator design often requires a robust assembly and relatively powerful actuators to manoeuvre the collimated detector, which is expensive in terms of the material and actuators. There exists a need in many applications for an inexpensive light-weight radiation imaging system. This paper describes a novel approach to the collimator design for a lighter and economical radiation detector system, developed at CRL.

2. Materials and Methods

The sensor of choice for this application is a silicon PIN photodiode. Si diodes are simple, robust, low-cost, and have been widely used for measuring gamma dose rates. The total charge generated in a Si diode is well known to be proportional to the ionization energy deposited in the diode depletion region, and thus the radiation dose [5]. Consequently, the current in an unbiased Si diode is a measure of the radiation field or dose rate. In current generation mode, p-n junction diodes as well as PIN photodiodes have been successfully used as high radiation field detectors in many facilities at CRL [6, 7, 8]. The photodiode sensor used in this application is sensitive to gamma dose rates in the range of 10^{-3} Gy.h^{-1} to 10^{3} Gy.h^{-1}.

A collimator enables a non-directional sensor to be used in a directional detector system, usually by surrounding the sensor with dense shielding material with a small aperture, such that radiation from all directions except the aperture is blocked. In a typical collimator, the detector response is high when the aperture faces the direction of a source and low elsewhere. An inverse collimator instead comprises a shielding 'pencil' – a thin rod or cone, of dense material that blocks radiation from a narrow solid angle. The detector response is relatively low when the shielding pencil is pointed towards a strong radiation source, and high otherwise. This concept is illustrated in Figure 1 for the case of a single point source. The concept of inverse collimation exists in literature [9], albeit purely for planar imaging of relatively low radiation sources as applicable to nuclear medicine imaging.

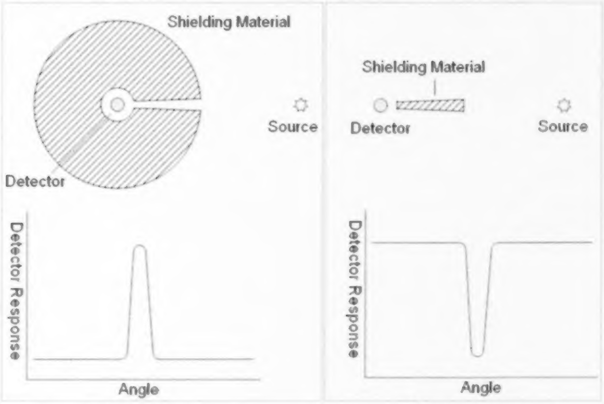

(a) Collimator (b) Inverse collimator

FIGURE 1
Collimator vs. inverse collimator, and their ideal response functions

To realize the inverse collimator concept in an imaging system, a thin rod of gamma blocking material needs to be assembled with the sensor and integrated with a mechanism that allows the detector and inverse collimator assembly to be pointed in all directions. A suitable pan-tilt solution was not found commercially; therefore, an inexpensive module to pan and tilt the detector and inverse collimator assembly was designed and built at CRL.

The pan-tilt module employs two stepper motors; one at the base for rotation in the horizontal plane (pan functionality) and one higher up on the body for rotation in the vertical plane (tilt function). A thin lead (Pb) pencil serves as the inverse collimator material in this design; see Figure 2. The sensor and the inverse collimator pencil are mounted in a diametric spoke of the vertical gear wheel (175 mm in diameter), which is driven by the tilt motor through a driver gear. The gear wheel, driver gear and tilt motor are mounted on a wheel base, which is rotated on the horizontal plane by the pan motor [10]. A low-noise signal cable attaches to the sensor at its mounting location, with sufficient slack-length to prevent cable wind-up; a separate power connection is not required.

The entire body of the pan-tilt device is constructed out of high-performance composite material using a 3D printer. This provided an inexpensive and radiologically unobtrusive body, especially for the tilt mechanism that houses the sensor. This complete imaging system has been patented by AECL.

3. Results and Discussion

The imaging detector system was tested using a 37 GBq (10 Ci) ^{60}Co providing a conical gamma beam. The source was placed roughly 380 mm from the center of the imaging system. This test served as a proof-of-concept, and allowed measurement of the detector's response to a simple source configuration to analyse the accuracy and limitations of the system. The image generated from this test is presented in Figure 3, as a plot of the gamma field intensities versus directions, represented on a unit sphere. Note that the numbers on the scale bar are only to be used as a relative measure. The utility of such an image is to visually present the directions of all sources that contribute to the radiation field at the detector location, and to identify the source with the highest contribution. It must be noted that the raw data collected by the system represents the inverse (or photo-negative) of the desired image; thus a photo-negation algorithm is applied to obtain the image [10].

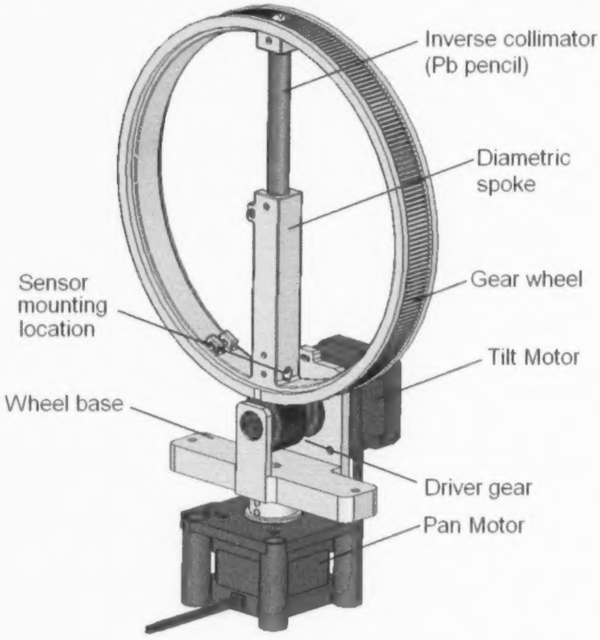

FIGURE 2
Light yield variation versus 2,5-diphenyloxazole (PPO) concentration in LAB.

Figure 3 (a) shows the location of the source as represented on the sphere. The high signal area on the side away from the source [Figure 3 (b)], is a result of the sensor's directionality. The photodiode sensor is rectangular prism shaped; its sensitivity to gamma rays incident on the tips is roughly 60% that of the sensitivity along the sides of the sensor. The detector system is configured such that the sensor is longitudinally in line with the inverse collimator, with the tips facing towards and directly away from the inverse collimator. As a result, a false low measurement occurs when the

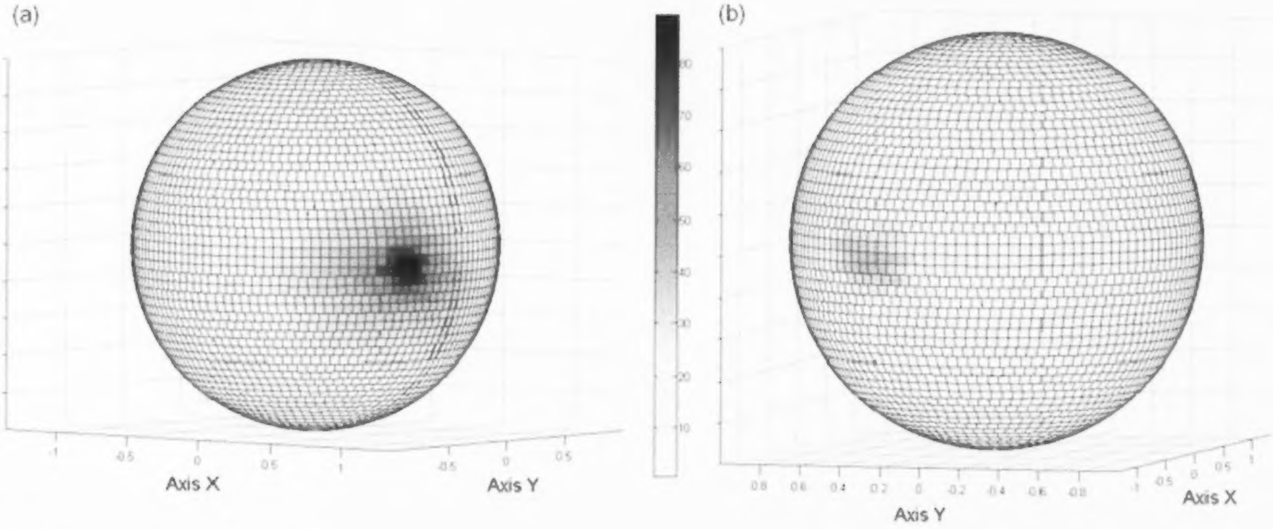

FIGURE 3
Gamma radiation source distribution image of a point source (a) side facing source (b) side away from source.

tip of the sensor is facing the source, which translates to a peak upon image inversion. Thus, for each strong source, there will be a secondary area of high signal directly opposite to the direction of the source. This effect proves to be useful in distinguishing erroneous signals and verifying true source locations.

A practical and more realistic test was performed in order to test the ability of the system to image two highly radioactive items in the presence of a high background field. A section of pressure tube removed from a CANDU® reactor, and an irradiated CANDU® fuel pin were placed in a radioactive materials handling hot-cell, operated by the Materials and Mechanics branch at CRL. A Si diode gamma detector calibrated in a Co-60 gamma cell [7] was used to measure the near contact gamma radiation fields for these objects; they were found to be roughly 1.3 $Gy.h^{-1}$ for the pressure tube section and 33 $Gy.h^{-1}$ for the fuel pin.

The roughly 5 m wide by 3 m deep hot-cell also contained miscellaneous pieces of equipment and tools that contributed to the ambient gamma field. The detector system was placed to one side of the cell and the two items used for this study were placed around it, as depicted in Figure 4. The fuel pin was laid flat on the floor, roughly 0.3 m from the base of the detector, and the pressure tube section was placed vertically around 1 m from the detector.

The image obtained of this setup is shown in Figure 5, with the outlines of the sources projected onto the surface of the sphere. The high signal area observed in Figure 5 (a) is in the direction expected for the fuel pin. The secondary high signal area due to the fuel pin can be observed in Figure 5 (b), directly opposite to the fuel pin location. As expected, the radiation fields observed from the fuel pin were much higher than the fields from the piece of pressure tube. The radiation exposure at the detector due to the pressure tube piece was too small to be resolved in the presence of the much higher radiation field of the fuel pin.

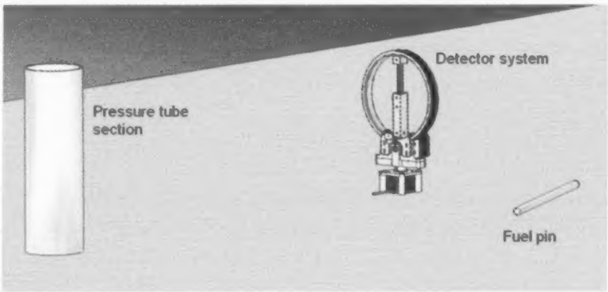

FIGURE 4
Multi-source image generation study setup inside hot-cell

4. Conclusion

Imaging of radiological environments can be performed using a directional sensor, where directionality is usually achieved through heavy collimation. The concept of using

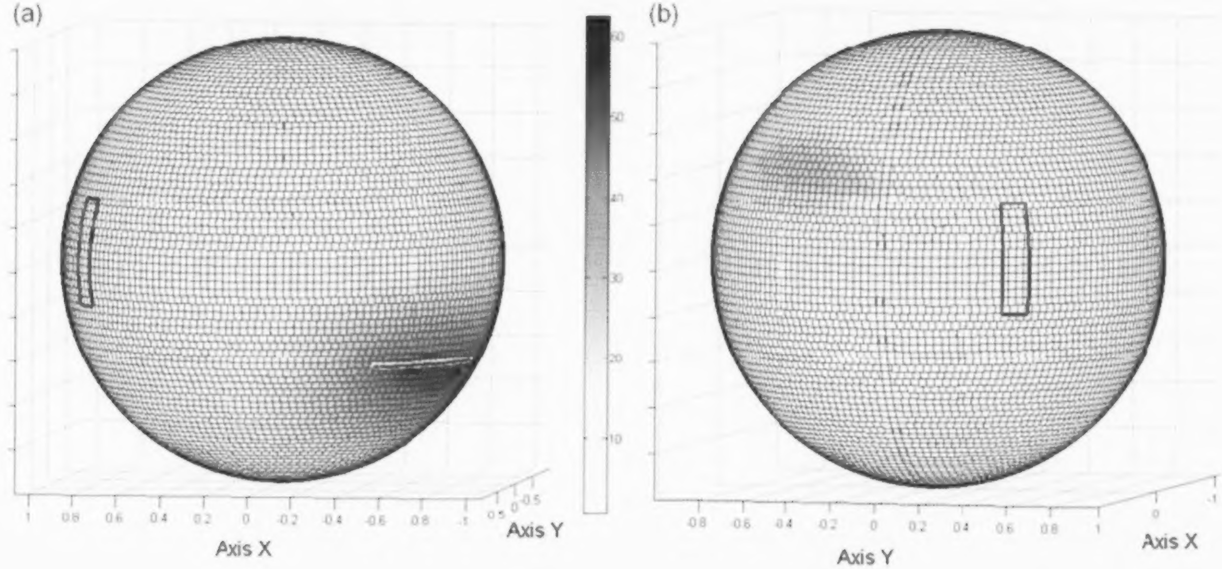

FIGURE 5
Radiation image generated in the hot-cell with the outline of the two sources overlaid as projections onto the sphere. (a) Bright spot corresponding to the fuel pin, along with superimposed outlines of pressure tube and fuel pin (b) Secondary bright spot associated with fuel pin, along with pressure tube outline

an inverse collimator, consisting of shielding material in a narrow solid angle where a typical collimator would have an aperture, has been proven at CRL. An inverse collimator is lighter and less expensive, both in terms of material cost and cost of actuators.

A radiation imaging detector system was designed and built in-house at CRL, using a silicon photodiode as the gamma sensor and a lead (Pb) pencil as the shielding material, assembled in a 3D printed composite body. The image is generated by rotating the sensor assembly, performing exposure rate measurements across the 4π solid angle around the sensor, and assembling the data as a spherical raster image. The raw image is then inverted to correct the photonegative effect due to the inverse collimator. This system was demonstrated successfully in a controlled environment using a ^{60}Co point source.

A test was conducted to determine the ability of the detector system to image two highly radioactive materials in the presence of high radiation background. The near contact gamma fields for the two items differed by a factor of 25, and the less radioactive item was placed farther from the detector. The system was able to detect and image the more radioactive item, but not the less radioactive item. It is concluded that changes in radiation exposure at the detector as the inverse collimator was swept through the direction of the weaker source were too small to be resolved in the presence of the much higher radiation field due to the stronger source. The test showed a limitation of inverse collimator systems in detecting radiation sources in the presence of much stronger sources. Further work is required to better define and improve the detection thresholds of the system so that weaker sources may be successfully imaged.

5. Acknowledgements

The authors wish to thank Elzbieta Rochon, Heather Chaput, Joseph Bida and Kevin McCarthy from AECL CRL, for providing use of their facilities and their assistance in sensor study and testing of the imaging system. The authors would also like to acknowledge the contributions of Alexandar Mechev and Hinkel Yeung, undergraduate students from the University of Waterloo, in post-processing for image reconstruction and mechanical design of the hardware, respectively.

REFERENCES

[1] R. Redus, et. al., October 1995 "An Imaging Nuclear Survey System," Nuclear Science Symposium and Medical Imaging Conference Record, IEEE, 1, pp. 649-652

[2] W. Lee, G. Cho, 2002, "Pinhole Collimator Design for Nuclear Survey System." Annals of Nuclear Energy, 29(17), pp. 2029-2040

[3] A.N. Sudarkin, O.P. Ivanov, V.E. Stepanov, A.G. Volkovich, A.S. Turin, A.S. Danilovich, D.D. Rybakov, L.I.N. Urutskoev, 1996, "High-energy Radiation Visualizer (HERV): a New System for Imaging in X-ray and Ramma-ray Emission Regions." Recom Ltd., Kurchatov (I.V.) Inst. of Atomic Energy, Moscow, IEEE Transactions on Nuclear Science, 43(4), part 2, pp. 2427-2433

[4] M. Woodring, D. Souza, S. Tipnis, P. Waer, M. Squillante, G. Entine, K.P. Ziock, 1999, "Advanced Radiation Imaging of Low-intensity Gamma-ray Sources." Nuclear Instruments and Methods in Physics Research, Section A: Accelerators, Spectrometers, Detectors and Associated Equipment, 422(1-3), pp. 709-712

[5] Knoll, G.F., 1989, "Radiation Detection and Measurement," 2nd Edition, John Wiley & Sons

[6] B. Sur, S. Yue, and A. Thekkevarriam, June 2007, "Radiation Exposure Rate and Liquid Level Measurement Inside a High Level Liquid Waste (HLLW) Storage Tank," Proceedings of the 28th Annual Conference of the Canadian Nuclear Society, Saint John, New Brunswick, Canada

[7] B. Sur, S. Yue, G. Jonkmans, "A Detector System for Measuring High Radiation Fields," April 2009, 6th American Nuclear Society International Topical Meeting On Nuclear Plant Instrumentation, Control, And Human-Machine Interface Technologies (NPIC & HMIT), Knoxville, Tennessee, USA

[8] A. Das, S. Yue, B. Sur, et al., May 2010 "Gamma Radiation Scanning of Nuclear Waste Storage Tile Holes," Proceedings of the 31st Annual Conference of the Canadian Nuclear Society, Montréal, Québec, Canada.

[9] D. J. Wagenaar et. al., July 2007 "Inverse Collimation for Nuclear Medicine Imaging," US Patent 7242003

[10] A. Das, B. Sur, S. Yue, G. Jonkmans, "Detector System for Radiation Imaging Using Inverse Collimation," June 2011, Proceedings of the 32nd Annual Conference of the Canadian Nuclear Society, Niagara Falls, Ontario, Canada

TECHNICAL NOTE

ANTHROPOGENIC RADIONUCLIDES IN OTTAWA RIVER SEDIMENT NEAR CHALK RIVER LABORATORIES

D.J. Rowan*

Atomic Energy of Canada Limited, Chalk River Laboratories, Chalk River, Ontario, Canada, K0J 1J0

Article Info
Article history: Received 19 May 2012, Accepted 26 June 2012, Available online 30 June 2012.

*Corresponding Author: (613) 584-3311 ext. 44732, RowanD@aecl.ca

ABSTRACT

The Ottawa River has received nuclear reactor effluent from Chalk River Laboratories (CRL) for more than 60 years, including releases from a NRX accident in 1952. Recent interest in the potential impact of these historical releases and the possible need for remediation of a small region immediately downstream from the release point has led to comprehensive studies to assess risk to people and wildlife. In this paper, the results of an extensive survey of gamma-emitting anthropogenic radionuclides in Ottawa River sediment in the vicinity of CRL are presented. Anthropogenic radionuclides detected in Ottawa River sediment include ^{60}Co, ^{94}Nb, ^{137}Cs, ^{152}Eu, ^{154}Eu, ^{155}Eu *and* ^{241}Am. *Concentrations of all anthropogenic radionuclides decline rapidly with distance downstream of the process outfall, reaching stable concentrations about 2 km downstream. All of these radionuclides are found at some sites within 2 km upstream of the process outfall suggesting limited upstream transport and sedimentation. Comparison of anthropogenic radionuclides with several representative primordial radionuclides shows that with the exception of sites at the process outfall and within 2 km downstream of the process outfall, primordial radionuclide concentrations greatly exceed CRL derived anthropogenic radionuclide concentrations. Thus, over 60 years of radionuclide releases from operations at CRL have had little impact on radionuclide concentrations in Ottawa River sediment, except at a few sites immediately adjacent to the process outfall.*

1. Introduction

The Ottawa River has received nuclear reactor effluent from Chalk River Laboratories (CRL) for more than 60 years, including releases from a NRX accident in 1952. The process outfall releases liquid effluent through a vertical diffuser located at a depth of approximately 22 m. In 1992, a "once through" research reactor was permanently shut down, significantly reducing the quantity of fission and activation products released to the river. Continuing releases are extremely low, approaching or exceeding analytical capabilities. Recent interest in the potential impact of these historical releases and the possible need for remediation of a small region immediately downstream from the release point has led to comprehensive studies to assess risk to people and wildlife. The river at the outfall is public and boaters, fishermen and campers regularly use this reach of the river.

The aquatic ecosystem at the site has been studied previously, including ^{137}Cs bioaccumulation and biokinetics of invertebrates and fish [1-4] and bioavailability of radionuclides to aquatic macrophytes and associated epiphytes [5]. However, there has not been a comprehensive study of the benthic community and sediment since the early 1950's [6].

In this study, I compare concentrations of anthropogenic radionuclides upstream of the process outfall are compared, on a transect containing the process outfall, sites within 2 km downstream of the process outfall referred to as the footprint, and sites further downstream. Anthropogenic radionuclide concentrations with those of several primordial radionuclides are also compared.

2. Methods

Ottawa River sediment was sampled on transects spaced at 1 km intervals, for distances of about 8 km upstream and downstream of the Chalk River Laboratories process outfall. Sample sites were chosen at depth internals of 0-5, 5-10, 10-15, 15-20, 25-30 and 30-50 m from both shorelines. A total of 214 sites were sampled using a 9" x 9" Ekman dredge. A core sample of the upper 5 cm of sediment was taken from each Ekman dredge and retained and dried at 0°C. The sediment was ground and packed in 50 ml vials for radionuclide determination by gamma spectroscopy using a low-background high purity germanium gamma spectrometer.

3. Results

3.1 Anthropogenic Radionuclides

^{137}Cs was detected in all sediment samples (see Table 1). ^{137}Cs in sediments upstream of CRL is due to atmospheric nuclear weapon tests during the early 1960's, although the higher concentrations within 2 km upstream of CRL suggests some upstream transport of reactor derived ^{137}Cs (see Figure 1). Concentrations are greatest at the process outfall, rapidly dropping off within 2 km downstream, to rather stable concentrations from 2-9 km downstream (see Figure 1). Downstream concentrations are about two-fold greater than upstream concentrations (see Table 1), suggesting that CRL releases have been equivalent to weapon test fallout.

TABLE 1
Concentrations of anthropogenic radionuclides in sediment up to 8 km upstream from the process outfall, at the process outfall, up to 2 km downstream of the process outfall, in the footprint and 2 to 8 km downstream of the process outfall.

Radionuclide	Upstream (n=83)	Process Outfall (n=5)	Footprint (n=35)	Downstream (n=91)
^{60}Co (Bq kg^{-1})	5.3±1.0	2944±2364	296±216	19±1.6
n	21	5	35	91
^{94}Nb (Bq kg^{-1})	6.5±4.9	18±9.0	12±7.0	1.6±0.5
n	2	5	26	38
^{137}Cs (Bq kg^{-1})	85±5.3	3411±1750	585±145	198±12
n	83	5	35	91
^{152}Eu (Bq kg^{-1})	1.1±0.1	240±171	46±22	3.0±0.2
n	2	5	22	59
^{154}Eu (Bq kg^{-1})	nd	179±134	24±13	1.2±0.1
n		5	18	9
^{155}Eu (Bq kg^{-1})	nd	40±24	46	nd
n		3	1	
^{241}Am (Bq kg^{-1})	2.4±0.3	84±57	16±4.4	3.2±0.3
n	27	5	24	56

Am-241 is another anthropogenic radionuclide that was globally distributed by atmospheric testing and was detected at most of the deeper sites. Upstream concentrations are not significantly different than downstream concentrations (see Table 1), with highest concentrations at the process outfall, and rapidly decreasing in the footprint (see Figure 2). Concentrations of ^{241}Am are about 40-fold lower than those of ^{137}Cs (see Table 1).

Co-60 is an activation product and present in Ottawa River sediments due to operations at CRL. ^{60}Co is only found at upstream sites within 2 km of the process outfall, again suggesting limited upstream transport of CRL radionuclides (see Table 1 and Figure 3). At the process outfall, concentrations of ^{60}Co are similar to those of ^{137}Cs, but ^{60}Co concentrations decline much more rapidly through the footprint (see Figure 3). Downstream concentrations of ^{60}Co are about 10-fold lower than ^{137}Cs (see Table 1).

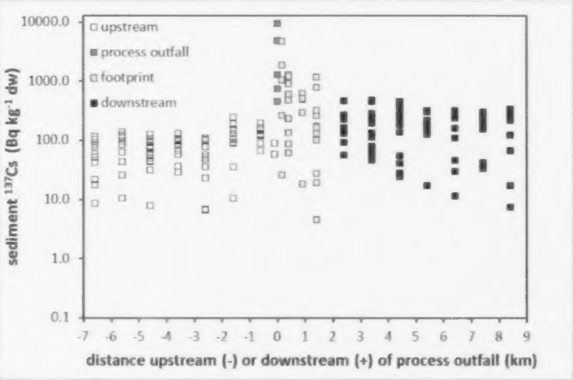

FIGURE 1
^{137}Cs in Ottawa River sediment.

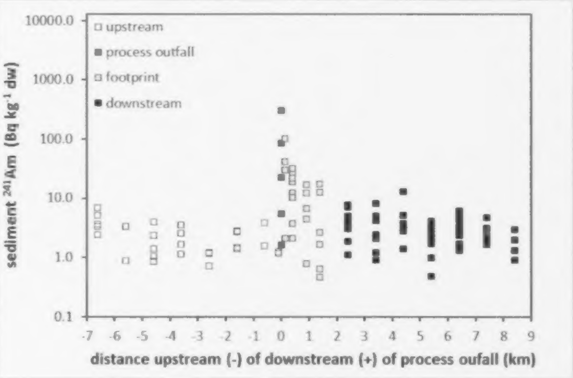

FIGURE 2
^{241}Am in Ottawa River sediment.

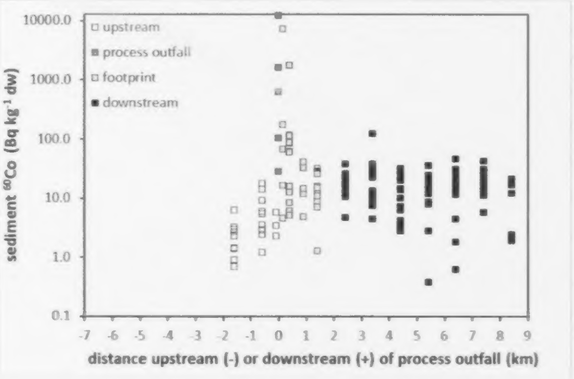

FIGURE 3
^{60}Co in Ottawa River sediment.

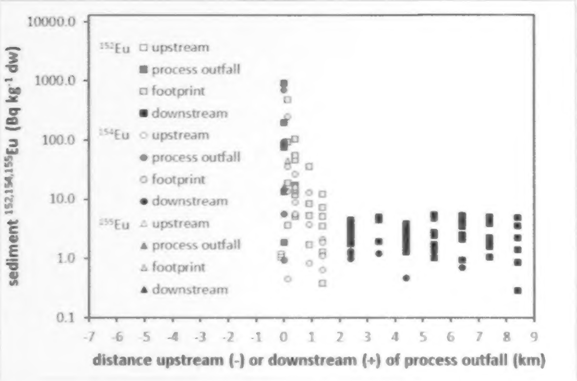

FIGURE 4
^{152,154,155}Eu in Ottawa River sediment.

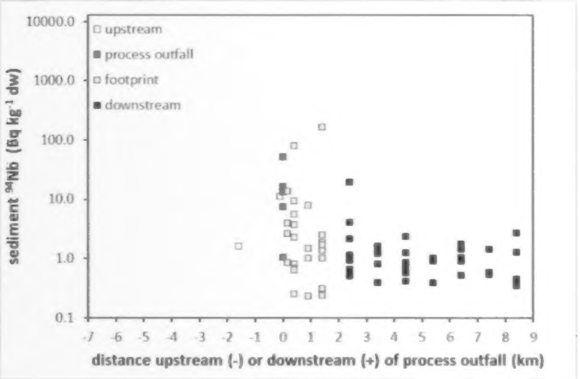

FIGURE 5
^{94}Nb in Ottawa River sediment.

^{152}Eu, ^{154}Eu and ^{155}Eu were detected at some sites near the process outfall, within the footprint and downstream. ^{152}Eu was the most widely detected of the three Eu radioisotopes, with much fewer detections for ^{154}Eu and ^{155}Eu, which was detected only in the immediate vicinity of the process outfall (see Table 1). Concentrations of Eu radioisotopes drop off very rapidly from the process outfall through the footprint, and are present at very low concentrations at downstream sites (see Figure 4).

^{94}Nb was detected at low concentrations in the vicinity of the process outfall, dropping off to very low downstream concentrations of a few Bq kg^{-1} (see Table 1 and Figure 5). As with other CRL derived radionuclides, there is evidence of limited upstream transport (see Figure 5). The distribution of ^{94}Nb is similar to ^{241}Am and ^{152}Eu, and ^{94}Nb was detected primarily in depositional sediments at deeper sites.

3.2 Primordial Radionuclides

A number of primordial radionuclides were detected in Ottawa River sediment, including K-40 and radionuclides from the ^{238}U and Th decay series. K-40 is the most abundant of the primordial radionuclides, averaging 537±5 Bq kg^{-1}. K-40 concentrations in Ottawa River sediment are not affected by CRL effluent, with very similar concentrations at all sites (see Figure 6). K-40 concentrations exceed those of all anthropogenic radionuclides except at some process outfall and footprint sites.

Bi-214 (^{238}U decay series) and ^{228}Ac (^{232}Th decay series) also show no impact of CRL operations, with uniform concentrations at all sites (see Figure 7). These radionuclides occur at much lower concentrations in Ottawa River sediment than ^{40}K, with ^{214}Bi averaging 16.1±0.3 Bq kg^{-1} and ^{228}Ac averaging 33.3±0.9 Bq kg^{-1}. These primordial radionuclides

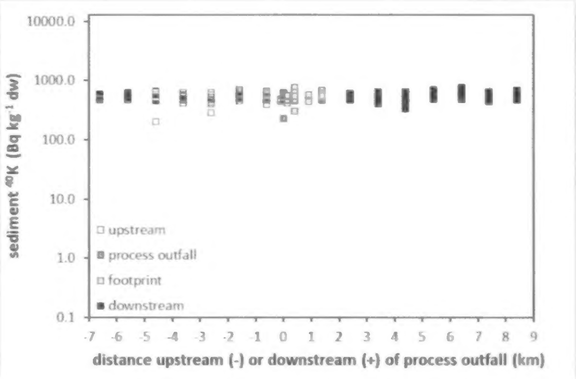

FIGURE 6
^{40}K in Ottawa River sediment.

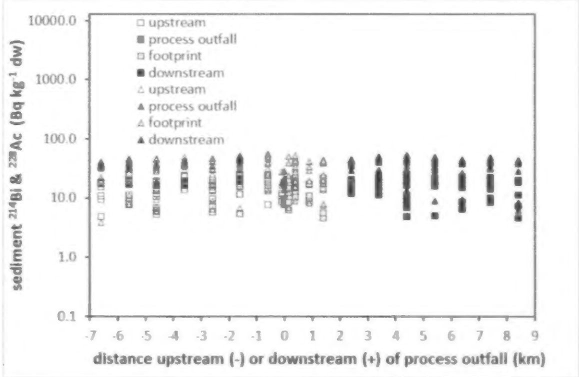

FIGURE 7
^{214}Bi and ^{228}Ac in Ottawa River sediment.

are present in concentrations similar to ^{60}Co at downstream sites and are about 10-fold higher than the other anthropogenic radionuclides at downstream sites.

Conclusions

Cs-137 and ^{241}Am in Ottawa River sediment are due to weapon-test fallout and CRL releases. CRL operations have about doubled weapon test fallout ^{137}Cs at downstream sites. Am-241 occurs at much lower concentrations and appears to be retained near the process outfall, with no significant difference between upstream and downstream (>2 km from the process outfall) sites. Other anthropogenic radionuclides detected in Ottawa River sediment include ^{60}Co, ^{94}Nb, ^{152}Eu, ^{154}Eu and ^{155}Eu. These radionuclides are also found at some sites within 2 km upstream of the process outfall, suggesting upstream transport of small amounts of CRL releases. Upstream movement of surface water during periods of strong upstream wind has been previously observed [7]. These radionuclides decline rapidly with distance from the process outfall, and as with ^{137}Cs and ^{241}Am, reach stable levels after about 2 km downstream of the process outfall. ^{137}Cs and ^{94}Nb decline to a lesser degree from process outfall to downstream sites, suggesting that these radionuclides are more mobile that the other anthropogenic radionuclides.

Comparison of anthropogenic radionuclides with several representative primordial radionuclides shows that with the exception of sites at the process outfall and within 2 km downstream of the process outfall, primordial radionuclide concentrations greatly exceed CRL derived anthropogenic radionuclide concentrations. In fact, CRL derived ^{137}Cs in sediment at downstream sites is only about 20% of naturally occurring ^{40}K. Co-60 concentrations in sediment at downstream sites are only about 3.5% of ^{40}K and are similar to representative ^{238}U and ^{232}Th decay series radionuclides. Other anthropogenic radionuclides occur in much lower concentrations (<1% of ^{40}K) and are about an order of magnitude lower than representative ^{238}U and ^{232}Th decay series radionuclides. Thus, over 60 years of radionuclide releases from operations at CRL have had little impact on radionuclide concentrations in Ottawa River sediment, except at a few sites immediately adjacent to the process outfall.

REFERENCES

[1] D.J. Rowan and J.B. Rasmussen, 1994, "Bioaccumulation of Radiocesium by Fish: The Influence of Physicochemical Factors and Trophic Structure". Canadian Journal of Fisheries and Aquatic Sciences, 51(11), pp. 2388-2410

[2] D.J. Rowan and J.B. Rasmussen, 1996, "Measuring the Bioenergetic Cost of Fish Activity in Situ Using a Globally Dispersed Radiotracer (137Cs)". Canadian Journal of Fisheries and Aquatic Sciences, 53(4), pp. 734-745

[3] D.J. Rowan, 2012 In press. "Bioaccumulation Factors and the Steady State Assumption for Cesium Isotopes in Aquatic Foodwebs Near Nuclear Facilities". Journal of Environmental Radioactivity.

[4] F.W. Whicker, C.T.Garten Jr., D.M. Hamby, K.A. Higley, T.G. Hinton, D.I. Kaplan, D.J. Rowan and R.G. Schreckhise, 2007, "Cesium-137 in the Environment: Radioecology and Approaches to Assessment and Management". National Council on Radiation Protection and Measurements, Bethesda, NCRP Report No. 154

[5] L.J. Jackson, D.J. Rowan, R.J. Cornett and J. Kalff, 1994, "Myriophyllum Spicatum Pumps Essential and Nonessential Trace Elements from Sediments to Epiphytes". Canadian Journal of Fisheries and Aquatic Sciences, 51(8), pp. 1769-1773

[6] F.H. Rigler, 1952. "Study of Radioactivity in Ottawa River Organisms and Bottom Deposits". M.A. Thesis, University of Toronto

[7] W.F. Merritt, 1964, "Studies of Dilution in the Ottawa River Using Rhodamine B 2 - CRNL to Pembroke". Atomic Energy of Canada Ltd. Report, AECL 2030

AECL
EACL

AN OFFICIAL PUBLICATION OF
ATOMIC ENERGY OF CANADA LIMITED

WWW.AECL.CA